ABSTRACT

GRIMLEY, CAROLYN ANDREA. Decoupling Chemical, Thermal, and Electrical Effects in Flash Sintering. (Under the direction of Dr. Elizabeth C. Dickey).

Sintering is a fundamental technique in the production of most ceramic-containing products, yet the field has seen little innovation over hundreds of years. Flash sintering offers a sintering innovation that uses high electric fields to reduce densification times and furnace temperatures by orders of magnitude. The densification mechanisms of the technique remain a topic of debate though, as the scientific community has struggled to assign the characteristics of flash sintering, like limited grain growth and rapid densification, to the unusual thermal profile of flash or to athermal field effects. This work reports and discusses a set of studies that separately consider the effects of the thermal and athermal processes during flash sintering, using yttria-stabilized zirconia (YSZ) as a well-characterized baseline material.

Much fundamental work on flash sintering has been performed under DC fields, yet it is well-established that DC fields can produce stoichiometry changes in mixed conductors. This effect was considered in the context of the DC flash sintering of YSZ by varying electrode configurations, as well as current densities and hold times. Combined with a low background furnace temperature, these experiments elucidated the effects of the DC field in the early stages of microstructure development. Stoichiometric reduction resulted in densification gradients, with high density on the anode and low density on the cathode, and its severity depended heavily upon the experimental parameters above. This dependency was discussed, and the link between reduction and densification was proposed to be the transient thermal gradient which results from the relative differences in conductivity between stoichiometric and non-stoichiometric YSZ.

To mitigate the stoichiometry gradients produced by DC fields, the next studies were performed using AC electric fields. The implementation of this system included current ramp-

rate controlling software, and that parameter formed the basis for one set of experiments. The current ramp rate was varied such that the densification time ranged from ~30s – corresponding to the fastest rate that current would increase in the sample – to several hours, similar to conventional sintering. The current ramp rate corresponded directly to the heating rate, controlling the thermal profile. The density and microstructural trends across heating profiles were consistent with those found in traditional sintering: faster current ramp rates limited final density due to trapped pores. Samples subject to high temperatures beyond the time required for densification exhibited grain growth comparable to that of conventional sintering. The electrical conductivities of the densified, flash sintered samples were generally explicable by their thermal profiles, although the grain boundary conductivities exhibited an increase relative to conventionally sintered samples that was difficult to explain on a purely thermal basis.

Finally, a set of experiments was performed in which the frequency of the AC field was varied across five decades. It was hypothesized that a dependence on frequency might emerge around the characteristic loss frequencies of the sample. Preliminary characterization of the green bodies identified the frequency related to the sample/electrode interfacial impedance contribution, and samples were flash sintered above and below this value. When flash sintering above this frequency, the interfacial impedance of the green body was qualitatively preserved, indicating that an interfacial conduction mechanism or reaction was short-circuited during high frequency flash. When flash sintering below this frequency, the qualitative interfacial impedance changed dramatically. Based on this finding, an interfacial reaction was proposed in which the oxygen exchange reaction between YSZ and the atmosphere is short-circuited above the critical frequency value.

Decoupling Chemical, Thermal, and Electrical Effects in Flash Sintering

by
Carolyn Andrea Grimley

A dissertation submitted to the Graduate Faculty of
North Carolina State University
in partial fulfillment of the
requirements for the degree of
Doctor of Philosophy

Materials Science and Engineering

Raleigh, North Carolina
2020

APPROVED BY:

Dr. Elizabeth C. Dickey Committee Chair	Dr. Jacob L. Jones
Dr. Douglas Irving	Dr. Daryoosh Vashaee

DEDICATION

To God the Father be all glory and honor, forever, amen. Also to my amazing and supportive husband, Everett.

BIOGRAPHY

Carolyn Grimley attended the University of Virginia in Charlottesville, VA from 2010-2014, where she completed her B.S. in Chemical Engineering. During her time there, she worked as an undergraduate researcher in Dr. Giovanni Zangari's electrochemistry group studying the solution-mediated growth of aluminum oxide thin films. She moved to Raleigh, NC in 2014 to begin her doctoral studies in Materials Science and Engineering.

ACKNOWLEDGMENTS

Many thanks are owed to my advisor, Beth Dickey, for not being satisfied with easy answers and guiding me through finding the hard ones. Thanks to all my group members along the way; special thanks to Weston Straka and John McGarrahan for long hours spent as sounding boards and co-problem solvers and to Steve Funni for ANSYS and TEM help.

Thanks to Lucideon, for funding all of the work in this dissertation, and to their flash sintering team for their help with the on-site experiments which show up in Chapter 6. Thanks especially to Chris Green for many helpful and interesting conversations, for patience with frequent emails, and for always thinking problems through to completion.

Thanks as well to the Department of Defense (grant FA9550-17-2226), which supported the IR imaging equipment used in this dissertation, as well as the Analytical Instrumentation Facility (AIF) and North Carolina State University, which is supported by the State of North Carolina and the National Science Foundation (award number ECCs-1542015).

Thanks to my family, by blood and by marriage, for being patient with me every time I showed up at a family event stressed out and unsociable, and letting me know I always had support from you regardless. Thanks to Dad, for the pick-me-up emails and song recommendations, to Mom, for being interested even in un-interesting life details, and Rachel, for sharing your home and adorable children with me regularly. Special thanks to my in-laws, Donna and Will, and my siblings in-law, for adopting me so quickly, and letting me hog the cat over Christmas.

The most deserving of all the thanks is my husband, Everett Grimley, whose support has been unwavering and invaluable. Finding you was by far the best discovery of my graduate career.

TABLE OF CONTENTS

LIST OF TABLES

LIST OF FIGURES

CHAPTER 1

An Overview of Empirical Evidence Concerning the Mechanisms of Field-Assisted and Flash Sintering

1.1 Motivation

Sintering, or the consolidation of a porous, packed body, is integral to the production of most ceramic components, and finds application in industries ranging from energy production to national defense and in products spanning dielectric capacitors to tile ware. It is also an incredibly costly processing step in terms of production time, money, and energy, typically requiring the ceramic body to be subject to high temperatures for several hours. Therefore, there is great industrial interest, from both a monetary and energy efficiency perspective, in processes that may reduce this high cost. Electric-field based ceramic sintering techniques such as flash sintering have been shown on a small scale to produce dense bodies faster than traditional sintering, at lower furnace temperatures, and with properties that may be highly beneficial to structural applications (e.g. small grain sizes). However, the fundamental science of flash sintering is currently too poorly understood for large-scale adaptation.

As a test material, yttria-stabilized zirconia (YSZ) represents a well-studied and technologically relevant structural ceramic used in a variety of applications. At lower doping

levels (~3 mol% Y), the tetragonal phase of zirconia is stabilized, which gives rise to a stress-induced toughening effect based on a phase transformation which applies compressive stress to crack tips; this makes it a desirable material for aerospace applications in extreme environments (*5*). Due to its hardness as well as its biocompatibility, it is also used commonly for dental implants (*6*). When doped to higher levels (8-12 mol% Y), the high ionic conductivity of the stabilized cubic phase makes it an excellent electrolyte for solid oxide fuel cells (*7*). Around this doping concentration, its low thermal conductivity also makes it appropriate for coating superalloy components used in high temperature environments such as inside of turbine engines (*5, 8, 9*). Furthermore, the substantial interest in both mechanical and electrochemical applications of YSZ have resulted in a vast body of literature characterizing its properties and behaviors on a fundamental level. This work seeks to use this highly documented material as a foundation to elucidate the underlying mechanisms of flash sintering and to distinguish the role of the thermal profile from the athermal electric field effects during the process.

1.2 Sintering fundamentals

Although sintering is considered basic material science, our later discussion of mechanisms that enhance the sintering kinetics will recall and build upon these fundamentals. As such, some review may prove helpful. The following summary of sintering basics is largely based on the seminal text by Randall German (*3*).

Sintering is a complex process consisting of several simultaneous and competing mechanisms that lead to densification of an initially porous body. These mechanisms can be roughly broken down into two categories: surface and bulk. Surface mechanisms involve rearranging atoms from surface site to surface site, and as such do not contribute to the actual densification of the body, although they can change the pore geometry in such a way as to affect

the rates of mechanisms that do lead to densification. On the other hand, bulk processes transport vacancies from within the grains of the ceramic to surface sites, moving mass in the opposite direction and producing densification as the vacancies are annihilated.

Both types of transport, however, are locally driven by the curvature inherently present in a porous body. Thermodynamically, curved surfaces create pressure differentials; in physical terms, these can also be considered vacancy concentration gradients, with a concave surface introducing an increased number of vacancies. Surfaces inherently possess more energy than the bulk phase as two-dimensional defects caused by partially satisfied chemical bonds. As the magnitude of surface curvature increases, the vacancy concentration differential increases as well; thus, given enough thermal energy, atoms will diffuse to level the vacancy gradient. Because this curvature provides the driving force for both surface and bulk transport, both sets of mechanisms act to reduce the area of free surfaces as well as grain boundaries. (Although they are lower energy than completely free surfaces, grain boundaries are similarly two-dimensional defects whose higher energy state results from unsatisfied chemical bonds.) With this basis, the driving force for sintering is

$$\sigma = \frac{2\gamma_{gb}}{d_g} + \frac{4\gamma_{sv}}{d_p} \tag{1.1}$$

in which γ_{gb} and d_g are the grain boundary energy and grain size and γ_{sv} and d_p are the free surface energy and pore size. The first and second terms then describe the free surface and grain boundary contributions respectively.

In response to this driving force, there are generally considered three pathways by which surface rearrangement and bulk transport each occur, and their dominance varies based on the chemistry of the compound, the particle geometry, and the amount of energy available to the system. These mechanisms are summarized in Figure 1.1. The three transport paths between

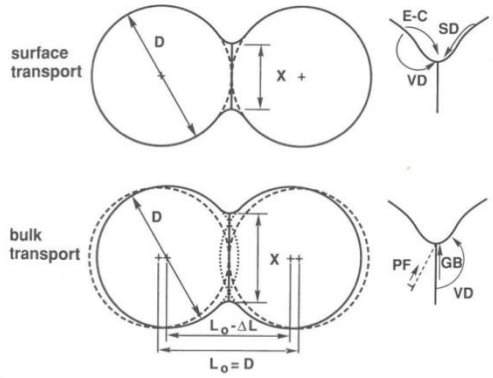

Figure 1.1 Six mass transport mechanisms occurring during sintering. E-C, SD, and VD represent evaporation-condensation, surface diffusion, and volume diffusion from surface site to surface site respectively. PF, GB, and VD represent plastic flow, grain boundary diffusion, and volume diffusion from bulk to surface respectively. Reproduced with permission from (3).

surface sites include evaporation and condensation, diffusion along the surface, and volume diffusion. Of the three, surface diffusion is considered the most prevalent due to its low activation energy; atoms can move between lower energy surface features like kinks and jogs. Volume diffusion in this context produces the same effect i.e. moving an atom from one surface site to the other; however, diffusion through the bulk is a higher energy pathway and this contributes little to surface rearrangement. Evaporation and condensation occur when the ceramic produces significant vapor pressure under the given processing conditions. In most material systems it is not considered highly relevant but can be a significant contribution when sintering more volatile ceramics.

Overall, each surface mechanism acts to decrease the curvature gradient within the body, and thus increases the bond between particles without actually bringing the particle centers closer together. When this rearrangement results in grain growth without densification, it is referred to as coarsening, and while there are applications in which this type of retained porosity with good particle bonding is desirable, the present work is generally concerned with materials in which coarsening is considered undesirable, and full densification with limited grain growth is the goal.

The traditionally “desirable” transport processes then consist of grain boundary diffusion, volume diffusion, and plastic flow. Grain boundary diffusion and volume diffusion both describe the movement of mass from the bulk to the particle neck region, along the grain boundary in the first case and through the lattice in the second. Plastic flow functions similarly, by moving dislocations to the grain boundary. As mechanisms which utilize bulk pathways, they represent higher activation energy processes. Therefore, these bulk transport mechanisms are typically considered to be more prevalent at higher temperatures, while the surface mechanisms dominate at lower temperatures.

Due to the dominance of different diffusion mechanisms at certain temperature ranges and their relationship to certain types of microstructures, sintering can be broken into three stages which are characterized by the pore structures in Figure 1.2. A powder compact begins the sintering process as a series of particles in roughly point contact; as such, the initial stage of sintering involves neck formation and growth as the contact area between the particles increases. The curvature gradients remain large and the pore network is open and connected. The intermediate stage of sintering begins when the compact reaches approximately 70% theoretical density, and is typified by the smoothing of the pores, which remain open. Once the compact reaches approximately 92% theoretical density, the pore network becomes closed and isolated; grain growth can occur rapidly in this stage as the pinning effect from pores decreases, creating intragranular pores. The onset of this effect can retarded by grain boundary doping, in which

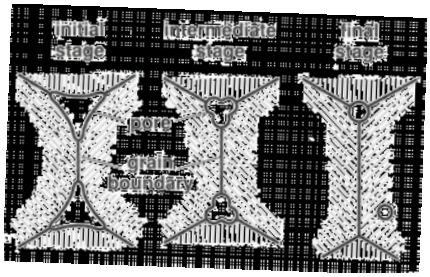

Figure 1.2 Difference in pore structure characterizing the three stages of sintering. Reused with permission from (3).

solute atoms provide an additional drag force to reduce grain boundary mobility. It is important to note that these stages can overlap significantly; as the overall compact densifies, particles are brought into contact at which point they begin sintering from the initial stage. Despite this overlap, this formalism is a useful way to discuss the degree to which certain bodies have sintered.

1.3 Field-assisted sintering and the foundations of flash sintering

A variety of techniques are used to enhance the transport mechanisms discussed above, but the present discussion is focused on those that incorporate electric fields in order to enhance the kinetics of the sintering process and retain sintered bodies with small grain sizes. This work focuses specifically on a technique called flash sintering. Flash sintering emerged in 2014 after almost 80 years of development on the related technique spark plasma sintering (SPS) (*10*), and the two techniques are often discussed with some overlap despite differences in processing parameters. This is in part because the fundamental work from which flash sintering emerged was motivated by a desire to understand the mechanisms of SPS. It is therefore valuable to begin with a brief overview of this early work.

SPS describes a process in which a powder, either metal or ceramic, is loaded into a conductive die and subjected to high uniaxial pressures and large pulsed direct currents (*10*). The high currents produce rapid Joule heating and, in combination with the uniaxial pressure, densification. SPS is most commonly used on metallic powders; when used on ceramics, the rapid heating results from Joule heating in the die rather than the ceramic body. Despite the nomenclature, significant debate still occurs within the community over the existence of actual plasma discharge between particles during the process (*11*), and the fundamental mechanisms are still under investigation.

Interested by the enhanced sintering rate and small grain size retention evidenced in the SPS of ceramics, a handful of researchers released a series of studies examining the effect of higher electric fields on the sintering rate and microstructure of ceramics (*12, 13*). This work did not use a conductive die but instead forced the current through the sample itself. Yang and Conrad had previously shown that electric fields induced superplasticity in certain ceramics, such as yttria-stabilized zirconia (YSZ) (*14, 15*); they went on to show, in a collaboration with Raj, that DC fields on the order of tens of V/cm could produce similar sintering rate effects as those seen in SPS, but at much lower currents (*12, 13, 16*). They termed the process "field-assisted sintering technique" (FAST). Around the same time, Chen et al. reported similar results obtained by the "electro-sintering" of YSZ, with the additional observation that grain growth was suppressed under these conditions until after full densification was reached (*17, 18*).

Each of these investigations used field and current values around the same order of magnitude, but the proposed underlying mechanisms differed significantly from each other. Conrad and Yang noted that the grain growth retardation appeared to be independent of temperature, and that the effect increased up to a certain field strength (~ 30 V/cm) above which no further effect on grain growth or sintering rate was realized. This concept of a limiting field was only tested using moderate fields, up to 65 V/cm (*16*). Based on their observations, they proposed that the grain growth suppression was caused by interactions between the electric field and the grain boundary space charge, which reduced the grain boundary energy, γ_{gb}. The saturation of the effect would then correspond to the reduction of γ_{gb} to zero, removing the driving force for growth. This interpretation referenced Conrad's aforementioned work on electroplasticity in ceramics, and relied on the connection developed therein between an applied electric field, grain boundary sliding, and space charge (*19, 20*).

Based on Conrad's hypothesis, the increase in sintering rate under electric field was based entirely on the suppression of grain growth. Typically, during the intermediate and final stages of sintering, grain growth occurs, decreasing the driving force in Eq. 1.1 and reducing the sintering rate; if grain growth is depressed, the grain size dependent contribution to driving force is held constant instead. Based on the relationship between grain growth and the electric field, Conrad developed an empirical model supporting the space charge approach (*16*); however, the phenomenological nature of the model limited its definitiveness. Furthermore, by appearing to establish the saturation of the effect as determined by the inherent space charge of a material's grain boundary, Conrad's work implied that the mechanism was ineffectual at higher fields.

In their collaboration, Raj, Conrad, and Yang established the early observations concerning grain size retention and the shift of the densification curve to lower temperatures (*12*). However, as Conrad developed his space charge theory, Raj argued that the applied voltage was too small to influence the space charge region; he estimated the field across the space charge, resulting from millivolts of charge displacement across nanometers of grain boundary region, to be ~10^4 V/cm, much larger than the macroscopic applied field (*13*). Rather, he relied upon the thermodynamic description of excess grain boundary energy

$$\gamma_{gb} = \Delta H_{gb} - T\Delta S_{gb} \tag{1.2}$$

in which ΔH_{gb} and ΔS_{gb} are the excess enthalpy and entropy of the grain boundary respectively. He suggested that the grain boundary resistance, higher than the bulk resistance (*21*), produced localized Joule heating which, according to Eq. 1.2, stabilized the grain boundary in a local energy minimum by increasing the entropic contribution (*13*). While both Raj and Conrad presented reasonable theories, no conclusive evidence of either mechanism was, or to this day has been, presented.

Shortly after Raj and Conrad released their work on the effect of electric fields on microstructure, Chen et al. released a series of papers discussing related experiments, but framing the mechanism as an interaction of the field with pores in the material, rather than the bulk or grain boundaries (*17, 18, 22*). He demonstrated the same enhanced sintering effect, with the additional observation that grain growth was retarded entirely only until full densification was reached, at which point rampant grain growth could occur if the temperature was sufficiently high (*18*). The other important addition from this work came from his demonstration that neutral phases in ionically conducting solids, e.g. pores and even Ar gas bubbles, migrate under field as well (*17*). Both of these effects were attributed to the transverse nature of ionic migration in this type of solid; that is, the cation migrates towards the cathode preferentially via surface mechanisms, while anions migrate towards the anode through the bulk lattice. Net mass transport results from the accumulation of cations across the pores on the cathode side and the exit of anions at the anode (while global stoichiometry is maintained by the high bulk diffusion of the anion and its ability to exchange with the atmosphere). The suppression of grain growth then in part would proceed from the difference in activation energy for grain boundary motion as compared to surface diffusion. The experiments were conducted at a low enough temperature that the grain boundaries were considered effectively immobile, but surface diffusion could still occur along pore surfaces. While this theory was specific to oxygen ion conducting solids, it clearly indicated that the interactions in this type of system are complex and poorly understood.

1.4 Flash sintering: Characteristic behavior

Flash sintering in its current form proceeded from the above work in 2010 (*1*). The first experimental setups were facilitated by pressing ceramic powder into a dogbone shape, looping Pt wires through each end to create electrodes, and suspending the sample by these wires in a

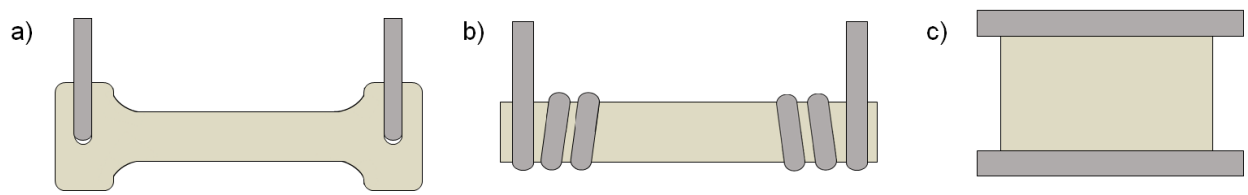

Figure 1.3 Sample configurations used in standard flash sintering experiments: a) a dogbone, b) a wrapped bar, and c) a pellet.

furnace (see Figure 1.3a). A high DC electric field (~60 to a few hundred V/cm) was sustained across the sample as the furnace temperature increased steadily (*1*); this method of heating/voltage application is referred to as a "constant heating rate" experiment. At some furnace temperature, referred to as the flash temperature (T_{flash}), the current measured through the sample increased non-linearly to the limit set on the power supply, at which point the supply switched to current-control mode and the voltage across the sample decreased. The current increase was accompanied by rapid shrinkage as the sample sintered in approximately 30 s. Examples of the electrical and shrinkage characteristics are shown in Figure 1.4. A higher electric field consistently produced a lower T_{flash} (*1*, *23*). The comparison in Figure 1.4b clearly distinguishes flash sintering from FAST; the sintering time became nearly instantaneous.

Later versions of the technique switched to isothermal furnace temperatures and ramped the electric field. This rendition, which is the most common form today, introduced the concept of an incubation time. This incubation time described the period from the application of the

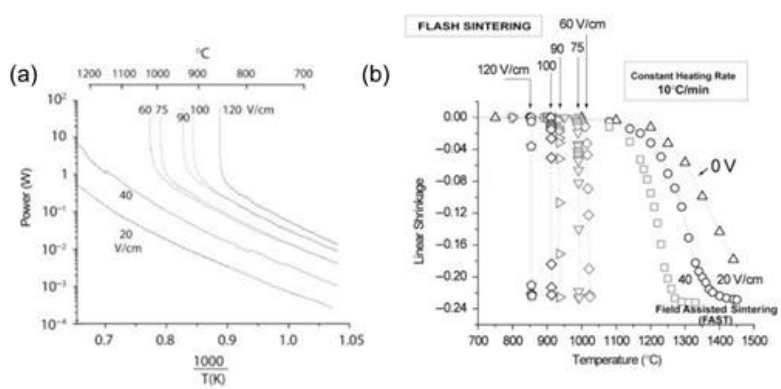

Figure 1.4 Characteristic (a) power density and (b) shrinkage versus furnace temperature during flash sintering. Reproduced with permission from (1, 2).

electric field to the nonlinear current increase. Its length decreased as the applied field increased, with times reported from 5 to 2500 seconds (*24*). (These experiments also demonstrated an increase in final density with increasing magnitude of current, although the power dissipation remained significantly lower than during SPS (*24*).) This discovery led to a formalism which describes the flash process in three stages: the incubation period (Stage I), rapid current rise (Stage II), and quasi-steady state (Stage III) (*25*).

A vast body of literature quickly developed around flash sintering, largely focused on exploring the variety of materials which could be flash sintered (*26, 27*). Alternate experimental rigs which enabled the sintering of pellets (Figure1.3c) and the use of an AC field were also developed (*28, 29*); however, the majority of foundational work at this time was performed using the dogbone suspension system or wrapped bar configurations in Figure 1.3a and b (a point which will become relevant in Chapter 3 during the comparison of our results to literature). The quantity of experiments and materials tested makes a full review impractical here; we refer you instead to reviews by Dancer (*26*) and Yu et al. (*27*) for a comprehensive overview of the variety of materials flashed and their resulting properties. What remains relevant here is the broad range of ceramics investigated, including dielectrics and semiconductors, and electronically and ionically conducting materials (*27, 30*). Furthermore, while an enhanced sintering rate was a consistent effect among materials, final microstructural features like grain size distribution depended heavily upon the specific material processed; for instance, localized grain growth was observed on the cathode in YSZ (*31*), while titania (*32*) and ZnO (*33*) displayed the same effect on the anode.

Due to the focus of this work, a short overview is given here of a few effects observed during the flash sintering of YSZ specifically. Both 3 and 8 mol % YSZ have been flash sintered

to full or near full density using both DC (*34, 35*) and AC (*29, 36*) fields, and while the empirical parameter-density relationships have generally been established, a fundamental understanding of the process has not. As mentioned above, cathode-localized grain growth has been observed in DC processed samples (*31*). Grain size gradients have also been observed between the sample center and edge resulting from the surface heat loss (*37*). Some studies report increases in bulk and grain boundary resistivity as well as grain boundary thickness in 3YSZ (*36, 38*) and 8YSZ (*39*) upon flash sintering, yet others report no difference from conventionally prepared samples (*29, 40, 41*). The origin of this intermittent observation remains poorly understood. Muccillo and Muccillo, who established one of the early AC flash sintering systems (*28*), suggested that there is a redistribution of oxygen vacancies from the grain boundaries of YSZ to the bulk during flash (*38*), while Vendrell et al. suggested that a fundamental change in defect state produced additional mobile oxygen vacancies (*39*). However, no experimental or modeling work exists to more deeply support or disprove these suggestions. Chapters 4 and 5 attempt to shed additional experimental light on this open question.

Other interesting observations during the flash sintering of YSZ include reports of photoemission (*25, 42*) and color front formation (*43*) during flash. The former was originally credited to electron-hole creation and recombination and linked with the increase in electrical conductivity. Since then, there has been some dispute over the validity of this explanation; similar photoemission was reported during the flash of other materials and could be explained adequately by thermal radiation (*44*). On the other hand, the color front formation was a clear indication of chemical reduction which commonly manifests in YSZ as “blackening,” or the appearance of brown or black color centers (*45*).

1.5 Flash sintering: Proposed mechanisms

Despite the profusion of empirical data, a fundamental understanding of the mechanisms of flash sintering has remained elusive; in particular, the rapid rate mass transport required to produce densification in a matter of seconds puzzles researchers. Several theories have been suggested, which tend to each emphasize different physical processes known to occur under high fields and currents, but it remains unclear which process is primarily responsible for densification. The core of the debate centers on the relative thermal and athermal field contributions to the densification and resulting properties. We review here the three predominant theories and relevant supporting evidence.

1.5.1 Defect nucleation and avalanche

The defect avalanche theory was one of the earliest proposed explanations for flash, and it is founded on the concept that the Joule heating created by power dissipation is insufficient to produce the kind of rapid densification observed here (*46*). Instead, the defect avalanche theory suggests that under a high field, Frenkel defects are created at an enhanced rate, facilitated by a local reduction in the ionization energy (*47, 48*). The argument uses classical thermodynamic nucleation theory to demonstrate that the polarization energy of the excess defects would be lowered by their agglomeration; this decrease, balanced by the increased interfacial energy between the nuclei and rest of the lattice, results in some critical nuclei radius. Because the nuclei are composed of aligned defect dipoles (Frenkel vacancy-interstitial pairs), they would represent areas of high dielectric constant (*49*). The nucleation event would explain the observed incubation time, and the decrease in incubation time with increasing electric field was explained by the relationship between the applied field and the value of the critical radius. The model was initially appealing because a dependence of the flash event on Frenkel pairs could potentially

explain the rapid mass transport. It also utilized a credible physical process (i.e. enhanced ionization under field).

Empirically, large oxygen vacancy concentrations are often correlated with flash sintering, although the increase in vacancy concentration has not, to this point, been separated from the effect of increasing temperature. Cathodoluminscence of flash sintered ZnO (*50*) as well as a couple of in-situ diffraction studies (*51, 52*) indicate that oxygen vacancy creation at least is enhanced during flash sintering relative to conventional sintering. However, Shomrat et al. performed an experiment in which they fixed the defect concentration in $SrTi_{1-x}Fe_xO_{3-\delta}$ via doping and used oxygen partial pressure to vary resistivity independently of point defect concentration (*53*). This decoupling allowed them to demonstrate that flash was independent of defect concentration, but instead dependent upon resistivity. Alternately, attempts to support this theory via modeling have resulted in a lone paper which demonstrated via molecular dynamic calculations that, within an energetic window of lattice vibrations and temperature ($T_{Debye} < T < T_{melt}$), a concentration of Frenkel pairs greater than the thermodynamic value could be generated (*54*). However, the results were limited to single crystal aluminum and a mechanism connecting an electric field as the source of the required lattice excitations was not proposed. Regardless, proponents of this theory have sought to link the Debye temperature to the flash temperatures of various oxides (*55*). Unfortunately, the degree of complication involved in this theory out makes it difficult to either prove or disprove.

1.5.2 Localized grain boundary melting

The theoretical basis for a liquid-mediated densification mechanism proceeds from the SPS literature and has been primarily advanced in a series of papers by Chaim (*56, 57*). The theory establishes grain boundaries as areas of high resistivity and focal points for the electric

field and proposes that the resulting current concentration produces a thin liquid phase, a few atoms thick, at the grain boundaries of the ceramic (*56*). This liquid phase would be responsible for the onset of non-linear conduction due to the increased conductivity of the liquid phase relative to the solid matrix. In this case, the capillary forces acting on the liquid phase would produce the rapid bulk consolidation (*56*).

There is some limited experimental evidence supporting the existence of a transient liquid in certain flash sintered material systems. Corapcioglu et al. observed a core-shell microstructure in the grains of flashed sintered $K_{0.5}N_{0.5}NbO_3$ (KNN) and used TEM and EDX to correlate the measured compositions to those in the liquid portion of the KNN phase diagram (*58*); this observation was replicated later by Serrazina et al., again in KNN (*59*). Other systems have shown evidence of localized melting and possibly vapor phase mediated crystal growth, including ZnO (*33*) and YSZ (*29*); however, these areas are localized to the anode, implying a dependence on the overall field gradient, rather than microscopic internal gradients. Finally, Biesuz and Sglavo found evidence of grain boundary melting and oriented grain growth in corundum, but based on the orientation of the growth direction and a comparison of the grain boundary kinetics/thermodynamics when a liquid phase is introduced, they suggest the liquid acted only to pin the grain boundaries (*60*). If grain boundary melting is the predominant densification mechanism during flash sintering, evidence of a transient liquid phase would be expected in a broader range of materials. The concept has been also criticized for not adequately considering rapid conduction of heat away from the grain boundaries through the crystal matrix (*61*).

1.5.3 Thermal runaway model

Five years after the first publications on flash sintering, a few groups independently published a mathematical model for the onset of flash sintering referred to now as the thermal runaway model. The mathematical formalisms varied between the groups, but the general approach remained the same (*30, 33, 62-64*). The model proposed that the basis for flash is the balance between radiative cooling from the sample surface and the negative thermal coefficient for conductivity in most ceramic oxides. In each case, the model assumed an Arrhenius expression to describe conductivity and standard heat transfer equations. Under an electric field and a high enough furnace temperature, Joule heating and conductivity were predicted to form a feedback loop and at a critical field or temperature, rapidly overcome the radiative cooling of the sample. The non-linear current increase in this case would result from the rapidly increasing temperature of the sample rather than a change in conduction mechanism. Using this approach, flash temperatures have been reasonably well-modeled for YSZ (*63*) and $BaTiO_3$ (*62*).

This theory is distinguished from the earlier two by the depth of the modeling work which supports it. In addition, it agrees with the correlation throughout literature of higher conductivity materials with lower flash temperatures. This dependence on resistivity was neatly demonstrated in the aforementioned work by Shomrat et al. (*53*) as well as the similar T_{flash} dependence of other materials on atmospheric conditions which enhanced their conductivity (*65*). However, while thermal runaway is now broadly accepted as the trigger for flash sintering, the modeling in literature has focused exclusively on describing and predicting flash temperatures; it has not been extended to actually explain and model the mass transport aspect.

Conceptually, the contribution of thermal runaway to densification references back to a small body of work on the fast firing of ceramics in the absence of electric fields. For example,

earlier work from Harmer et al. showed that introducing alumina to a pre-heated furnace at 1850°C densified the pellets to theoretical density in 15 minutes (*66*); similar effects were attained in alumina even at lower furnace temperatures (*67*), and in nano-grained YSZ, full densification was achieved in 1 min at 1300°C (*68*). While this process has not been extensively modeled or theoretically developed, some work proposed that the thermal gradient that develops between the sample surface and the center during rapid external heating enhances the driving force for diffusion (*69, 70*). Biesuz and Sglavo modelled the contribution from this effect in flash sintering, known as the Soret effect, and found that sufficiently high temperature gradients could accelerate sintering at intermediate densities (*71*). In their work, however, it was assumed that the gradient would have to develop across the short distance between particle bulks and grain boundaries in order to reach the required magnitude (10^6 K/m). Developing this kind of gradient across the bulk of a sample, as would occur during fast firing, seems unlikely.

It has alternately been proposed that a rapid heating rate simply limits grain growth by activating high temperature densification mechanisms more quickly, thus increasing the densification rate (*72*); this represents a more traditional interpretation of sintering kinetics. Roura et al. demonstrated, using Ashby's basic sintering model, that a fast heating rate with standard diffusion mechanisms was sufficient to reproduce the shrinkage profiles observed in fast firing (*73*). In flash sintering, this suggestion is supported by the correlation of smaller particle sizes (which provide a higher driving force for sintering) with lower flash temperatures (*74*). The flash sintering community added a couple of studies to this body of work which compared rapidly heated ceramics produced through a variety of techniques to DC flash sintered ceramics (*61, 75*). They found similar relationships between heating rate and rapid densification,

but declined to make strong statements concerning the fundamental origins. Rather, their work served to support a predominantly thermal basis for the characteristics of flash sintering.

1.6 Absolute temperature during flash sintering

The feasibility of a predominantly thermal basis for flash sintering depends heavily upon the absolute temperatures and heating rates present during flash sintering. One focus of the present dissertation was to distinguish the thermal effects of flash sintering; thus measuring the temperatures present during flash became relevant. Similarly, other researchers have expended substantial effort on obtaining accurate in-situ temperature measurements during flash using a variety of techniques. The major temperature prediction and measurement techniques used are each discussed briefly below along with their strengths and weaknesses, and the overall results are summarized in ***Table 1.1***. This section aims to give the reader a general sense of the state of this important area of study, and the range of findings it has reported, rather than an exhaustive list of temperature studies in flash sintering.

1.6.1 Temperature predictions: Blackbody radiation model

Up to the present, the body of flash sintering work has leaned heavily on the black-body radiation (BBR) model to estimate sample temperature. Introduced in studies as early as 2012 (*46*), the model uses a steady-state, homogeneous formalism of heat flow to estimate sample temperature as a balance between Joule heating and radiative heat loss. This balance yields the following:

$$T_{sample} = \left(T_f^4 + \frac{P}{A\sigma\varepsilon} \right)^{\frac{1}{4}} \tag{1.3}$$

in which T_f represents furnace temperature, P is the power dissipated via Joule heating, σ is the Stefan-Boltzmann constant, ε is sample emissivity, and A is the sample surface area. While the simplicity of this expression gives it merit as a first approximation, the model makes several

assumptions, some explicit and some implied, which introduce substantial inaccuracies to its results.

First, this expression ignores the contribution of sample geometry and inhomogeneous conductivities to the thermal profile, which can modulate both heat loss and heat generation. As stated in (*46*), Eq. 1.3 ignores convective and conductive losses to both the furnace environment and the sample electrodes. While this assumption may be considered reasonable in the early flash sintering experiments, which featured dogbone samples with limited electrode contact, cylindrical green bodies contacted by flat Pt electrodes are now frequently used. The amount of increased contact area with a more thermally conductive material introduces error on the order of >100°C to the basic BBR model, as Charalambous et al. demonstrated (*76*). Alternately, in the dogbone configuration the electrodes have been predicted to contribute localized Joule heating due to concentrated contact resistance, which the BBR model also fails to accommodate (*77*).

Next, as stated above, the formalism uses equations for steady-state heat transfer, assuming a uniform body temperature and ignoring transient thermal effects. These assumptions remove the likely possibility of internal temperature gradients between the sample surface and center, which have been calculated to be substantial (*63, 77*). Furthermore, the relationship between heating rate and the rate of sintering, as demonstrated by the history of rapid-rate sintering (*61, 67*), indicates that the transient region of Stage II, rather than the steady-state period, is when most densification occurs and is therefore fundamental to flash sintering.

Third, the model is often implemented by expressing power dissipation as I^2R, in which sample resistance R is represented by an Arrhenius expression. The use of a single Arrhenius expression implies a constant conduction mechanism, an assumption which has been disproven during the DC flash sintering of oxygen ion conductors such as YSZ (*78, 79*), TiO_2 (*32*), and

CeO_2 (*80*); such oxides become mixed conductors under high fields (*81*), which substantially increases their conductivity independent of temperature. Although using the experimentally measured power to estimate the thermal balance partially mitigates this issue, it does not compensate for the spatial character of the reduction process, which introduces a thermal inhomogeneity as reported in (*82*) and further discussed in Chapter 3.

Finally, the model requires an accurate expression of the emissivity, which can vary not only with temperature, but with density and grain size as well (*83*). While papers invoking the BBR model often acknowledge the importance of the emissivity factor, – Du et al. note that a difference between an emissivity of 1 and 0.7 in their model would result in a variation of 136ºC (*84*) – no calibration is ever performed to compensate for this important factor. Rather, a constant emissivity is assumed: typically either the ideal value of 1 or e.g., in YSZ studies the value of 0.7 reported for dense 5.3YSZ between 127-577ºC (*85*) is utilized. This assumption can result both in absolute temperature inaccuracies as well as error which changes as the sample densifies.

Too many studies have used the BBR model for temperature estimates to mention them all here; however, the temperatures generated not often central to the argument of a particular study but is more often used as a general estimate. Using this model, temperature values for YSZ have been predicted to range from 1400ºC (*77*) to 1600ºC (*63*). More recently, the BBR model was modified to include heat loss via electrodes; when compared to diffraction-based measurements, this adjustment substantially improved the accuracy of the result (*86*).

1.6.2 Temperature predictions: Finite element method

Surprisingly, only a few studies have used the finite element method (FEM) to estimate the temperature during flash. The more sophisticated nature of FEM, particularly in commercial

software packages, improves on the BBR model by allowing temperature gradients and incorporating electrical and thermal contact resistances. Unfortunately, the increased nuance can also introduce error if accurate values for the contact resistances are unknown. FEM studies predict a wide range of temperatures during flash, from 1232°C for 3YSZ (*37*) to 2272°C for 8YSZ (*87*) at the sample center. Predicted gradients range from 25°C to >1000°C between the center and edge. The study which reports the highest value notes that the gradient is unexpectedly high, and suggests that may be a major factor in densification.

1.6.3 Optical measurements

Optically-based techniques have been popular from the early days of flash sintering, usually in the form of a pyrometer. However, the absolute value of these measurements is often limited for two reasons: first, because no calibration is performed to compensate for emissivity value, reflections from ambient conditions, etc.; and second, because spot pyrometers are typically used which sample a limited portion of the ceramic. These obstacles are not insurmountable, but do require careful calibration to produce an accurate measurement (see §2.3 for a more thorough discussion). Issues in calibration may explain the spread in the measurements summarized in this portion of ***Table 1.1***, which range from 1000 to almost 1700°C. As Chapters 2 and 4 will discuss in more detail, substantial effort was put into this work's investigations to arrive at an accurate temperature measurement method using an optical technique, which also allows for improved temporal and spatial resolution.

1.6.4 Diffraction measurements

More recently, several in-situ studies have been performed using diffraction measurements. These studies commonly used 3YSZ or TiO_2, although $BiFeO_3$, ZnO, and CeO_2 were recently tested as well. In some cases, the temperature of the sample was determined via

diffraction based on the thermal expansion of a strip of Pt set into the side of the sample; in other cases, the sample itself was calibrated for thermal peak shifts before performing the flash experiment.

Comparing the temperatures measured between different materials is of limited value as the peak temperature will vary based on sample conductivity and specific heat, but the technique has proved useful in correcting temperatures predicted by the BBR model. For instance, in the DC flash sintering of ZnO, the BBR model predicted temperatures ranging from ~188 to 581°C higher than those measured, depending on the starting temperature of the furnace and the current density (*88*). Adjustments to the emissivity constant could not explain the discrepancy, and in a later related paper, several of the same authors to modified the model to include conductive losses from the sample electrodes, as mentioned previously (*86*). These diffraction studies have proven valuable both in reporting accurate temperature measurements during flash as well as establishing that the temperatures present during flash sintering are often comparable to those used in conventional sintering. For YSZ, temperature measurements have ranged from 1400-2000°C; note that the upper value reported used an unusually high current density.

While diffraction studies represent the most accurate measurement of average steady-state flash temperature to date, the technique is limited by spatial and temporal resolution. The low spatial resolution means that internal temperature gradients, resulting from surface heat loss or DC electrochemical reduction, are averaged together; and unfortunately, most of the studies listed in ***Table 1.1*** were performed using DC fields. However, the time resolution represents a possibly greater loss of information, as the 0.5-1 s resolution reported in the above studies allows for at most 1-2 data points during the most interesting and relevant part of the flash sintering experiments.

Table 1.1 *Summary of in-situ temperature predictions and measurements from literature.*

Technique	Max Temperature	Material	Year/citation
Impedance spectroscopy	>2000ºC	Dense 8YSZ	2013 (*89*)
Optical measurements	1100ºC	Porous 3YSZ	2011 (*90*)
	~1500ºC	Green 3YSZ	2014 (*25*)
	~1680ºC	Green $MgAl_2O_4$	2016 (*91*)
	~1575ºC	Green Y_2O_3	2014 (*92*)
	~ 1300ºC	Dense 8YSZ (single + polycrystal)	2018 (*79*)
BBR model predictions	~1600ºC	3YSZ	2015 (*63*)
	1436ºC	3YSZ	2018 (*77*)
	1885ºC	ZnO	2018 (*88*)
FEM simulation	1640ºC	3YSZ	2011 (*93*)
	2272ºC	8YSZ	2015 (*87*)
	1232ºC	3YSZ	2016 (*37*)
	1580ºC	3YSZ	2018 (*77*)
Diffraction measurements	1290ºC	Porous 3YSZ	2015 (*52*)
	~1700ºC	Green 3YSZ	2015 (*42*)
	~1400ºC	Dense 3YSZ	2016 (*94*)
	925ºC	Dense TiO_2	2016 (*95*)
	1250ºC	Green TiO_2	2018 (*51*)
	1300ºC	Green ZnO	2018 (*88*)
	~1460ºC	Green TiO_2	2018 (*86*)
	~1150ºC	Green CeO_2	2018 (*80*)
	>2000ºC	Green 8YSZ	2019 (*76*)
	~783ºC	Green $BiFeO_3$	2019 (*96*)

1.7 Nature of electric field effects on ceramic microstructures

Empirically, the traditional understanding of sintering mechanisms in combination with rapid heating and high temperatures reached during flash sintering appear sufficient to at least phenomenologically explain most characteristics of flash sintering. However, the possibility of some influence from the electric field cannot be entirely discounted, not only because it is difficult to definitively disprove, but also because experimental evidence of field interactions with ceramic microstructures does exist. Some early work in this area was already discussed in

§1.3, but recently a few truly robust studies have been published which provide strong evidence of field effects on microstructure, specifically with respects to grain boundary mobility.

While sintering is a complex process involving many interacting mechanisms, studying grain growth specifically in pre-densified samples allows for simpler and more fundamental observations of field interactions. Rheinheimer et al. performed a carefully controlled pair of studies in this area using the seeded polycrystal technique on $SrTiO_3$ with current-blocking electrodes to prevent effects from Joule heating (*97, 98*). They found that grain growth was enhanced at the negative electrode. Using a thermodynamic treatment, they demonstrated that the oxygen chemical potential gradient which develops under a DC field reduces the space charge at the negative electrode. The reduction in space charge reduces defect segregation to the grain boundaries, thereby decreasing the amount of solute drag and increasing grain boundary mobility. Dong et al. observed similar results in pre-densified 8YSZ; that is, both electrochemical reduction and atmospheric reduction were correlated with faster grain growth (*99*). These observations are in line with other, less finely controlled sintering studies which report enhanced grain growth on the cathode in YSZ (*100*), and on the anode in TiO_2 (*32*) and ZnO (*33*). Note that, in each of these studies, there was no direct effect observed from the electric field; rather, the effect of the bias on grain size was mediated by a chemical potential gradient.

Notably, these observations in controlled systems contradict the common correlation of flash sintering with grain growth suppression. This discrepancy indicates that the effect of the electric field is either thermal – i.e., grain growth suppression due to rapid rate sintering – or electrochemical, manifest as enhanced grain growth. A comparison of AC field-assisted sintering to DC from Conrad's work supports this concept. Conrad's studies on moderate electric fields

indicated that an AC field was equally effective as a DC field in suppressing grain growth (*101*); this is explicable by the increased sintering rate via Joule heating, effective in both AC and DC. If some direct interaction between the electric field and grain boundary occurred, differences in the AC and DC behavior would be expected.

1.8 Deconvolving thermal and athermal electric field effects

In most of the flash sintering community, thermal runaway has gained general acceptance as the explanation for the onset of flash sintering. However, significant debate is still present over the relative roles of the electric field and rapid heating on densification during flash. A predominantly thermal basis for densification is far from ubiquitously accepted, and the role of the field in mass transport remains poorly understood. Whether traditional diffusion mechanisms are sufficient to explain rapid densification or some novel mechanism is at work remains debated. The following chapters aim to detangle some of the complicating aspects of flash sintering by varying first the electrochemical boundaries of the system, then the thermal profile, and finally the electrical frequency. Our work indicates that field effects are minimal and that many of the “inherent” benefits of flash lie in the rapid rate of Joule heating and densification rather than a direct field effect.

CHAPTER 2

Experimental Design and Analytical Techniques

The experiments discussed in the following chapters required in many cases a non-trivial amount of design, and understanding the results requires a reasonable understanding of the physical details of the experiment. Therefore, while the specific parameters used in each experiment are discussed in their relevant chapters, the general physical setups are discussed here. The preparation of green bodies varied in some ways from experiment to experiment, and as such the powder and preparation details are also left to their respective chapters. On the other hand, most of the analytical techniques used in the following studies are well-known and used in a common or straightforward way (e.g. SEM for grain size analysis) and require no background discussion. The exceptions to this are infrared (IR) measurements and impedance spectroscopy. As such, this chapter includes the development of our IR measurement method and a short discussion of the application of impedance spectroscopy.

2.1 DC flash sintering experimental setup

The DC flash sintering experiments were performed using a horizontal dilatometer built by a previous graduate student (*102*). The dilatometer, whose sample holder is shown

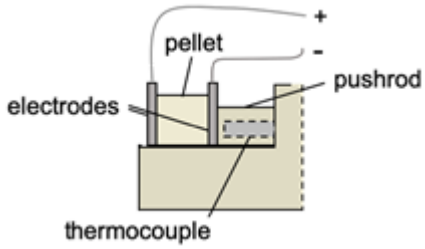

Figure 2.1 DC flash sintering sample holder.

schematically in Figure 2.1, sandwiched a pellet between two electrodes. A pushrod applied 0.002-0.05 MPa of pressure to the stack via an external set of weights; the number of weights could be modified to apply different amounts of pressure. A thermocouple, which was fed through the pushrod, monitored the sample temperature, separated from the sample by 1.6 mm of alumina. The electrodes were connected to sheathed Pt wire, which fed out of the furnace to a DC power supply capable of up to 300 V and 3.5 A (Sorenson DCS 300-3.5A).

The power supply was controlled by a Labview program which monitored the current, voltage, shrinkage, and temperature of the sample and controlled the electrical output of the DC supply. The program allowed for two forms of flash sintering experiments. The first was constant heating rate experiments, in which the furnace heated the sample while a field was applied; when either a set maximum temperature or current was reached, the program would delay for a set period of time, then turn off both field and furnace. For isothermal experiments, the furnace was first heated, then the sample was inserted and the field was stepped and held until a preset current limit was reached; the current was held for a specified dwell time.

2.2 AC flash sintering experimental setup

For the AC flash sintering experiments, a vertical furnace was modified to add several features:

1) a suspended and mobile sample holder which enabled the option of a gravity-fed electrode contact instead of a weighted one;
2) an external frame and linear actuator which moved the sample holder between a processing position in the furnace to a loading position below the furnace;
3) a viewport which accommodated IR monitoring of sample temperature; and

4) a quench rod which extended from outside the furnace into the sample holder so that the sample could be pushed from the holder to drop out of the furnace i.e. rapidly quenched to room temperature.

The full experimental setup used for AC flash sintering is shown in Figure 2.2. The electrodes connected to an AC power supply (Pacific AMX-360) capable of up to 135 V_{rms} and up to 17 A_{rms}. The output was controlled by proprietary software produced by Lucideon, Ltd., which was available for use in our laboratory via our collaboration. The software not only monitored the electrical output and enforced current and voltage maximums, but it introduced control of the current ramp rate, a parameter which features heavily in Chapter 4.

Flash sintering experiments were performed by loading the pellets into the holder in loading position, then raising the holder to the processing position. Samples were allowed to thermally equilibrate for 10 minutes. An IR camera (FLIR SC8300HD) recorded the sample temperature through an IR transparent NaCl window. Sample shrinkage was estimated from the IR footage based on the change in dimension, and calculated as $\frac{\Delta V_i}{V_o} = \frac{r_i^2 l_i}{r_o l_o} - 1$ where the subscript

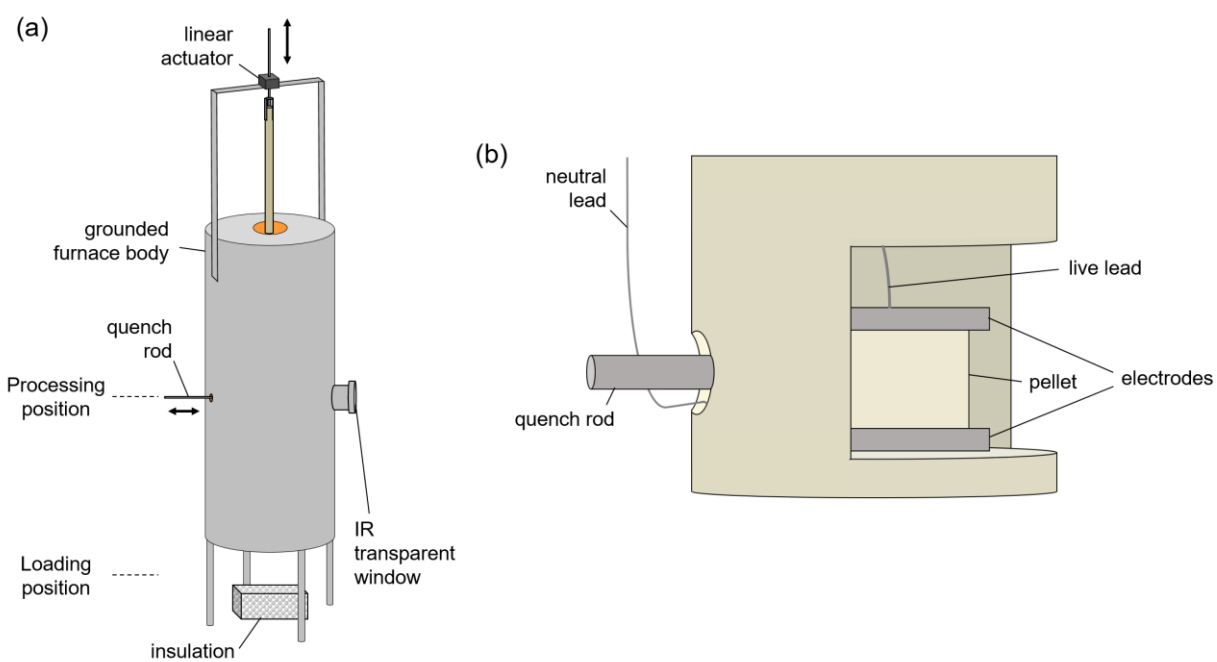

Figure 2.2 (a) Overall AC flash sintering setup and (b) close-up of the sample holder.

i indicates the instantaneous value. After current and voltage were applied, samples could be quenched by using the rod shown in Figure 2.2, or removed manually by lowering the holder to the processing position.

2.3 IR temperature measurement calibration and data analysis

2.3.1 Empirical corrections to IR temperature values

On the surface, infrared-based temperature measurements appear to be fairly straightforward; infrared radiation is collected and translated into temperature via the Stefan-Boltzmann law. However, the simplicity of fundamental blackbody predictions quickly degrades as one attempts to correct for experimental factors.

The Stefan-Boltzmann law expresses the power flux radiated from an ideal hemispherical blackbody

$$j = \sigma T^4 \tag{2.1}$$

The simplicity of the above expression masks a number of assumptions which will deviate from actual experimental conditions, especially those which are performed in furnaces not equipped to control for errant signal. First, the expression is derived from an integration of Planck's law from frequency $\nu = 0$ to ∞

$$\frac{P}{A} = \int_0^{\infty} \frac{2h\nu^3}{c^2} \frac{1}{\exp\frac{h\nu}{kT} - 1} \cos\theta \, d\Omega \tag{2.2}$$

in which h, c, k, and T have their usual meaning, and P and A are power and surface area respectively. The integration range in the first integral would need to be corrected for the actual measurement range of the spectrometer or detector. Second, in order to integrate the second term, an accurate expression of the solid angle, $d\Omega$ in the second integral, must be chosen based on the geometry of the emitting body and its relation to the detector. The form shown in Eq. (2.1

assumes the solid angle expression for a hemisphere. Third, Eq. (2.2 would need to be scaled down for the non-ideality of the emitting body i.e. $\varepsilon < 1$.

In theory, these corrections could be made, and a reasonable spectrum calculated, if all other experimental conditions were controlled. The setup used in these experiments, however, contains the added complication of exposed furnace elements. A non-ideal blackbody exhibits a reflectivity of (1- ε), which means IR emissions from the background are reflected from the sample surface and mix with the sample signal. In the case of background furnace elements, this interference results in artificially high temperature measurements. In other cases, this complication can manifest as an artificially lower temperature due to, e.g., reflection from the sky in outdoors measurements.

Due to the above complications, an empirical correction to our IR measurements seemed likely to produce the most accurate results, as opposed to a fundamental calculation. The need for a calibration was based on 1) good practice and 2) the possibility that the emissivity, and therefore signal conversion, would differ for dense and green pellets, and thus need to be specific to each case. Thus, a set of temperature measurements was taken of both green and dense (conventionally sintered) pellets at furnace temperatures from 600 to 1050°C using both the IR camera and a calibrated thermocouple in contact with the sample. The pellets were allowed to equilibrate at each temperature for 20 minutes; based on the thermocouple measurements, the vast majority of the temperature change occurred within the first 5-10 minutes.

The IR and thermocouple measurements are presented in Figure 2.3. The IR camera reads a temperature which was consistently elevated relative to the thermocouple with a degree of error higher than the manufacturer’s reported value of 2%, shown as the error bars in Figure 2.3a.

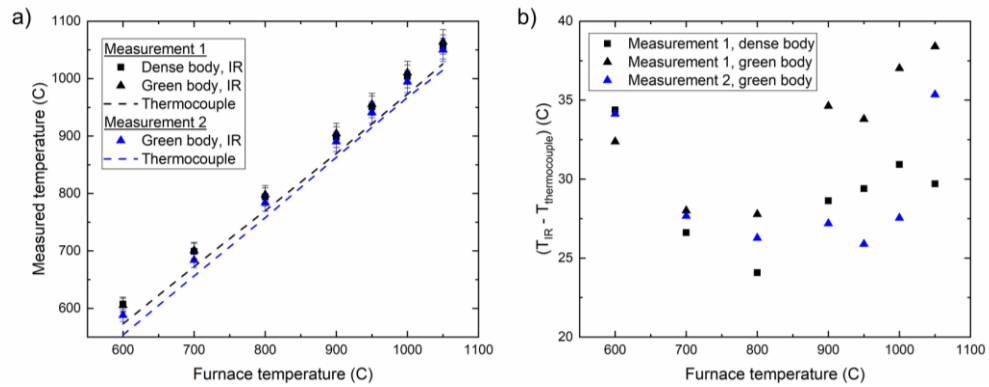

Figure 2.3 (a) IR and thermocouple measurements used in calibrating the IR measurements and (b) the absolute error of the IR measurements, calculated as the deviation from the thermocouple measurement.

Were this error due to an inaccurately high value of emissivity in the camera software (which was already set to the maximum value of 1), the direction of the error would have been lower, not higher, than the thermocouple reading. Any physically possible emissivity correction would have exacerbated, rather reduced, the error. We therefore credited the differential to reflection from the furnace elements, which would be at a higher temperature than the contents of the furnace.

There are two other conclusions from Figure 2.3 which are relevant to the development of the data correction. First, the dense and green body readings did not differ substantially across the temperature range measured; therefore, any variations in the value of emissivity with density could be discounted in this case. Second, the magnitude of the error remains fairly constant across the temperature range considered, between about 25 and 35 degrees. Finally, a sampling of the calibration data was also plotted spatially to see whether there were spatial inhomogeneities introduced to the temperature correction factor by e.g. uneven positioning of furnace elements. The spread of temperature measurements across the sample fell within 0.5% of the average sample temperature, so spatial inhomogeneities were considered negligible.

Altogether, these results indicated that a single, constant IR correction factor would be valid during a given flash sintering experiment with a constant furnace temperature. The exact

value of the offset, however, should vary with the sample's orientation to the furnace elements and the element temperature; while the sample position during flash sintering experiments is kept as consistent as possible, the nature of empirical work introduces some natural variation in angle. Based on the thermocouple measurements, a properly equilibrated sample would be at ~1020°C at the beginning of each experiment which uses a 1050°C furnace temperature (the offset from the furnace set point was likely due to the substantial convention which occurs in a vertical furnace). Thus, for all IR data reported in this document, a correction was calculated for each experiment individually as the offset between 1020°C and the starting temperature from the first few frames of the IR recording, before the current is turned on. This process typically results in a reduction of the reported IR temperatures by a few tens of degrees. Based on the measured offsets in Figure 2.3b, this correction appears sufficient for our purposes.

2.3.2 Data processing

After collection, the IR data was exported from FLIR's Research IR software as a set of .csv files and processed using a Matlab script written for this work. The script performed several tasks:

1) Calculation of average starting temperature and correction factor.
2) Trimming of each frame to reduce data size.
3) Automated sensing of sample dimensions in each frame using the difference between pellet and background temperatures.
4) Calculation of sample temperature statistics using the pixel framing established in (3).

The temperature statistics were calculated by treating each pixel within the sample dimensions as a separate measurement. Each sample was typically ~25x40 pixels; the edge pixels tended towards a temperature lower than the rest of the sample due an averaging effect with the

background and the extreme observation angle at the sample edge; see Figure 2.4a for an example of one frame and its boundaries. This sampling resulted in a skewed profile and as such, when a single representative temperature measurement is required in this work, the median temperature is reported, along with the first and third quartile (as opposed to the average and standard deviation, which are dramatically reduced by the skewed profile), as shown in Figure 2.4b. Note that this range typically falls within the manufacturer-reported error of 2%.

Finally, we note that the thermal profiles measured appeared fairly reproducible between repeat experiments; as an example, the thermal profile of two experiments performed under identical conditions is shown in Figure 2.4b. Any variation was within the accuracy of the camera.

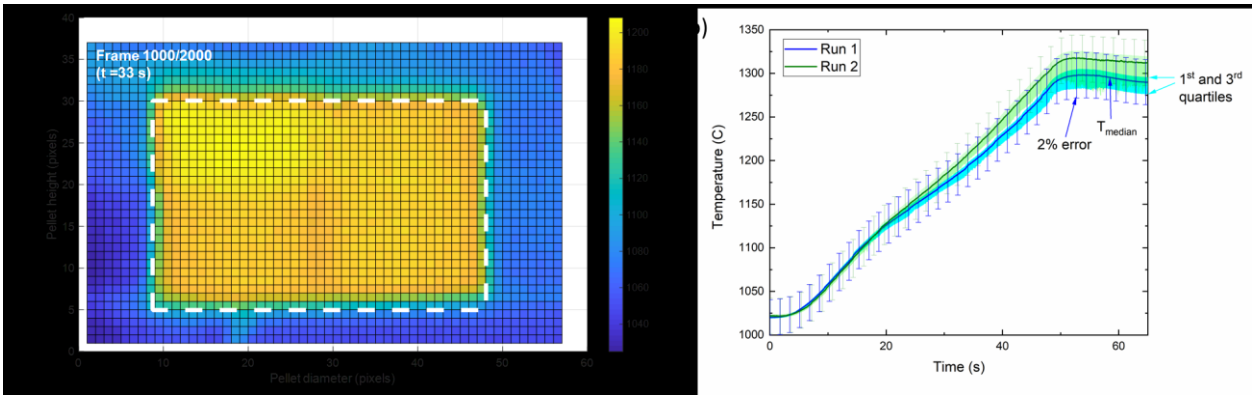

Figure 2.4 (a) One frame of IR data showing its sample dimension boundaries and (b) fully processed and reported temperature measurements from two experiments performed using the same conditions. Data from (a) and (b) are from experiments performed using 3 A of current, a $6x10^{-5}$ A/ms current ramp rate, and 1000 Hz.

2.4 Impedance spectroscopy and equivalent circuit fitting

2.4.1 Overview of impedance spectroscopy

Impedance spectroscopy is a powerful method of electrical characterization which can illuminate many material properties and behaviors if utilized properly. At its core, it is an AC electrical measurement, although it can be combined with an underlying DC bias, in which the sinusoidal signal $V_t = V_o\sin(\omega t)$ is input and the resulting output $I_t = I_o\sin(\omega t + \varphi)$ is measured

(*103*). The phase shift, φ, is based on the time response of the circuit being measured. In a general sense, φ is associated with dielectric loss; in an ideal, pure resistor, φ = 0, whereas φ of a pure capacitor is 90° (*104*). The overall loss then is described by the real component of the impedance, which follows from the I-V signal via Ohm's law: $Z = V_t/I_t$. Impedance is most commonly expressed as the imaginary number Z = Z' + jZ", where the real part is resistance (loss) and the imaginary component is reactance (energy stored).

By measuring impedance across a range of frequencies, the contribution of various conduction and polarization mechanisms can be established. The general nature of each active mechanism is identified both by the relative frequencies to which it responds ($f_{bulk} > f_{grain\ boundary} > f_{electrode}$) as well as its capacitance ($C_{bulk} \sim 10^{-12}$, $C_{grain\ boundary} \sim 10^{-11}$-$10^{-8}$, $C_{electrode} \sim 10^{-7}$-$10^{-5}$) (*105*). Quantitative analysis of the respective contributions can be extracted by equivalent circuit fitting, in which the response of each physical mechanisms is modelled as one or more electrical circuit elements. The most commonly used elements are R||C elements, parallel combinations of a resistor and a capacitor, and R||CPE elements, in which the capacitor is replaced by a constant phase element (CPE). The CPE simply relaxes the ideal behavior of a capacitor; mathematically,

$$Z_{capacitor} = \frac{1}{j\omega C} \tag{2.3}$$

while

$$Z_{CPE} = \frac{1}{Q\ j\omega^{\ n}} \tag{2.4}$$

The value of n describes the degree of non-ideality; a value of n close to 1 indicates only a slight deviation. Physically, this relaxation is usually credited with a dispersion of physical properties. The parameter Q can be converted into capacitance in an R||CPE circuit via the following expression (*106*):

$$C_{CPE} = \frac{QR^{\frac{1}{n}}}{R} \tag{2.5}$$

2.4.2 Equivalent circuit fitting of YSZ

This work is not concerned with the identification of unknown conduction/polarization mechanisms, although impedance spectroscopy can be used for that purpose; rather, in order to observe quantitative changes in the conduction mechanisms, it relies on a substantial body of literature which has already established the mechanistic contributions to the impedance spectrum of YSZ. Impedance spectra of polycrystalline YSZ are commonly represented on Nyquist plots (complex versus real components of a parameter) in which three distinct contributions are clear: bulk ion (or oxygen vacancy) conduction, a grain boundary contribution, and sample/electrode interface effects (*107*). A sample spectrum from this work is shown in Figure 2.5a. The bulk and grain boundary contributions are typically represented by either an R||C or R||CPE element, while the electrode contribution is often assumed to be a diffusion-related element called a Warburg component. The electrode element is often fit only to the detriment of the overall fit quality; as such, its contribution is not considered in this work. An example of fit and corresponding equivalent circuit are shown in Figure 2.5. In this work, all fitting was performed using EIS Spectrum Analyser software (*108*).

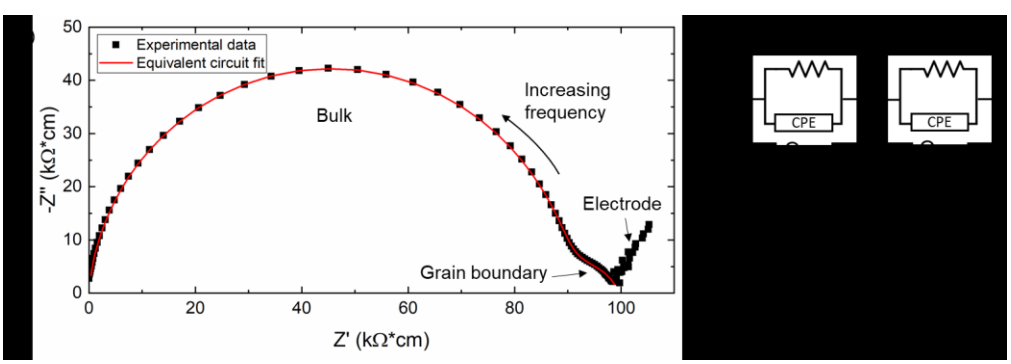

Figure 2.5 (a) Impedance spectrum of polycrystalline 8YSZ from this work and (b) the equivalent circuit commonly used to fit YSZ spectra.

2.4.3 Brick layer model analysis of polycrystals

When comparing the quantitative contributions of grain boundaries between different samples, it is impossible to draw any conclusions without compensating for the microstructure of each sample. In the same way that the resistance of the bulk must be normalized by the bulk sample dimensions, grain boundaries must be normalized by their geometric dimensions; otherwise, it is impossible to identify whether an increase in resistance is due to the relatively smaller grains of a sample – and therefore more total grain boundary length – or another more fundamental effect such as doping. In order to obtain quantitative comparisons, this work uses a well-established framework called the brick layer model (*4*, *109*).

The brick layer model treats a polycrystal as a set of cubes, with length equal to the grain size d_g, filling the bulk of a sample with length l and cross-sectional area A (see Figure 2.6). The conductivity of the grain boundary is then expressed as

$$\sigma_{gb} = \frac{\delta_{gb} n}{R_{gb} A} \tag{2.6}$$

where δ_{gb} is the thickness of the grain boundary and n is the number of grains between the electrodes. The capacitance of the bulk and grain boundaries are described by

$$C_{bulk} = \varepsilon_o \varepsilon_{bulk} \frac{A}{n d_g} \tag{2.7}$$

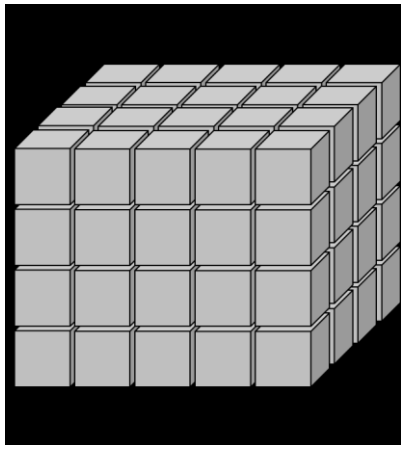

Figure 2.6 Geometry used in the brick layer model.

and

$$C_{gb} = \varepsilon_o \varepsilon_{gb} \frac{A}{n\delta_{gb}} \tag{2.8}$$

respectively. Assuming $\varepsilon_{gb} \sim \varepsilon_{bulk}$ (considered to be a reasonable assumption due to the relative insensitivity of ε_{YSZ} to dopant concentration (*110*)), the grain boundary thickness can be expressed as

$$\delta_{gb} \approx \frac{C_{bulk}}{C_{gb}} d_g \tag{2.9}$$

The number of transverse grains, n, can be expressed as

$$n = \frac{L}{d_g + \delta_{gb}} \tag{2.10}$$

and, if $\delta_{gb} << dg$, Equations 2.7-2.10 can be substituted into Equation 2.6 to give the final expression

$$\sigma_{gb} = \frac{L}{R_{gb}A} \frac{C_{bulk}}{C_{gb}} \tag{2.11}$$

This calculation also introduces δ_{gb} as a useful sample characteristic to consider. Note that, when calculating δ_{gb} from electrical measurements, the thickness refers to the effective electrical thickness, not the physical crystallographic thickness of the grain boundary, which may be substantially smaller.

2.4.4 Correction for lead inductance

During high temperature impedance measurements of zirconia ($T_{measure} \sim 1000^oC$), inductance from the system wires and cables can contribute substantially to the signal measured due to the relatively small impedance contribution of the zirconia itself. If substantial, this inductance can be problematic for any attempts at in-situ measurements i.e. measurements directly after flashing a sample at processing temperature. These effects can be eliminated from

the final signal by a simple procedure. First, the signal from the leads is measured by recording the spectrum of the system when shorted. The impedance of a pure inductor is

$$Z''_L = j*2\pi f*L \tag{2.12}$$

Thus, the inductance L of the system can be estimated by plotting $\frac{Z''_{short}}{2\pi f}$ vs. frequency; this plot should contain a plateau with the approximate value of L. With a reasonable value of L, the lead inductance can be calculated and subtracted from high temperature measurements using Eq. 2.12.

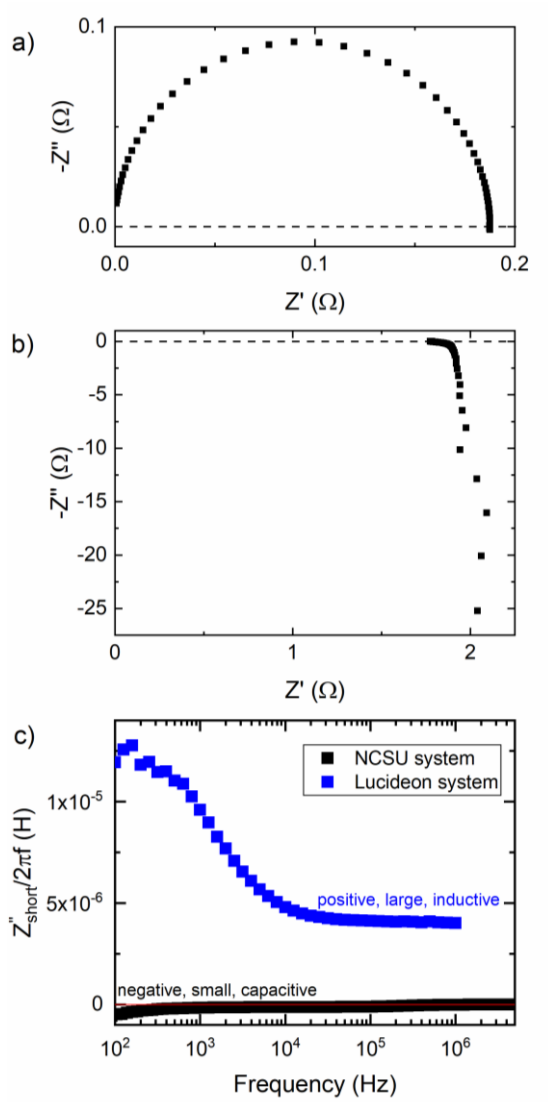

Figure 2.7 Short-circuit Nyquist plots measured from the flash sintering system (a) at NCSU and (b) at Lucideon. (c) shows the induction correction attempts using Z''_{short} for both systems.

The implementation of this process to the experiments in this work is shown in Figure 2.7. Figure 2.7a shows the short-circuit spectrum of the AC flash sintering system designed at NCSU (§2.2). In Chapter 6, additional flash sintering work was performed at the facility at Lucideon, Stoke-on-Trent; the short-circuit spectrum from that system is shown in Figure 2.7b. The inductance from the NCSU system was minor, barely manifesting as a small negative tail in the larger R||C loop. On the other hand, the inductance in the system at Lucideon was substantial, dominating the spectrum. The distinction between the two spectra was even more readily apparent in the inductance plot in Figure 2.7c, where the positive sign and high frequency plateau of the Lucideon system allowed for an estimate of $L \sim 4x10^{-8}$ H. On the other hand, the magnitude of the signal from the NCSU system was negligible and its negative sign indicates that no substantial inductance is present in the system. Therefore no correction was applied to high temperature impedance measurements taken in that experimental setup.

CHAPTER 3

Effect of Boundary Conditions on Reduction during Early Stage Flash Sintering of YSZ

As a processing technique, flash sintering was established using almost entirely DC fields. However, the possibility of stoichiometric changes under large fields was established outside of flash sintering literature well before the publication of the technique. Within the flash sintering community, the influence of chemical reduction/oxidation during processing has gone from a fringe effect to a factor frequently invoked to explain microstructural and electrical results. The work in this chapter contributed to the growing understanding of the detrimental effects that a DC field can have upon microstructural homogeneity, separating aspects of flash sintering which electrochemical interfacial reactions cause from the fundamental characteristics of field-assisted processing.

This chapter was originally published by Elsevier and is reproduced here with their permission, with slight modifications to incorporate it into the dissertation as a whole. The original reference can be found as:

Grimley, C.A., Prette, A.L.G, & Dickey, E.C., "Effect of boundary conditions on reduction during early stage flash sintering of YSZ." *Acta Materialia* 174 (2019): 271-278.

3.1 Abstract

The onset of flash sintering is generally considered to be predominantly a function of the conductivity of a given ceramic, the furnace temperature, and the electric field. However, the evolution of the point defect profiles in ionic conductors such as yttria-stabilized zirconia (YSZ) can complicate the picture of homogeneous Joule heating and thermal runaway during DC flash sintering. Here, 8 mol% YSZ pellets were partially flash sintered under a DC bias using various current densities and hold times. The electrode geometry was varied to modulate the oxygen ion flux available to the cathode to compare the effects on the resulting oxygen vacancy inhomogeneity. The contribution to the cathodic reduction reaction from fundamental and experimental factors such as interface reaction kinetics and sample geometry are also discussed. Local reduction of the ceramic was inevitably observed under all current densities and the resulting microstructural inhomogeneity was explained as the result of a transient conductivity asymmetry. This asymmetry was the result of the enhanced electronic conductivity in the cathode region to a value significantly greater than the ionic conductivity of near-stoichiometric YSZ. The link between the local conductivity, voltage and Joule heating is mathematically demonstrated to result in an asymmetric heating profile.

3.2 Introduction and background

Flash sintering emerged in 2010 as an interesting technique for rapid consolidation of ceramics out of work by Cologna et al. (*1*). The technique, which involved applying an electric field across a heated dog-bone-shaped ceramic powder compact, was characterized by a slow increase in sample temperature from Joule heating followed by a rapid onset of non-linear conduction and densification (*1*). In the years following its discovery, the application of the technique was demonstrated across a wide range of materials, and this universality has lent

insight into the nature of the onset of flash (*26, 27, 111*). Researchers such as Todd et al. (*63*), Zhang et al. (*33*), da Silva et al. (*62*), and Dong and Chen (*30*) separately demonstrated that the rapid conductivity increase during the first stage of flash can be explained largely by a thermal runaway effect in which a feedback loop between the Joule heating and the sample conductivity overcomes natural radiative cooling to produce an abrupt temperature increase. In theory, the effect was applicable to all materials with a negative temperature coefficient of resistivity.

Based on the universal nature of flash sintering combined with its apparent independence from conductivity mechanism, it has been tempting to ignore the effect that specific material properties may have on the flash sintering process or its final product. However, many open questions remain concerning the actual densification mechanism of flash and the various observed effects on grain size and distribution, e.g. cathode-localized rapid grain growth in yttria-stabilized zirconia (YSZ) compared to anode-localized grain growth in titania and zinc oxide (*31-33*). While the thermal runaway model provides an excellent foundation for the early stages of flash sintering, additional, material-specific conductivity and polarization mechanisms can and should be incorporated into the Joule heating model of thermal runaway in order to interpret these varying effects.

Recent work has built a more holistic picture of flash sintering by considering the electrochemical reduction reactions occurring simultaneously with the nonlinear conductivity increase and subsequent color front formation in materials such as YSZ, titania, and alumina (*32, 60, 79, 112, 113*). While the macroscopic evidence of reduction in YSZ, i.e. formation of color fronts ranging from brown to black, was reported during flash as early as Downs' thesis work (*43*), until recently literature has largely ignored the effect this reaction may have on the characteristic aspects of flash and the resulting microstructure. Recent investigations have

reported temperature gradients and asymmetric photoemission, suggesting a geometrically complicated picture of concurrent electrochemical reactions and Joule heating (*79, 82*). However, much of the work actively addressing these electrochemical effects focuses on pre-densified or fully densified samples, and, as such, the effects on densification initiation and its spatio-temporal evolution are limited. Furthermore, many studies typically rely on dog-bone shaped samples, which maximize the ability of the sample to equilibrate with the external atmosphere (*114*).

To this end, the present investigation links inhomogeneous microstructural development in partially flash-sintered 8YSZ pellets to the fundamental electrochemical processes in YSZ, which are well established in the literature. Under high current densities, inadequate oxygen flux at the cathode creates a locally reduced region which progresses through the length of the sample at the expense of the stoichiometric YSZ. This process establishes a transient conductivity asymmetry across the ceramic with attendant thermal and microstructural inhomogeneities. These inhomogeneities are highly dependent on the sample boundary conditions, which, in practice, are determined by the limiting current density and the relationship between sample and electrode geometry, all of which need to be taking into account in practical applications of flash sintering.

3.3 Methods

8 mol% YSZ powder with polyvinyl alcohol binder (Inframat Advanced Materials) was uniaxially pressed with 336 MPa into pellets 6.1 mm in diameter and approximately 3 mm thick. The binder was burned out before sintering by heating the pellet in a furnace at 600°C for 1 hr. The green density of the pellets after binder burnout was 52 ± 0.5% of the theoretical density.

Isothermal flash sintering runs were performed using a modified horizontal dilatometer setup. Either solid Pt or Pt-mesh electrodes were inserted into the sample holder and connected to the external DC power supply (Sorenson DCS 300-3.5) by Pt wires. A push rod applied ~0.05 MPa of pressure to ensure good electrical contact between the electrodes and the pellet. In addition, the ends of each sample were coated with a conductive paste of either Ag (Sigma Aldrich) or Pt (Gwent Group) to improve contact. Three combinations of electrode configuration were used: Ag paste with solid Pt electrode; Pt paste with solid Pt electrode; and Pt paste with Pt mesh electrode (see Figure 3.1).

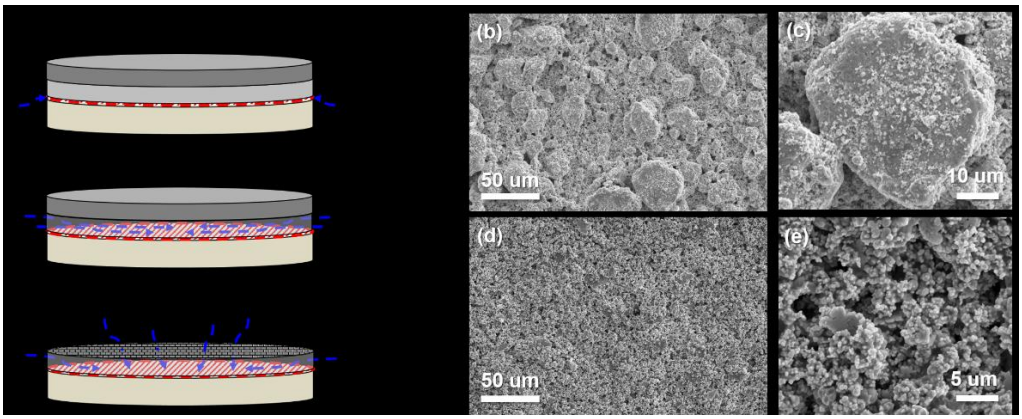

Figure 3.1 (a) The three electrode/paste combinations tested and SEM images of the microstructure of the (b) Ag and (c) Pt paste applied directly to the pellets. In (a), the red area indicates the TPB while the blue lines depict O_2 diffusion paths.

The experiments were conducted by loading the sample into the sample holder and inserting it into the pre-heated furnace, where it was allowed to thermally equilibrate for 20 minutes. An isothermal furnace temperature of 900°C was used for all runs. After thermal equilibration, a field of 260 V/cm was applied as a single step function; the voltage was preset and the supply turned on, maximizing the ramp rate of the power supply. Current limits ranging from 1 A (3.4 A/cm^2) to 3.5 A (11.9 A/cm^2) were set using the power supply controls, and a LabVIEW program monitored the current and shut off the supply after a set period of time; in

this study, hold times of 0.5, 10, or 20 minutes were used. Secondary electron images of fractured cross-sections were taken using a JEOL 6010LA scanning electron microscopy (SEM).

3.4 Results

3.4.1 Electrode characterization

The electrode configurations, summarized in Figure 3.1, progressed from partially blocking to geometrically open as the pastes and geometry changed. The Ag and Pt pastes provided different characteristics in terms of microstructure, catalytic activity and mechanical behavior. The microstructure of the two pastes after spreading on a pellet surface and drying are shown in Figure 3.1b-e. Although Ag has been shown to facilitate faster transfer kinetics of oxygen into ZrO_2 as compared to Pt (*115*), the Ag paste in the present study was much denser and more agglomerated than the Pt. Because of the denser starting structure and the use of a furnace temperature close to the melting point of Ag, the Ag paste-solid Pt electrode was anticipated to form the most severe geometrically blocking condition for oxygen transfer across the interface due to the lower triple phase boundary (TPB) length between the atmosphere, metal and YSZ. The Pt paste with solid electrode then functioned as an intermediate case, where the paste retained much of its open porosity, increasing the TPB length along the surface and allowing for some lateral permeation of oxygen through the paste layer. The Pt paste with the mesh electrode formed the closest approximation of an open boundary condition, allowing for permeation through the electrode itself (as illustrated in Figure 3.1). Note that a paste layer was required not only for stable electrical contact, but also for repeated application of the same electrodes, particularly in the mesh case. Intensive heat generation on the anode, discussed later, melted the fine wires of the mesh electrode without a conductive layer to dissipate the heat.

3.4.2 YSZ Blackening

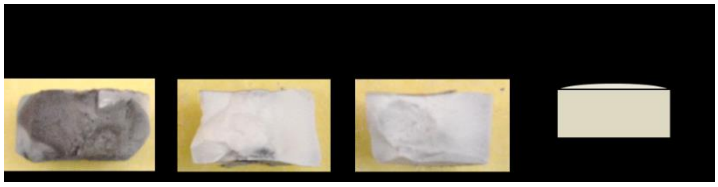

Figure 3.2 Optical images comparing severity of blackening for Ag paste-solid Pt, Pt paste-solid Pt, and Pt paste-mesh Pt samples. Samples were each processed with 5.3 A/cm^2 for 0.5 minutes.

Figure 3.2 shows optical images of samples flash sintered for 0.5 minutes at 5.3 A/cm^2 for each electrode condition. Severe degrees of blackening are observed under these relatively low current densities in the samples processed with the Ag-paste/solid-Pt electrodes. While some coloration may have been due to migration of Ag into the ceramic, EDS analysis only detected Ag within ~150 m of one electrode, which contrasts with the significant and fully infiltrated color change in Figure 3.2a. The sample with the Pt-paste/solid-Pt electrode configuration exhibited some degree of blackening in the near-cathode region, particularly near the radial center of the pellet. In both types of samples with the solid-Pt electrode, the maximum applicable current density was limited by the melting of the platinum anode during the flash event; the electrodes from the Ag-paste/solid-Pt samples melted when flash sintered with 8.8 A/cm^2, while the electrodes for the Pt-paste/solid-Pt melted around 10.6 A/cm^2. The Pt-paste/Pt-mesh samples, however, showed no blackening when flash sintered with 5.3 A/cm^2, as seen in Figure 3.2, and generally withstood the upper limit of the power supply (3.5 A or equivalent 12.4 A/cm^2 for our sample geometry) without electrode melting. These results implied a direct relationship between the degree of reversibility at the electrode and the extent of blackening during the initial 30 seconds of flash. Furthermore, the physical robustness of the samples scaled with coloration, ranging from the darkest Ag-paste samples, which crumbled upon removal from the dilatometer, to the mesh samples, which retained their structure during handling.

Figure 3.3 shows the effect of current density on the blackening profile in the Pt-paste/mesh samples as a function of current density and hold time. The onset of blackening appeared at 7.1 A/cm^2, and blackening was localized to the cathode for all samples processed for 0.5 minutes. Figure 3.3 also shows a time series of the Pt-paste/mesh flashed at 10.6 A/cm^2 with hold times of 0.5, 10, and 20 minutes. When held for longer times, the color front completely permeated the pellets, providing some information on the velocity of the color front during the flash process. Note that the blackened region did not extend all the way to the electrodes. We believe that this results from some oxygen incorporation into the sample as it is cooled to room temperature without a biasing voltage (at an estimated rate of 40˚C/min).

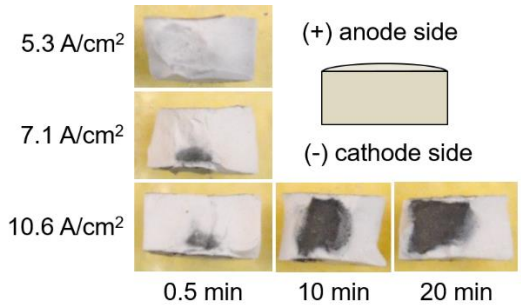

Figure 3.3 Optical images comparing severity of blackening for Pt mesh/Pt paste electrode samples processed with 5.3, 8.8, and 10.6 A/cm^2 for 0.5 minutes, and 10.6 A/cm^2 for 10 and 20 minutes.

3.4.3 Densification and microstructure

Samples partially flash sintered at a furnace temperature of 900 ˚C and over a range of conditions exhibited final densities ranging from 59.9 to 81.9% theoretical density depending on the electrode configuration, current density, and the hold time. As seen in Figure 3.4 and Figure 3.5, the samples generally exhibited partially sintered microstructures. This degree of porosity corresponded to the intermediate stage of sintering, in which necks have formed between particles, but the porosity is largely open (*3*). These partially sintered microstructures provide useful insight into the heat/current distribution throughout the sample at the initial stages of flash sintering.

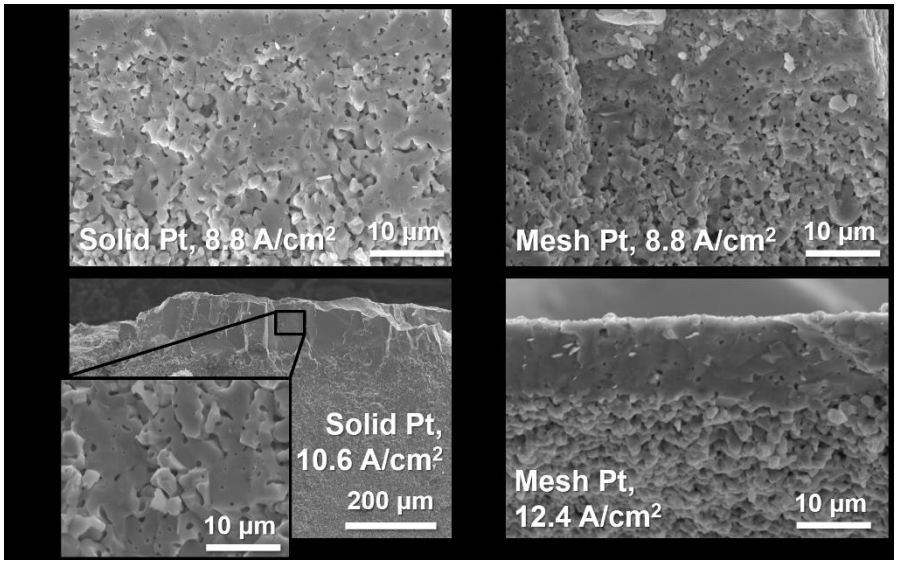

Figure 3.4 SEM images of the anode region (fracture surfaces) for samples processed for 0.5 min with Pt paste and (a) solid Pt electrode and 8.8 A/cm^2, (b) mesh Pt electrode and 8.8 A/cm^2, (c) solid Pt electrode and 10.6 A/cm^2 and (d) mesh electrode and 12.4 A/cm^2.

Inhomogeneity during early-stage flash sintering manifests in a couple of different ways. Macroscopically, the pellets did not densify evenly, resulting in a large variation in the estimated densities. Densification was concentrated along the anode in many samples, as illustrated in Figure 3.4. Dense regions of YSZ adjacent to the anode were evident in all electrode types, and the thickness of the dense layer scaled with oxygen permeability through the electrode; this correlation is demonstrated by comparing the solid Pt (Figure 3.4c) to the mesh Pt electrodes (Figure 3.4d) processed at the maximum possible current densities for both configurations. These areas of localized densification exhibited closed porosity, with significantly greater density than the remainder of the pellet, which retained open porosity. This distinction corresponds to a transition into the final stage of sintering characterized by pore shrinkage. In addition, these regions more commonly exhibited transgranular fracture as compared to the bulk of the ceramic body. In contrast, in all samples the cathode side retained an almost green microstructure (Figure 3.5).

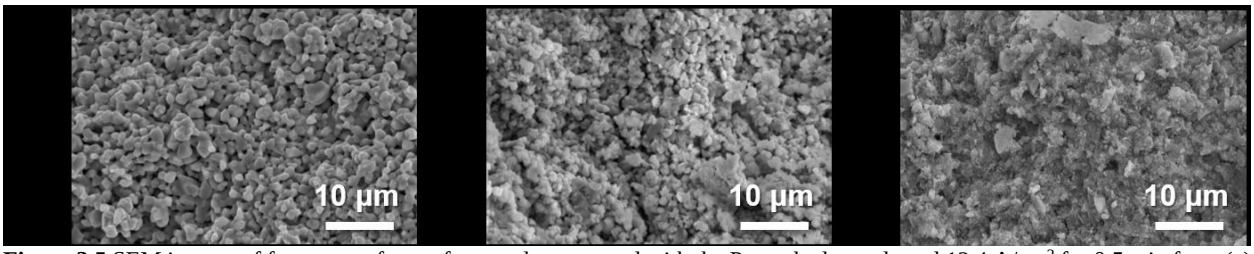

Figure 3.5 SEM images of fracture surfaces of a sample processed with the Pt mesh electrode and 12.4 A/cm^2 for 0.5 min from (a) the sample center and (b) the cathode; (c) shows the green microstructure for comparison.

3.5 Discussion

The color-front and microstructural observations on partially flash sintered samples indicate a link between the oxygen exchange at the electrodes during the flash sintering of YSZ and microstructural inhomogeneity. This connection can be understood by the electrochemical reduction that the limited reversibility of the electrode promotes which localizes the voltage drop and therefore heat generation to the anodic region, as will be discussed in detail below.

3.5.1 Conditions influencing steady-state ionic conduction

Across a wide range of temperatures and atmospheric pressures, YSZ functions as an almost purely ionic conductor in which the cathode undergoes the following electrochemical reaction driven by the applied current:

$$V_o^{\cdot\cdot} + O_{ads} + 2e' \rightarrow O_o^x \tag{3.1}$$

where the standard Kröger-Vink notation is used. The anode undergoes the reverse reaction:

$$O_o^x \rightarrow V_o^{\cdot\cdot} + O_{ads} + 2e' \tag{3.2}$$

and oxygen vacancies are transported from the anode to the cathode in response to the applied voltage (*116*). Reaction (3.1) is known to occur at or in the vicinity of the triple phase boundary (TPB) between a metallic electrode (functioning as an ion-blocking electron source), atmospheric oxygen (functioning as an electron-blocking oxygen source), and the YSZ electrolyte (*117*). This area is referred to as the electrochemically active region, and appears to be on the order of 1 um (*118*). Generally, it is considered that the oxygen is first adsorbed onto

the metallic electrode then transported along the electrode surface to the TPB, where Reaction (3.1) is catalyzed. In a steady-state condition, the flux at the cathode in terms of electrons and oxygen equals the flux of each species in the opposite direction at the anode; in this case the electrolyte is not polarized, meaning no stoichiometry gradients are induced (*119*). The oxygen activity on the cathode is directly proportional to the applied voltage via the Nernst equation. Therefore, for these steady-state conditions to be achieved, adequate fluxes of O_{ads} and $V_{\ddot{o}}$ at the TPB must be achieved and the surface exchange kinetics must not limit the process.

Whether an adequate concentration of reactants is present depends on the current density and whether the oxygen adsorption, surface diffusion, and reaction rates are fast enough to maintain steady state concentrations. Identification of the rate-limiting step as electrode (O_{ads} and diffusion) based or reaction (charge transfer and defect diffusion) based is difficult, and evidence exists to support either interpretation (*117*). In either case, this investigation is concerned with the established scaling of the kinetics with the following geometric factors: (1) the length of the TPB as the active reduction site and (2) the area of the metal/O_2 interface as the site of O introduction to the system.

As such, the geometry of the electrode configurations shown in Figure 3.1a exert significant control over whether the steady-state conditions set by the current density are met. This concept was touched on in the previously referenced work from Biesuz et al. in which the deviation from ionic conduction in dense YSZ was modulated by “bad” and “good” contacts i.e. contacts attached with and without conductive Pt paste (*79*). The inclusion of Pt paste increases the length of the one-dimensional transfer interface, thus increasing the number of active reaction sites. In this investigation, this length was modulated by pastes with different morphologies, with the more porous layer creating more contact.

However, more fundamental limitations are enforced at the TPB as well. Even in the presence of excess O_{ads} and a high concentration of reaction sites, the surface reaction rate is finite, as controlled by charge transfer and defect diffusion. The charge transfer resistance describes the energy barrier to electron transfer from the electrode to the electrolyte. Within the electrolyte, the necessary defects ($V_O^{\cdot\cdot}$) require time to diffuse to the TPB; this diffusion is enhanced by the electric field, as described by the Nernst-Einstein equation, but is still finite (*117*). Taken in combination with the geometric variation of the TPB, these factors imply a limiting ionic current density based both on the experimental choice of TPB formation as well as fundamental reaction kinetics, one of which will function as the rate-limiting step in Reaction 3.1.

Away from the TPB, the incorporation of atmospheric oxygen is similarly limited by both sample geometry and mechanism kinetics. The concentration of O_{ads} is fundamentally based on the adsorption kinetics as described by the sticking coefficient, but the amount available to the overall system is controlled by the amount of contact area between the air and the metal and is therefore maximized by a three-dimensional porous metallic layer with significant surface area. Unlike the reaction kinetics, however, the adsorption and subsequent surface diffusion of oxygen is driven primarily by the O_{ads} chemical gradient between the TPB and the rest of the O_2/metal interface, and therefore remains relatively independent of the electrical potential (*117*). It should be noted that, during flash, the electrode temperature increases along with the rest of the sample, and some enhancement to surface diffusion is expected in response. However, the increase in surface diffusion would be at least partially offset by a decrease in the sticking coefficient with increasing surface temperature (*120, 121*).

In the interest of thoroughly considering all paths for oxygen diffusion into YSZ, we also consider the direct diffusion of atmospheric oxygen via the YSZ porous surface as an additional path. Using measurements from Manning et al. for the surface exchange coefficient between oxygen and single crystal 9.5YSZ (*122*) as an estimate for the uncatalyzed incorporation of oxygen into the 8YSZ polycrystal, it is possible to compare the maximum rate of oxygen intake via adsorption and diffusion at the YSZ/O_2 interface to the oxygen flux required by the applied current. The required oxygen incorporation rate during flash is set by the cross-sectional current

$$n_{O,\,out} = \frac{i}{2eN_A} \tag{3.3}$$

whereas the maximum oxygen incorporation rate into the sample via atmospheric adsorption and diffusion is

$$n_{O,\,in} = \frac{k^*}{2}\frac{P_{O_2}}{RT}A_s \tag{3.4}$$

where the constants e, N_A, and R are the elemental charge, Avogadro's number, and the gas constant, while A_s is conservatively considered as the entire exposed YSZ surface area as calculated by the hard sphere model (*123*) and based on the measured initial density of 52%. The surface exchange coefficient k* is estimated to be 4 x 10^{-7} cm/s at 900°C (*122*). Under the conditions of this experiment and the lowest current applied (1 A), the rate of oxygen incorporation required at the cathode to maintain steady-state ionic conduction via Reaction 1 is 5.18 x 10^{-6} mol/s, while the oxygen incorporation into the sample via atmospheric diffusion is calculated to be 2.91 x 10^{-12} mol/s via Eq. 3.4.

A robust examination of this contribution should also consider that, during flash sintering, the sample temperature is expected to significantly exceed the furnace temperature, which would increase the value of k* and thus the contribution of atmospheric oxygen. The original measurement of k* extended up to 1100°C (*122*), at which temperature the incorporation

rate increases by approximately an order of magnitude to 5.83 x 10^{-11} mol/s; yet the molar flux remains five orders of magnitude smaller than the amount required by the current flow. Furthermore, fitting an Arrhenius expression to the data from Manning et al. (*122*) and extrapolating, the sample temperature required for the atmosphere to contribute as much as ten percent of the required oxygen flow would require a surface temperature of 2318°C, well above what has been measured or calculated in similar experiments (*77, 86*) and approaching the melting point of ZrO_2. Thus we conclude that the un-catalyzed incorporation of atmospheric oxygen contributes negligibly to the oxygen flux into the sample.

The tremendous gap between the oxygen flux requirement and the diffusional contribution raises an interesting question: given the large number of factors affecting the kinetics of Reaction 1, what magnitude of ionic current density can the YSZ system reasonably maintain in steady-state? The solid oxide fuel cell community has been grappling with quantitative models of this system's kinetics for decades, in part to define the upper limits to cell operation. To provide an estimate, an excellent example can be found in the work of Mitterdorfer and Gauckler, which combines the previously described kinetic limitations to estimate the rate coefficient of the electrochemical reaction and links the reaction coefficient to the ionic current (*124, 125*). Assuming a one electron kinetic step, they derive a maximum current of $i = 2FA\ V_o^{\cdot\cdot}\ \theta^o k_o \exp(-E_a/RT)$ in which A is the chemically active area, Γ is the number of surface sites on the Pt, θ^o is the coverage of O_{ads} at the reference temperature, and $k_o\exp(-E_a/RT)$ is the Arrhenius expression for the electrochemical reaction coefficient at the cathode. Using the kinetic values estimated in their study as well as their area values for porous Pt, assuming a constant atmospheric PO_2 of 0.21 atm, and correcting for the initial sample temperature of 900°C, electrode area, and initial vacancy concentration, this model predicts a maximum ionic

current of approximately 0.07 A/cm^2. At a higher temperature of 1200°C, as may be reached during flash sintering due to Joule heating, this value increases to 0.18 A/cm^2. While these values are not negligible and function as only estimates, they still only represent at most 5 percent of the lowest current density utilized in this study.

3.5.2 Electrochemical reduction in YSZ and its implications

It is clear, intuitively and semi-quantitatively, that during the flash sintering of a predominantly ionic conductor, steady-state ionic conduction cannot be achieved under high current densities. Experimental parameters such as electrode geometry can further restrict the maximum achievable ionic current density. This behavior, and its implications for oxygen ion flux restrictions at one or both electrodes, is functionally identical to a partial "blocking electrode" described in other electrochemical models and observed experimentally in many other ceramic systems (*126-128*). These models confirm that, in the ion-flux-limited regime, polarization invariably occurs, resulting in either reduction or oxidation.

In YSZ, this polarization produces local changes in $\mu_{O^{2-}}$ which push the defect chemistry into a mixed conducting regime (*129*). The suggestion that YSZ transitions from a purely ionic conductor to a predominantly electronic conductor during flash sintering is not novel (*79*), but its discussion remains relevant for two reasons. First, the modeling work around flash sintering assumes a conductivity mechanism modelled by a single Arrhenius equation, which will clearly not be the case for many experimental conditions. A more accurate description of the DC conduction in YSZ and similar oxides may lead to more comprehensive models. Second, the reduction reaction that occurs in YSZ when the steady-state conditions are not met and which leads to macroscopic stoichiometry polarization lends insight into the asymmetric field and temperature distribution during flash sintering in ways that have not been considered.

During the polarization process, the excess vacancies, along with electrons injected from the electrode initiate a reduction reaction at the cathode which progresses into the sample if the field is sufficiently high. The reduction mechanisms and the defects that function as the color centers have been heavily discussed, with evidence found for defects ranging from electron-neutralized vacancies (F centers) to electron trapping via impurity sites or Zr^{3+} formation, an oxidation state known to be field-stabilized (*130-133*).

Even without exact knowledge of the defect chemistry, the properties of this reduced region are empirically understood and the behavior modelled. The cubic phase is retained, although some microstructure changes at the grain boundaries have been noted (*134*). Conduction in the material becomes increasingly mixed with electron conduction eventually dominating (*81*) and the increase in conductivity is linked to the degree of sub-stoichiometry (*81, 135*). The spatial extent of the reduced region has been modelled, with the steady-state position of the reduction front depending on applied voltage (*114*). Furthermore, due to the mixed conductivity of the reduced volume, this region functions as an additional electrochemically active area capable of providing both electrons and vacancies to the YSZ/O_2 interface and facilitating Reaction 1 (*114, 136*).

The last characteristic is of particular interest because it assigns relevance to the geometric differences between experimental setups in the literature. As a sample is progressively reduced to the mixed conducting state during flash sintering, the electrochemically active surface area increases, marked by the reduction front position, w, in Figure 3.6; for a given w, this area can be calculated. Normalizing the electrochemically area (A_{active}) by the sample volume, which is proportional to the amount of oxygen required to retain stoichiometry, introduces a parameter that controls the degree of electrochemical reduction for a given sample geometry. Comparing

this geometric parameter for different experimental setups provides an explanation for the varying transience and degrees of blackening observed during flash sintering of YSZ in other studies.

To illustrate, the results from this study are compared to the analogous study on dense YSZ from Biesuz et al. (*79*). In the Biesuz study (and much of the foundational work in flash sintering), long samples were used with wrapped Pt electrodes; this geometry offers a high active surface area relative to its volume, whereas the present investigation used pellets with cross-sectional electrodes which offer relatively less surface area. As a result, in the Biesuz study the color front was often transient, appearing during flash and disappearing afterwards (*79*). In contrast, the blackening in this study was retained, although the coloration was often limited to the radial center of the sample. As shown in Figure 3.6, the geometric factor (A_{active}/V) describing the Biesuz sample was consistently larger than in this work, allowing for greater oxygen retention and incorporation. Conversely, the active surface area of the pellets in this investigation was significantly less compared to the pellet volume. In addition, the diffusion path to the sample center was larger than that in the Biesuz study, which may also contribute to the localization and retention of the sub-stoichiometric region in the sample center. The importance

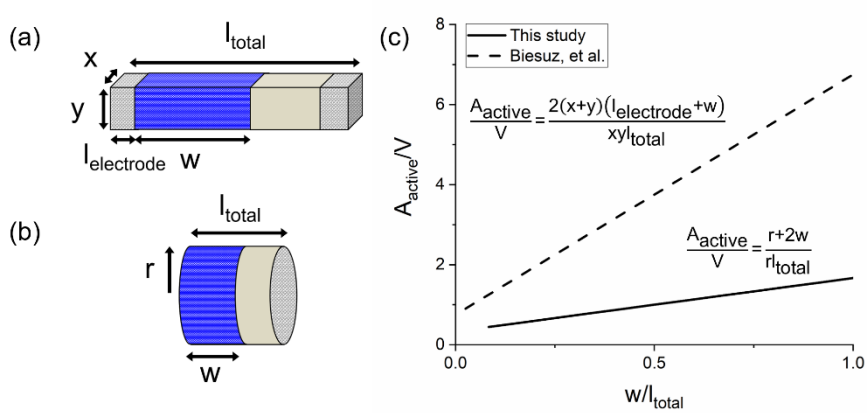

Figure 3.6 Schematic of (a) bar and wrapped Pt geometry and (b) cylinder and end electrode geometry where blue represents the segment of the sample that is reduced. (c) Comparison of the area of electrochemically active region normalized by the sample volume for the two geometries.

of this comparison lies primarily in the scale-up and application of flash sintering; the geometry of commercial ceramic components is dictated by end use rather than ideal study conditions and has implications for secondary variables like temperature and field.

The link between inadequate oxygen exchange at the electrodes, stoichiometry polarization, and microstructure lies in the properties of the reduced region and the transient state during which it propagates through the sample. The implications of this transient electrochemical reduction can be explored using a simple one-dimensional model that considers the sample to be a set of resistors in series. As the reduction front initiates at the cathode and travels through the sample, it divides the sample into two regions, one a reduced, highly conductive mixed region and one a stoichiometric, resistive region which remains predominantly ionically conducting. In the reduced region, electrons travel from the cathode to the color-front interface, where they are trapped by either oxygen vacancies or impurity ions, advancing the boundary. Oxygen vacancies transported through the stoichiometric region either recombine with electrons to form immobile F centers at the interface of the two regions or are transported through the mixed conducting region. In practice, the reduced zone would contain a distribution of stoichiometries and therefore conductivities, but for this simple model homogenous reduction will be assumed.

As the reduced region grows, the voltage profile across the sample will mimic the conductivity distribution, disproportionately dissipating power in the more resistive stoichiometric region. The balance between the heat generated during this transient phase and the radiative cooling of the sample, can be calculated by

$$Q = V_{i,j}^2 \frac{\sigma_{i,j} A}{l} - A\varepsilon S \quad T_{i,j}^4 - T_f^4 \tag{3.5}$$

in which subscripts i and j indicate position and time, A and l are cross-sectional area and length, ε and S are emissivity and the Stefan-Boltzmann constant respectively, and T_f is the furnace

temperature. The expression for conductivity at a given point in space and time is an Arrhenius expression

$$\sigma_{i,j}\ T = \sigma_o \exp\ -\frac{E_a}{kT} \tag{3.6}$$

The expression of $\sigma_{i,j}$ should vary depending on whether the point is contained within the reduced region of the sample. Broadly accepted expressions for ionic and electronic conductivities can be found in the work of Park and Blumenthal (*116*), the electronic conductivity corresponding to the reduced-region conductivity in this model.

Following these expressions, the electronic conductivity also requires an estimate of local effective PO_2, which in turn depends on the degree of polarization achieved in the sample. For the case of this simple model, an effective PO_2 of 1.1 x 10^{-35} atm was used. The choice of a constant PO_2 is conservative; the value should continue to decrease as the sample becomes increasingly polarized. The specific value chosen corresponds to an electronic transport number of 0.7 at 900°C, an achievable value measured in the work of Masó and West (*81*).

Treating each slice of the sample as a resistor described by either σ_i or σ_e, and assuming the excess energy in Equation 5 heats its slice, the final expression for local sample temperature is the equation

$$\frac{C_p m}{\Delta t} T_{i,j} + AS\varepsilon T_{i,j}^4 = V_{i,j}^2 \frac{\sigma_{i,j} A}{l} + \frac{C_p m}{\Delta t} T_{i,j-1} + AS\varepsilon T_f^4 \tag{3.7}$$

in which C_p is specific heat and m is the mass of the slice. As the front moves, the overall series resistance decreases, the current limit of the power supply is quickly reached, and the total voltage applied decreases as the supply switches into current-control mode. This is observed experimentally in Stages I and II of flash sintering and in the model, which is designed to reflect the switching time response of the power supply model used for this work (~500 μs). All

constants used in this equation are given in Table 3.1. The last parameter of interest is the speed at which the reduction front travels. A constant rate is assumed for this treatment, as would correspond to a first-order reaction. The characteristic time to reach steady state can be estimated based on Kirchheim's recent work (*114*), assuming irreversible electrodes and setting the steady state position of the reduction front to be the length of the sample, as appears to be the case in this investigation (see Figure 3.3).

Table 3.1 Parameters used to estimate temperature/voltage distributions.

Parameter	Value
A (cm^2)	0.2827
l (cm)	0.003
m (g)	0.000254
C_p (J/g*K)	0.64
ε	0.7
$\sigma_{o,i}$ (S/cm)	1.63x102
$E_{a,\,i}$ (eV)	0.79
$\sigma_{o,e}$ (S/cm)	1.31x10^
$E_{a,e}$ (eV)	3.88
T_f (K)	1173

Figure 3.7 demonstrates the link between local conductivity, distribution of the voltage drop, and the effect on temperature with time as the reduction front progresses through the sample. Note that the absolute values of the temperature are underestimated; the one-dimensional nature of the model ignores the insulating character of the outer YSZ region, which is significant (*63*). It is clear, however, that the cathode, which is reduced first, remains notably cooler than the rest of the sample. The center of the sample follows the higher heating rate of the anode until the reduction front overtakes it. The heat generation is therefore overall concentrated on the anode during the reduction process.

These profiles qualitatively agree with the microstructural inhomogeneities observed; the cathodic microstructure was effectively green, the sample center partially sintered, and the

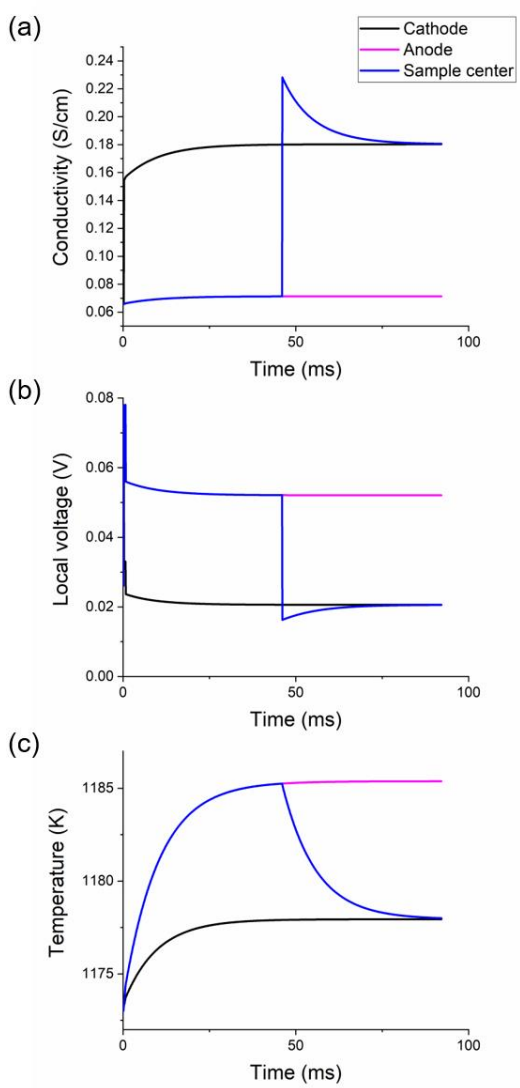

Figure 3.7 Model results showing (a) the conductivity, (b) local voltage drop, and (c) temperature for the anode, cathode, and sample center as a function of time.

anodic region densified substantially more. It is interesting to note that the early work from Casselton on blackening in YSZ also empirically confirmed the voltage asymmetry by placing probes along the length of YSZ and measuring voltage locally under electrochemically reducing conditions (*45*). He found that uneven voltage distributions were stable under combinations of high current densities and reducing furnace atmospheres; at higher current densities, the atmospheric PO_2 capable of inducing the asymmetry increased (reaching as high as 0.02 atm). At intermediate current density/PO_2 combinations, the reduced region remained localized to the

cathode, concentrating the voltage drop across the rest of the sample. This field asymmetry is also represented in flash sintering literature by the localized retardation of grain growth in the anodic region reported in fully dense samples (*37, 99*), as applied field strength has been linked to grain growth suppression in YSZ (*16*).

Once the temperature dependence of the voltage distribution is established in a simple one-dimensional model, a three-dimensional extension can be qualitatively considered based on the morphological instability of the reduction front as reported by Janek and Korte (*137*) and thermodynamically motivated by work from Schmalzried (*138*). The stability of the two-phase interface is determined by the direction of the reduction-controlling flux relative to the direction of the boundary motion and the mobilities of the components in each phase. In the case of the reduction of YSZ, Janek and Korte concluded that the instability of the front suggested the reduction was controlled by the oxygen vacancy flux, and that the electronic mobility in the reduced zirconia was greater than that of the oxygen ions in stoichiometric YSZ. Since their work, Masó and West have confirmed this prediction in the measurement of the electronic transport number under a DC bias i.e. reducing conditions (*81*). Because the oxygen vacancies travel towards the advancing phase boundary, and electrons are considered to be in excess due to their higher conductivity, perturbations in the travelling front are exacerbated rather than stabilized.

During the sintering of porous YSZ then, several factors may introduce an additional radial component to the inhomogeneous densification. The morphologically unstable reduction front represents an irregular voltage concentration whose impact should mimic that of the one-dimensional model except for its orientation perpendicular to the velocity of the front. In addition, radiative cooling from the sample surface would consistently concentrate current and

therefore heat generation in the sample center. This concentration would be further exacerbated by the incorporation of oxygen from the free surface of the sample, a mechanism which decreases the degree of non-stoichiometry in the outer regions, thereby concentrating the current density in the more conductive sample center.

3.6 Conclusions

The oxygen stoichiometry gradient in YSZ during flash sintering is significantly affected by a number of experimental factors, including current density magnitude, triple-phase boundary length, electrode permeability, and sample geometry. The stoichiometry polarization is fundamentally determined by the surface exchange kinetics, which depend on the charge transfer resistance and the availability of adsorbed oxygen. Partially blocking electrodes and geometric factors that limit the exposed sample area exacerbate the tendency of the YSZ to reduce and blacken. The reduction of YSZ during the first stage of flash sintering produces uneven microstructural evolution, as evidenced by highly inhomogeneous densification from the anode to cathode during early stage sintering. The densification inhomogeneity can be explained by the transient reduction process, which concentrates the voltage drop and heat generation in the anode region. A radial component of inhomogeneity is also introduced by some combination of the morphologically unstable reduction front, radiative cooling, and the incorporation of oxygen at the free surface of the sample. These effects and their relationship to the sample geometry have significant implications for the scale-up and application of flash sintering.

3.7 Acknowledgements and permissions

This work was funded by Lucideon, Ltd., Stoke-on-Trent, UK. It is reproduced here with permission from Elsevier.

CHAPTER 4

A Thermal Perspective on Flash Sintering: The Effect of Current Ramp Rate and Its Processing Implications

4.1 Introduction and background

Flash sintering is a novel sintering technique which utilizes high electric fields and relatively low furnace temperatures to produce rapid densification. It is characterized by a nonlinear increase in conductivity concurrent with abrupt densification (*26, 111*). The wide range of ceramics sintered in this fashion often exhibit properties such as retained small grain size (*1, 139*), increased conductivity (*36, 38*), and unusual luminescence (*140, 141*). It remains unclear whether these properties are unique to the flash process, or the product of some combination of electric field effects and the short densification time. A unified understanding is further confounded by conflicting evidence between studies and materials e.g. polarity dependent enhanced grain growth in certain systems (*98*).

As the number of studies investigating the fundamental mechanisms of flash sintering grows, the discussion revolves around three main theories: enhanced formation of Frenkel defects leading to an avalanche of mass and electrical transport (*49, 74, 142*); liquid formation at grain boundaries which produces capillary force-driven densification (*56*); and thermal runaway with rapid-rate sintering (*30, 61-63*). (Electrochemical effects are sometimes included among

these as a separate densification mechanism; while these effects certainly influence the sintering process, we consider them to be secondary to densification. Electrochemical oxidation/reduction can couple with any one of the above mechanisms.)

Each of these theories has some experimental support, but often this evidence could be produced by the electric field or by the temperatures reached via Joule heating, e.g. the excess of anionic defects after flash. In fact, one of the challenges in fundamental flash sintering studies is the separation of thermal and electrical effects. Cao et al. recently suggested that the process of flash, rather than representing one exclusively field-driven or one exclusively thermally-driven mechanism, is likely a confluence of several mechanisms responding to multiple stimuli of which electric field and current are simply two more (*143*). In this spirit, we present a study which uses current ramp rate control to distinguish the effects of the thermal profile of flash sintering as compared to conventional sintering. The rate of increase in current directly controls the heating rate of the sample, which accommodates a controlled transition of the heating rate during flash sintering into that of field-assisted sintering and finally that of a conventional sintering profile.

To our knowledge, at this time a handful of studies have introduced or utilized current ramp control in the flash sintering process; while we will consider our results in the context of these works, this study occupies a unique space among them as the only study to combine AC with current ramp rate control across a timescale spanning from the fastest possible flash sintering process up to conventional sintering. The first two studies were published in 2018 by Charalambous et al. (*144*) and Kumar et al. (*145*) on current controlled DC flash sintering of ZnO and 3 mol% yttria-stabilized zirconia (YSZ) respectively. An additional study on current ramp rate controlled DC flash sintering of ZnO was published the following year by Phuah et al.,

using TEM to examine microstructures in more detail (*146*). The use of DC fields in these studies complicates the fundamental interpretation of the results. The significance of the electrochemical effects which DC introduces to the processing of oxides such as YSZ (*31, 78, 79*), ZnO (*33*), and alumina (*60*) are well established. This was manifest in the Charalambous study as a difference in grain size between the positive and negative electrodes, and as a difference in porosity between electrodes in the Phuah study. In addition to grain size trends, the chemical and defect distribution inhomogeneity which DC introduces complicates the analysis of electrical results. Only two papers to our knowledge have addressed current ramp in AC flash sintering, using 3YSZ; however, the first study looked at different functional forms of the current ramp rather than rate control (*41*), and the second used such a limited range of current ramp rate values that it is difficult to compare our results (*147*).

In this study, a state-of-the-art current control system was used to elucidate the processing-property relationships during AC flash sintering- that is, flash sintering in which additional electrochemical effects and inhomogeneities have been minimized. Surface temperature was tracked with an IR camera and the internal temperature estimated using finite element modelling (FEM) so that final properties could be related back to absolute temperatures and heating rates. The results of the study demonstrate that when normalized by the samples thermal history, the microstructural development is the same between field- and non-field based processing techniques. With the possible exception of grain boundary behavior, no properties are observed which cannot be explained by the unusual thermal profile of flash sintering and the resulting microstructures.

4.2 Methods

4.2.1 Sample preparation

8 mol% YSZ powder (Tosoh, TZ-8Y) was ball milled with 1 wt % binder (poly-vinyl butyral) in methanol for 24 to 48 hours with zirconia milling media. Pellets were prepared by pressing the powder in a 6 mm diameter die uniaxially with 87 MPa, then isostatically with 276 MPa. The binder was burned out in advance of further processing by holding the pellets at 600°C for 1 hour. Final green body densities were 51.2 ± 0.8% theoretical density and final thicknesses were 3.29 ± 0.06 mm. The faces of the green pellets were coated with platinum paste (70% Pt, Gwent Electronic Materials) and the organics were dried out of the paste by baking on a hot plate for 1-3 minutes.

Control samples were prepared via conventional thermal processing by the following heat treatment: ramp to 600°C at 300°C/h, heating to 1400°C at 80°C/h, soaking for 2 hours, heating to 1500°C at 50°C/h, holding at 1500°C for 4 hours, cooling at 20°C/h to 1000°C, then uncontrolled furnace cool ("conventional+slow-cool" samples). An additional control sample was prepared using the same heat treatment up through the 1500°C soak; however, at the end of the soak the sample was quenched to room temperature by pulling the sample to the end of the furnace tube, well away from the heating zone ("conventional+quenched" samples). This quench took approximately two minutes.

4.2.2 Flash sintering experiments

Flash sintered samples were produced by inserting the platinum-coated green bodies between two solid Pt electrodes in the sample holder shown in Figure 4.1. The sample holder was loaded into a pre-heated 1050°C furnace and allowed to thermally equilibrate for 10 minutes; careful calibration indicates the samples stabilized at a starting temperature of 1020°C

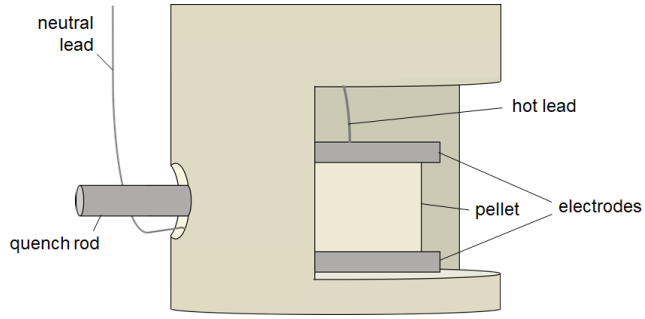

Figure 4.1 Schematic of a) the experimental setup used for flash sintering, showing loading and processing positions and b) a close-up of the sample holder showing quench rod.

due to the substantial convection present in vertical furnaces (see Chapter 2). A FLIR SC8300HD infrared (IR) camera monitored the temperature (see §2.3 for IR temperature calibration and data analysis details). Sample shrinkage was estimated from the IR footage based on the change in dimension, and calculated as $\frac{\Delta V}{V_o} = \frac{r_i^2 l_i}{r_o l_o} - 1$ where the subscript i indicates the instantaneous value.

A control system designed by Lucideon, Ltd. was used to deliver the desired current and voltage from a Pacific AMX-360 AC power supply to the sample. The software enabled a precise level of control over the rate at which the current was delivered. The software employs non-linear algorithms in conjunction with a real time computer, with control loop times typically set to 1 ms. The system is capable of providing voltage, current and power ramps with essentially zero overshoot, together with pulsed operation for thermal re-equilibration, if necessary. An

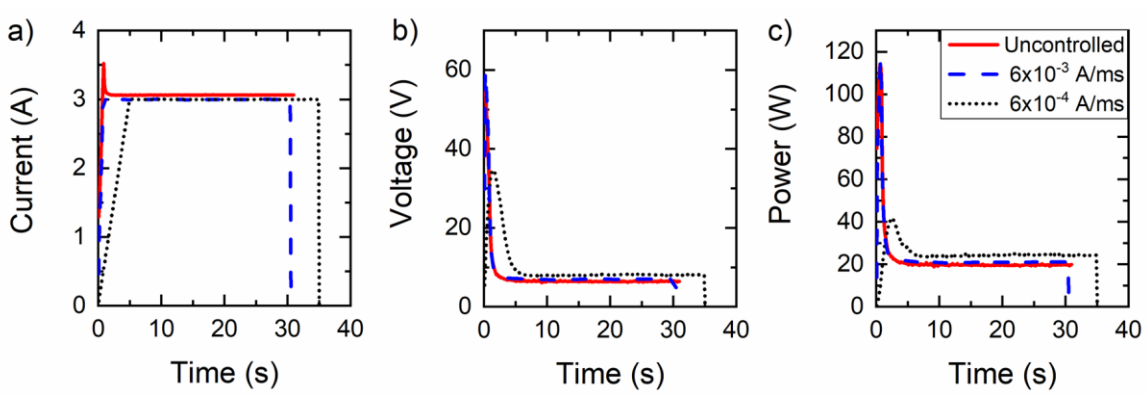

Figure 4.2 Characteristic examples of electrical data from the flash sintering process showing a) current, b) voltage, and c) power behavior

example of the electrical characteristics of a software-controlled flash experiment versus an uncontrolled, power-supply limited flash experiment is shown in Figure 4.2. The short dashed voltage profile in b is typical of current ramp rates slower than $6x10^{-4}$ A/ms.

Immediately after the desired electrical profile was completed, the power was turned off and there was a 30-60 second delay before the samples were quenched from the furnace. The cooling process amounted to a two-step quench: the first, from the flash temperature to roughly the furnace temperature at ~15ºC/s (estimated from real-time IR data); and the second, from the furnace temperature (1050 ˚C) to room temperature at ~8ºC/s (assuming a linear rate).

4.2.3 Flash sintering experimental sets

Three sets of controlled flash sintering runs were performed. In the first two sets, a maximum current of 3A (or 10.61 A/cm^2 current density) was specified. In the first set ("current ramp rate series"), the current was increased using ramp rates ranging from $6x10^{-3}$ A/ms ($2.1x10^{-2}$ A/cm^2*ms) to $1x10^{-7}$ A/ms ($3.5x10^{-7}$E-7 A/cm^2*ms) until the current setpoint was reached, at which time the current was held for 30s and then turned off. These runs were compared to an

Table 4.1 Summary of hold and total processing times used for the current ramp rate series and the current hold series. The shaded rows indicate the current ramp rate series values.

Current ramp rate (A/ms)	Hold time (s)	Total processing time (s)
$6x10^{-3}$	30	30.5
$6x10^{-4}$	30	35
$6x10^{-5}$	30	80
$6x10^{-6}$	30	530
$6x10^{-7}$	30	5030
$1x10^{-7}$	30	30030

additional set of samples processed using the traditional flash sintering approach; that is, the power supply was used to limit the current, while the control system was used only to measure the power supply output, with the Pacific on-board hardware given responsibility for controlling the current. The resulting uncontrolled profile is included in Figure 4.2. The range of ramp rates covered the fastest possible ramp – i.e. $6x10^{-3}$ A/ms, which was electrically equivalent to the uncontrolled samples except for the current overshoot – to a ramp with a timeframe comparable to conventional sintering, 8.3 hours.

In a second set of experiments, the effect of hold-time at maximum current was explored; these are termed "current hold series". The parameters used for this set of experiments are compared to the current ramp rate series in Table 4.1.

Finally, a third set of flash sintered samples were prepared to examine the spatial distribution of microstructural development during flash ("time series"). An intermediate current ramp rate of $6x10^{-5}$ A/ms was used, but the process was truncated at various points in time to produce a set of samples which represented the stages of flash sintering; the chosen points are reported alongside the results in Figure S1.

4.2.4 Finite element modelling

Transient thermal modeling was performed using ANSYS, a commercial finite element analysis (FEA) code. The model geometry included the sample, electrodes and immediate portion of the sample holder. An initial temperature of 1000oC was used. Boundary conditions were applied to the appropriate surfaces to account for convective and radiative heat losses. Joule heating of the sample was assumed to be evenly distributed and was therefore modeled by a volumetric heat generation calculated from the electrical power dissipation data and the initial dimensions of the sample. The modeling did not take into account the effects of either sample

shrinkage from densification or the system's electrical behavior, such as current concentrations from thermally produced gradients in conductivity. The transient analysis incorporated time steps of 50 ms over the 30 s period of the ramp and hold times. The mesh size used for the sample and electrodes was 400 um.

Due to the pressureless nature of the sample holder, the bottom electrode was not perfectly flush with the sample holder. This meant that, in the experimental setup, the sample and bottom electrode were not in ideal thermal contact with the alumina sample holder. To model this, a small air gap was placed between the electrode and sample holder in the FEA geometry. Since the thickness of the air gap could not be accurately measured experimentally, the gap size in the model was chosen such that the predicted surface temperature matched with that observed via IR measurements. Matching the surface temperature of the model to the experimental measurements by this method enabled an estimate of the sample's internal thermal profile.

4.2.5 Characterization

Electrical characteristics were measured via impedance spectroscopy for the conventionally sintered samples, the “uncontrolled” flash sample, and quenched versions of samples at each current ramp rate. The residual Pt paste was ground off of the samples with SiC paper, and the pellets were polished and sputtered with a clean layer of Pt for electrodes. Impedance spectra were measured using an HP 4192A impedance spectrometer from 5 Hz to 5 MHz and a 1V AC amplitude at five temperature steps between 290 to 370°C. The spectra were fitted to a two element equivalent circuit in which the high frequency element corresponding to the bulk conduction and the mid-range frequency element corresponding to the grain boundary conduction were each described by a resistor in parallel with a constant phase element (R||CPE); the two R||CPE elements were in series. A third, low-frequency contribution, corresponding to a

Warburg peak, was not included in the fitting. The bulk conductance values were normalized by the sample dimensions, while the grain boundary conductance values were normalized using the brick layer model, which assumes 1) a relatively uniform grain size and 2) a grain size substantially larger than the space charge layer (*4, 109*). This allows for comparison of the specific grain boundary conductivity values, normalizing for difference in microstructure between samples.

The density of each sample from the current ramp rate sweep and equivalent time/energy sweep was measured using the geometric and Archimedes methods after the residual platinum paste was removed from each electrode. For microstructure analysis, the samples were cross-sectioned, mounted, and polished down to 0.25 um diamond paste. The cross-sections were imaged using ion channel contrast imaging, which prevented the need for thermal etching and possible grain growth. Grain size measurements were performed using the linear intercept method and a correction factor of 1.56 (*148*). The density of each sample from the time series was measured geometrically; these pellets were fractured and imaged in a FE-SEM (FEI Verios 460L).

4.3 Results

4.3.1 Calibrated temperature profiles during flash

All samples exhibit the same thermal trend as the current increased, shown in Figure 4.3. The heating rate measured from the surface was roughly linear and proportional to the current ramp until the current limit was reached, at which point the temperature decreased slightly. Only the slowest current ramp rates did not exhibit this slight temperature overshoot.

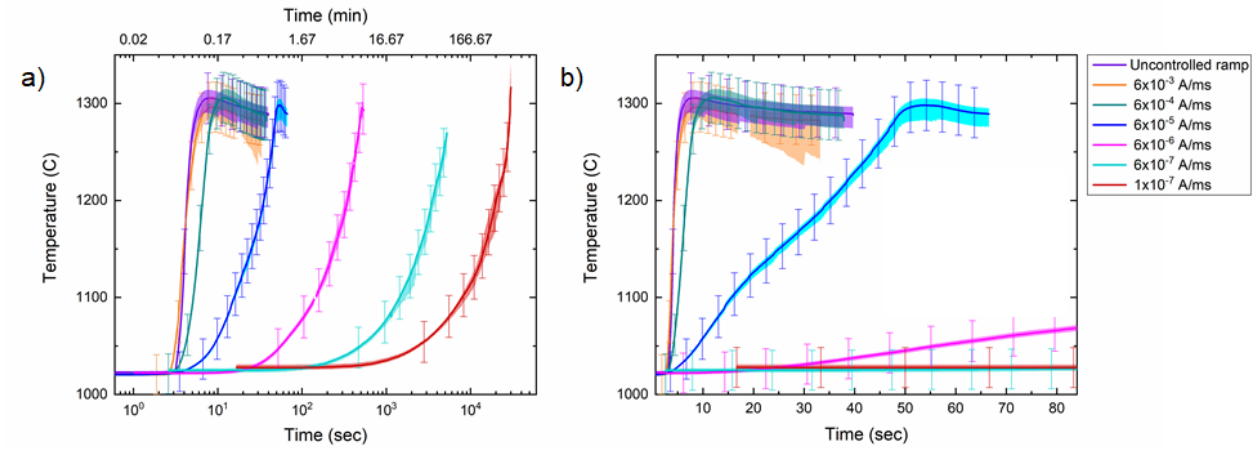

Figure 4.3 Surface temperature profile for each current ramp rate. A log plot (a) is required to compare all ramp rates, while a linear axis (b) exemplifies the linearity of the heating rate. The bold line depicts the median temperature, the colored region the interquartile range, and the error bars are the manufacturer-reported camera error of 2%.

As an example, the cross-sectional profile from the FEM simulation of a $6x10^{-3}$ A/ms experiment is shown in Figure 4.4. When the current maximum was reached, a temperature gradient of ~100°C existed between the center of the sample and its edges; this gradient was smaller between the sample center and electrode regions, ~60°C.

The sample shrinkage was estimated from the IR footage for the current ramp rate sample series are plotted versus temperature in Figure 4.5; error bars are shown from only one representative sample for clarity. Data collection was continuous; the apparent discontinuities result from resolution limitations of the camera and the pixel-by-pixel nature of the dimensional change. The majority of the shrinkage occurred during the non-isothermal portion of the flash

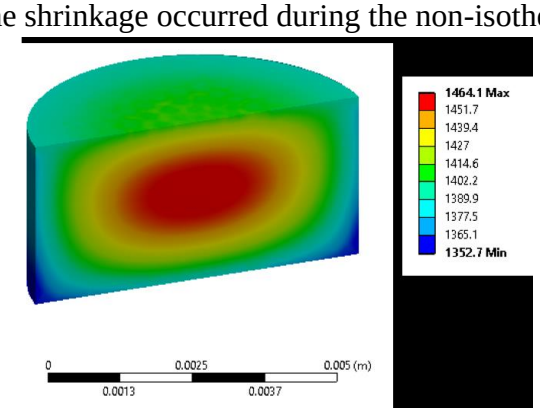

Figure 4.4 Using the power dissipation of a $6x10^{-3}$ A/ms sample, FEM results for a cross-sectional temperature profile during the current maximum. (FEM courtesy of Steven Funni)

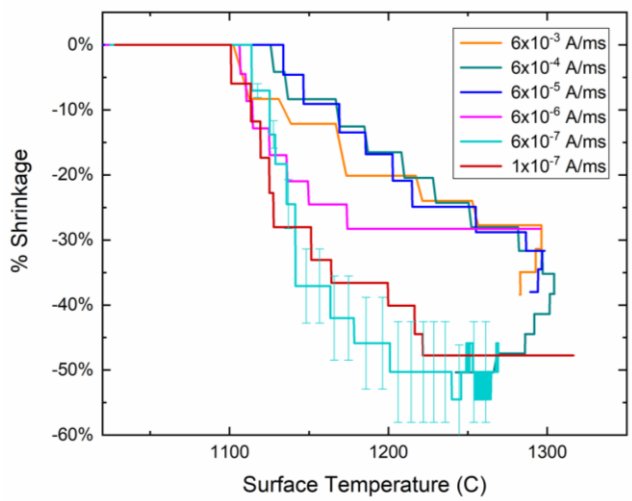

Figure 4.5 Shrinkage estimates from current ramp rate series IR footage plotted versus the measured surface temperature.

process, although in the faster ramped samples some densification did occur during the 30 s current hold. In the slower-ramp-rate samples, final density was often reached before the current limit was reached.

4.3.2 Density trends

Final sample densities for the current ramp rate and current hold series are shown in Figure 4.6 as a function of current ramp rate and total processing time. The sample density increased as the current ramp rate decreased; note that the density of the current hold series correlated well only to the ramp rate, not to total processing time. For comparison, the conventionally prepared sample were fully dense (~100% theoretical density).

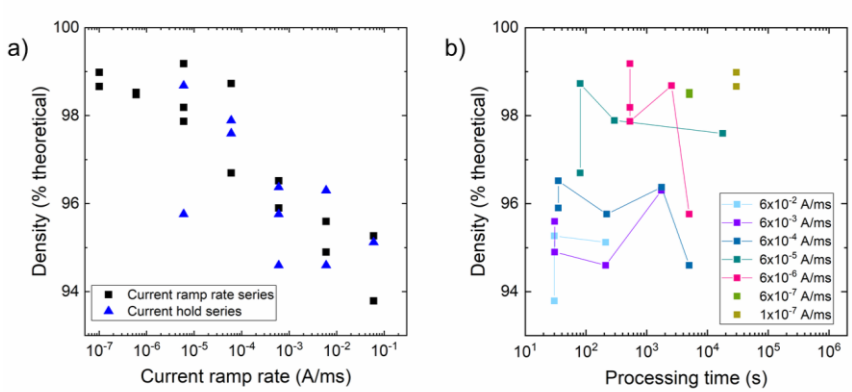

Figure 4.6 Archimedes densities for flash sintered samples from the current ramp rate and current hold series plotted against (a) current ramp rate and (b) total processing time. Error bars are smaller than the marker boundary.

4.3.3 Final microstructure

As shown in Figure 4.7 and Figure 4.8, within the current ramp rate series grain size stayed relatively constant until the ramp rate exceeded $6x10^{-6}$ A/ms, or a ramp time of about 8.5 minutes. The sample edges and electrodes generally also exhibited slightly smaller grain sizes than the sample center (Figure 4.7). This disparity appeared to increase in the samples which saw grain growth, but the difference remained ~30% of the center grain size.

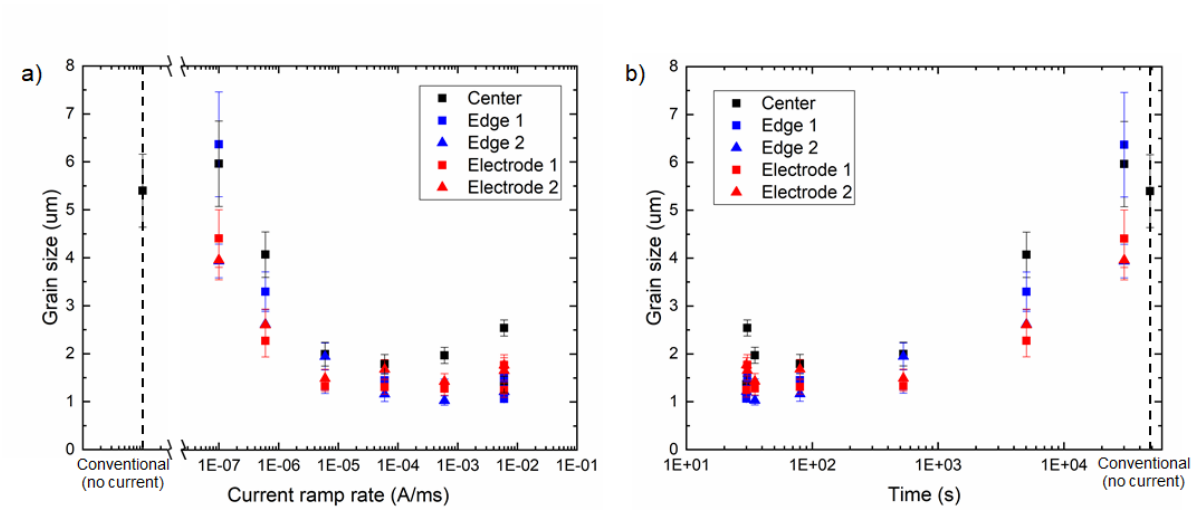

Figure 4.7 Grain sizes for current ramp rate sweep samples at various ramp rates and positions in the samples plotted (a) against current ramp rate and (b) against the amount of time spent above 1000°C.

4.3.4 Electrical properties as a function of current ramp rate

As shown in Figure 4.9, there are distinct differences between the electrical characteristics of the flash sintered samples and the conventionally prepared samples; however, most of the measured and calculated parameters seem fairly insensitive to the actual value of the current ramp rate, with the exception of the slowest ramp rate. Both the bulk and grain boundary sintered samples seemed to be consistently higher than the conventional+slow-cooled sample, although the differences in the bulk conductivity are small enough to be technically within error. The conventional+quenched sample exhibited a higher bulk conductivity than both the furnace

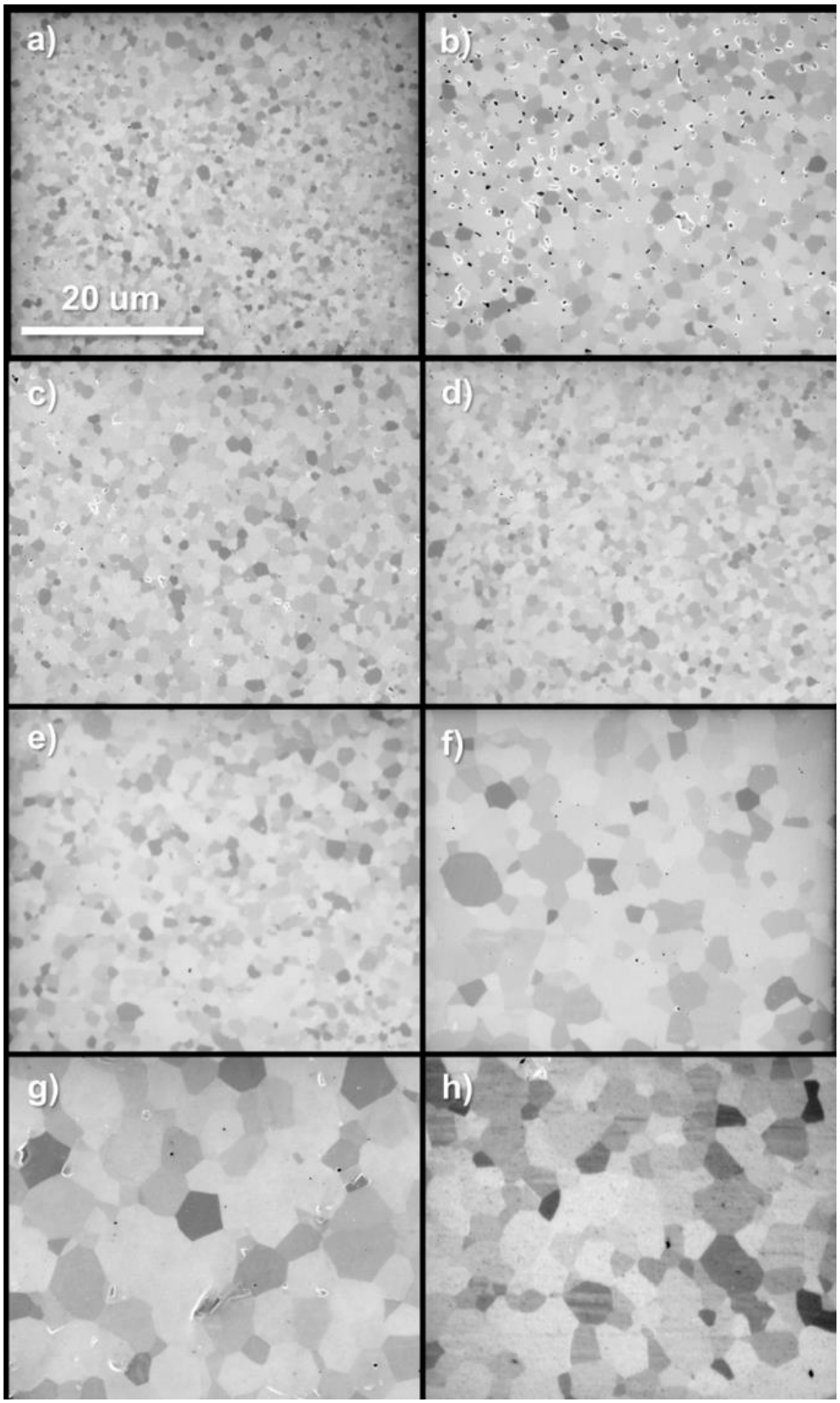

Figure 4.8 Microstructure images comparing samples flashed sintered without current ramp control (a), with current ramp rates of $6x10^{-3}$ A/ms (b), $6x10^{-4}$ A/ms (c), $6x10^{-5}$ A/ms (d), $6x10^{-6}$ A/ms (e), $6x10^{-7}$ A/ms (f), and $1x10^{-7}$ A/ms (g). The conventional+slow-cooled sample is shown in (h). conductivities of the flash technically within error.

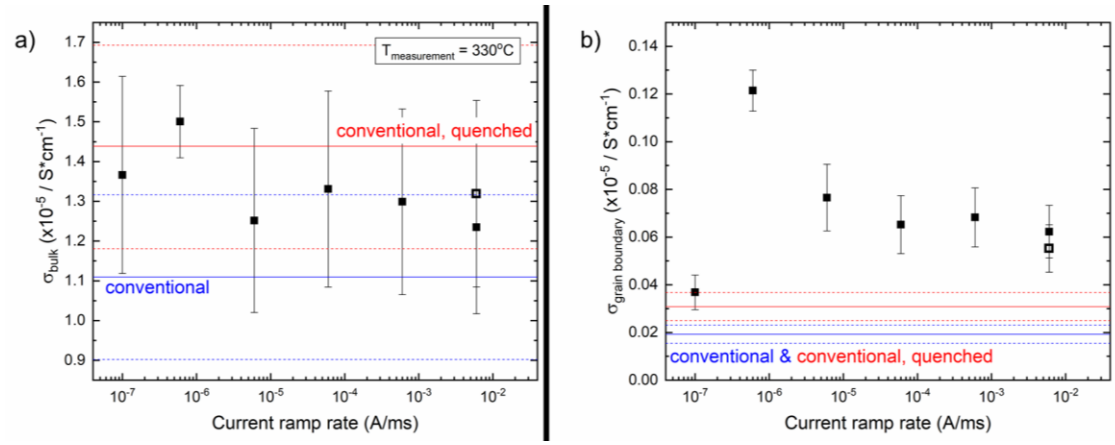

Figure 4.9 a) Bulk and b) grain boundary conductivity values at 330ºC. The measurement for the conventional, furnace cooled sample is shown in blue, the conventional, quenched in red, and their error bars are shown as dashed lines. The open square indicates the value for the uncontrolled flash sample.

cooled and flash sintered samples, although it was closer to the flash sintered samples.

Table 4.2 reports activation energies ($E_{a,bulk}$ and $E_{a,gb}$) and grain boundary thickness ($\delta_{gb,avg}$) calculated from the Arrhenius plots and brick layer model. $E_{a,bulk}$ remained around the same value as the conventional+slow-cooled sample while $E_{a,gb}$ of the flash sintered samples was consistently higher, again with the exception of the slowest flash ramp rate. The grain boundary thicknesses for all flash sintered samples were also substantially larger than conventional+slow-cooled except again for the slowest flash ramp rate.

Table 4.2 Additional electrical parameters reported for several current ramp rates.

Current ramp rate (A/ms)	$E_{a,bulk}$ (eV)	$E_{a,gb}$ (eV)	$\delta_{gb,\ avg}$ (nm)
6x10^{-3}	1.079 ± 0.006	1.143 ± 0.006	43 ± 3
6x10^{-4}	1.089 ± 0.007	1.150 ± 0.010	30 ± 3
6x10^{-5}	1.064 ± 0.006	1.126 ± 0.010	26 ± 3
6x10^{-6}	1.092 ± 0.002	1.141 ± 0.014	26 ± 3
6x10^{-7}	1.080 ± 0.009	1.168 ± 0.006	280 ± 3
1x10^{-7}	1.069 ± 0.005	1.094 ± 0.004	13 ± 2
Conventionally sintered	1.077 ± 0.007	1.115 ± 0.006	10 ± 2

4.4 Discussion

4.4.1 Thermal profile and absolute temperature

The relatively good agreement between the surface IR and FEM predicted temperatures allows us to estimate the thermal distribution inside the pellet during flash sintering. The internal average temperature of 1417°C can be compared to a recent synchrotron study of AC flash sintering of 8YSZ from Charalambous et al. (*76*); while the time resolution in the IR data is finer than in synchrotron studies, the bulk nature of the diffraction measurement provides a complementary comparison. When the Charalambous study used a current density of 10 A/cm^2 and a 6 mm diameter x 3.5 mm pellet– i.e. highly similar sample form factor and current density– a steady state temperature of ~1500°C was measured, in reasonable agreement with the estimate in this study, especially given the difference in thermal boundaries.

4.4.2 Stagnation of densification with time and its apparent dependence on current ramp rate

A dependence of density on current ramp rate was also reported in the DC current ramp control study from Charalambous et al., but its reason was not discussed (*144*). We consider here three possible explanations for the apparent dependence of density on current ramp rate: 1) the fast ramp samples simply see less thermal energy; 2) rapid densification of sample edges and electrode regions applies some constraint; or 3) slower ramp rates allow for finer microstructure control which produces denser samples.

The most straightforward explanation for increasing density with decreasing current ramp rate was that the faster ramped samples saw less thermal energy. The slower ramp rates take longer to reach the same current level used in each experiment; this delay means that these samples both dissipate more energy overall and are subject to the higher temperatures of flash sintering for longer periods of time. The current hold series of samples casts strong doubt on this

possibility. If the samples simply required more energy or time, Figure 4.6b should have shown an increase in density with time for samples using the same current ramp rate. Instead, the densities of this set did not improved but fell within the general experimental scatter of the first set. It appears that the initial densification rate limits the final density.

The next possible explanation for the stagnation effect was that the edges/electrodes of each sample were densifying faster than the center, and either introducing a mechanical constraint or trapping gas within the ceramic structures. The microstructural inhomogeneity plotted in Figure 4.7 provides some support for this idea; smaller grains were observed around the edges of the sample, and smaller grains are often correlated with faster rates of densification. However, the time series microstructures in Figure S1 indicate that, if anything the electrodes densify slower, not faster, than the sample center. As discussed in a later section, the temperature distribution is more likely responsible for the smaller grains. Of course, this does not rule out the possibility of some mechanical constraint from the metal electrode; however, that effect would not show a dependency on ramp rate.

The remaining hypothesis uses the idea of microstructure refinement. Uneven microstructure development leads to a broad distribution of grain sizes and pore sizes. With a broad pore/grain size distribution, the outlier pores tend towards early pinch-off, resulting in closed porosity at relatively low densities. This effect results from two mechanisms. First, large curvature pores shrink preferentially due to a higher local sintering stress; this can increase the macroscopic separation of particles during the earlier stages of sintering, increasing some pore sizes as the smaller pores sinter preferentially (*149*). Second, in the later stages of sintering, the pores are bound to grain boundaries only as long as their drag force is adequate to counter the force for grain growth (*150*). The force for growth of a given grain is dependent in part upon the

ratio of its grain size to average grain size (*151*). The greater than one this ratio is, the larger the driving force for growth, and the larger the pore drag force must be. In other words, the critical pore size, below which pore de-pinning occurs, is larger, which means pores de-pin at a relatively lower overall density. Once trapped in the lattice, pore removal is dependent upon the slowest diffusion pathway, through the bulk (*151*). In both of these cases, a broader pore/grain size distribution means that at any given time or temperature, a greater fraction of the population of pores is shrinking and pinching off prematurely. The detrimental effects of gas trapped inside of pores upon the transition of a sintering body from open to closed porosity has been empirically demonstrated in systems such as alumina (*152*) and porcelain (*153*). The significance of the effect depends on the diffusivity of the gas in the material (*154*). In these experiments, trapped gas would explain why additional heating did not improve the density of samples with fixed microstructures.

The increasing relevance of gas-trapping with increasing current ramp rate lies in the link between sintering rate and microstructure development. While inhomogeneous pore distributions are most often associated with inhomogeneous green bodies (produced from e.g. incomplete binder burnout); however, they are also associated with rapid densification. Studies on the technique of rate-controlled sintering (RCS) have explored the link between sintering rate and microstructure development. Several studies from Palmour et al. (*155-158*) demonstrated that optimal microstructures (i.e. dense and small grained) were produced not with the fastest possible densification rate, but by a controlled, non-linear thermal process which approached densities between ~75-100% more slowly and with a more linear shrinkage rate than conventional sintering. This approach often required the sample to spend most of its processing time at elevated but intermediate temperatures, approaching or exceeding conventional

temperatures only in the final stage of sintering. Palmour credited the effectiveness of this technique to a homogeneous pore distribution and retained grain size. Finer grain sizes produce smaller pores, and a homogeneous grain size distribution produces a more homogeneous pore distribution, so the relatively lower temperatures of RCS, at which grain growth is not as rampant, facilitated an ideal pore distribution.

While the heating rate for flash sintering is linear, unlike in RCS, the dominant temperature range in RCS is not unlike that of the slower flash sintering ramp rates in this work. For ramp rates greater than $6x10^{-5}$ A/ms, much of the processing time was spent at temperatures lower than conventional sintering temperatures. In fact, shows that when a slow ramp rate is used, most of the densification occurs before the maximum temperature is reached. It is also in this mid-range where this study finds an optimal combination of high density, controlled grain size, and small macroscopic grain size distribution. This relationship between flash and rate-controlled sintering is particularly promising because there is potential for the development of microstructure optimization with finer-tuned control and less power consumption than a furnace-based process like RCS. For example, the control software used in this study can include real time pyrometric feedback together with segmented ramps and holds.

4.4.3 Grain size dependence on current ramp rate

To compare the amount of grain growth during flash sintering to that of the conventional+slow-cooled sample, the grain size data from Figure 4.7a is replotted in Figure 4.7b as a function of time spent above 1000°C. This temperature was chosen as the lowest temperature at which grain boundaries may be mobile. Grain growth was onset at times above ~1000s, and the amount of growth in the conventionally sintered sample was generally in agreement with the trend demonstrated by the flash samples. This dependence of grain size on

time agrees well qualitatively with the conventional picture of grain growth. Actual grain growth occurs only when a critical pore size (and corresponding density) is reached such that the pore no longer effectively pins the grain boundary (*150*). The longer held samples reach the critical density/porosity relatively earlier in their run (see Figure 4.5) and spend more time in the regime of active grain growth.

Within this study, there is no need to invoke electric field-based mechanisms to explain the observed pattern of grain growth; this study is not intended to be a robust examination of grain growth under field. Other studies have attempted to address the question of field effects on grain growth, but most of them do not compensate for the effects of Joule heating; for example, the comparison study from Charalambous (*144*) reported enhanced grain growth during flash but did not include a measurement of final sample temperature. A recent exemption to this oversight is a study from Cao et al. in which the furnace temperature was reduced during field-assisted sintering to compensate for Joule heating effects (*159*). Cao's work indicates that there is likely some interplay between the field and grain boundary. A recent review from Chaim et al. (*160*) gives a general overview of the work in this area; however, further studies which include robust temperature measurements and/or thermal compensation in AC systems should be performed to establish field effects on grain growth absent electrochemical reduction/oxidation.

4.4.4 Grain size dependence on position

The variation of grain size within each sample is easily understood as an effect of the thermal profile predicted by the ANSYS model (see Figure 4.4). The edges and electrode-adjacent areas stayed consistently cooler than the sample center and spent less time at higher temperatures. The opposite of this effect was reported previously during the AC flash sintering of 3YSZ (*38*), and the skin effect was suggested as a possible explanation. However, the skin

depth can be estimated as $\sqrt{\frac{2\rho}{\omega\mu}}$; approximating μ_r as 1 and using the resistivity measured for our conventional+slow-cooled sample, δ =~192 cm at 1000 Hz and 1020ºC. As such, it seems unlikely that the skin effect factors into the flash sintering of such small samples. The discrepancy between the two studies may come from the sampling; grain size measurements in the previous study were only reported from the polished surface of the samples, so the small "center" grains were not truly in the thermal center of the sample.

4.4.5 Electrical properties of flash vs. conventional sintering

Before discussing the conductivity trends in Figure 4.9, it should be noted that, in general, studies comparing the electrical conductivity of flash sintered samples to conventional are inconsistent at best. Neither Muccillo et al. (*40*) nor Steil et al. (*29*) reported an increase in the bulk conductivity of 8YSZ upon flash sintering (although the analysis from the Steil study was qualitative, not quantitative) while Vendrell et al. did (*39*). Similarly, for 3YSZ, Christian et al. reported similar behavior for flash and conventionally sintered samples (*41*), while Carvahlo et al. saw increases in both bulk and grain boundary conductivity (*36, 38*). The previously referenced ZnO study with current ramp rate control saw variations in conductivity relative to the conventionally sintered sample (*144*), but these seemed largely due to differences in density.

There are two factors in flash sintering that tend to vary from study to study and which will have a significant impact on the electrical characteristics of flash sintered samples: the quench nature of flash sintering and the choice of DC or AC electric field. First, it must be noted that a thermal quench is inherent to the flash sintering process. Several previous studies agree with this investigation's findings that the internal temperature of a sample is increased substantially by Joule heating during flash (*76, 88, 96*); when the current is shut off, this Joule heating is abruptly stopped, and the sample is effectively quenched from this higher temperature

to the furnace temperature. As mentioned previously, the quench rate in this study was ~15°C/s. The effect of this quench will be more substantial when high current densities and low furnace temperatures are used, as the discrepancy between the in-situ and furnace temperatures is higher and defects at lower furnaces temperatures will be less mobile.

The second factor is the choice of AC or DC. The reduction of mixed/ionically conducting oxides under a DC field is well established, especially in the presence of electrodes which are not fully reversible (*127, 128*). In YSZ specifically, under high current densities, inadequate amounts of oxygen are available at the cathode to reoxidize the vacant oxygen sites (*78*), which can lead to an increased concentration of mobile oxygen vacancies. The discrepancy in literature among 8YSZ measurements may be due to the use of DC in the Vendrell study and the choice of AC in the Muccillo and Kleitz studies. The disagreement among the 3YSZ studies is a bit more surprising, as all three used AC fields. However, looking at the data itself, the discrepancy may be a difference of opinion; the differences in bulk conductivity in particular, without error bars, are subtle.

This investigation used AC; we suggest that is why a significant increase in bulk conductivity was not evidenced, in accordance with the Steil/Muccillo/Vendrell comparison. The slight increase can be attributed to the quench of the samples, as demonstrated by the comparison to the conventional+quenched sample in Figure 4.9. In fact, the FEM results indicate that the conventional+quenched sample was quenched from a higher average temperature, which may explain its status as the most conductive sample. Increases in both bulk and grain boundary conductivity have also been reported in literature upon quenching in YSZ (*161, 162*); this increase results from a greater number of mobile oxygen vacancies. At high temperatures, the oxygen vacancies in fluorite structures are considered freely dissociated, but at lower

temperatures they form associations with charged dopants, i.e. Y'_{Zr}-$V_{\ddot{o}}$ in this case (*161, 163, 164*). Rapidly cooling YSZ to a temperature below which oxygen vacancies and cations are considered mobile prevents the equilibrium concentration of defect clusters from forming, resulting in higher bulk conductivity at lower temperatures.

Contrary to the bulk conductivity, the differences in grain boundary conductivity were higher than both the conventional+slow-cooled and conventional+quenched samples by a subtle but persistent factor of ~4, until the slowest current ramp rate. There are a number of potential factors which have been demonstrated in literature to affect grain boundary conductivity in YSZ, including non-field based dependencies such as grain size (with changes evidenced in grain sizes up to ~4 um) (*165*). However, the results in this study are inadequate to determine the origins of this interesting effect. Small variations in the $E_{a,gb}$ do occur here, but their fluctuations do not indicate any kind of trend, and while there is also a persistent increase in $\delta_{gb,\ avg}$ in flash sintered samples (as previously reported in (*41*)), the specific values are too variable within the study to indicate a specific cause. Additional work is underway to better understand the fundamental cause of this effect.

4.5 Conclusions

In flash sintering with current-ramp-rate control, final density is principally determined by the rate at which sintering occurs. This is consistent with conventional sintering and implies the predominance of the thermal profile in determining macroscopic (or microstructural) sample properties. Overall, grain growth is prevented at or below mid-range ramp rates; absolute inhomogeneity between sample regions is reduced below this point as well, although the relative disparity appears fairly constant. At very slow ramp rates, the long exposure to temperature produces a relatively large grain size. The electrical conductivities are insensitive to specific

ramp rate values; based on prior results, one can safely attribute this property to thermal history, i.e. maximum temperature and quench temperature. On the other hand, grain boundary electrical characteristics like the impedance are modified by flash sintering, but more work is needed to pinpoint the origins of this result.

Based on these results, we suggest that the rapid densification during flash is predominantly a thermal effect, perhaps enhanced by an increase in sintering stress due to applied field. This is the most consistent perspective in the context of literature. Densification in 60 s at 1300°C has been accomplished in nano-grained YSZ using rapid heating only (*68*). Ji et al. similarly demonstrated that this rate of densification could be accomplished by several different methods of rapid heating (*61*). Roura et al. demonstrated mathematically that a rapid shrinkage rate can in fact be explained by the material reaching an elevated temperature while still in a highly sinterable, high energy state (*73*). Differences in properties such as grain boundary characteristics have been reported for alumina prepared by fast firing (*166*). We cannot preclude some amount of field interaction, especially in light of studies such as Cao's (*143*), but it does not seem necessary to invoke new field-derived mechanisms to explain the vast majority of flash sintering characteristics.

Of more practical importance is this study's demonstration that the densification process can largely be explained be interpreted in terms of well-established thermal sintering principles, in agreement with the suggestion by Ji et al. in their robust study on the various forms of rapid heating (*61*). Indeed, before crediting the electric field with the impartation of any remarkable properties, particular care should be taken to consider whether the microstructure and inherent quench character of flash sintering can explain the observed "unusual" properties e.g. the grain size dependence of grain boundary conductivity in conventionally sintered YSZ.

4.6 Supplemental material

Figure S1 shows the microstructural development in the sample center and electrode region at different points in time during the flash sintering process. Individually, the microstructure in both areas develops along the classical lines; that is, neck formation and growth transition into an open, porous network, which pinches off into a set of isolated pores in the last stage of sintering (*3*). However, it is apparent, especially in the higher density stage, that the electrode lags the sintering rate of the center. Given the temperature gradient between the sample center and electrode, this is not surprising (Figure 4.4).

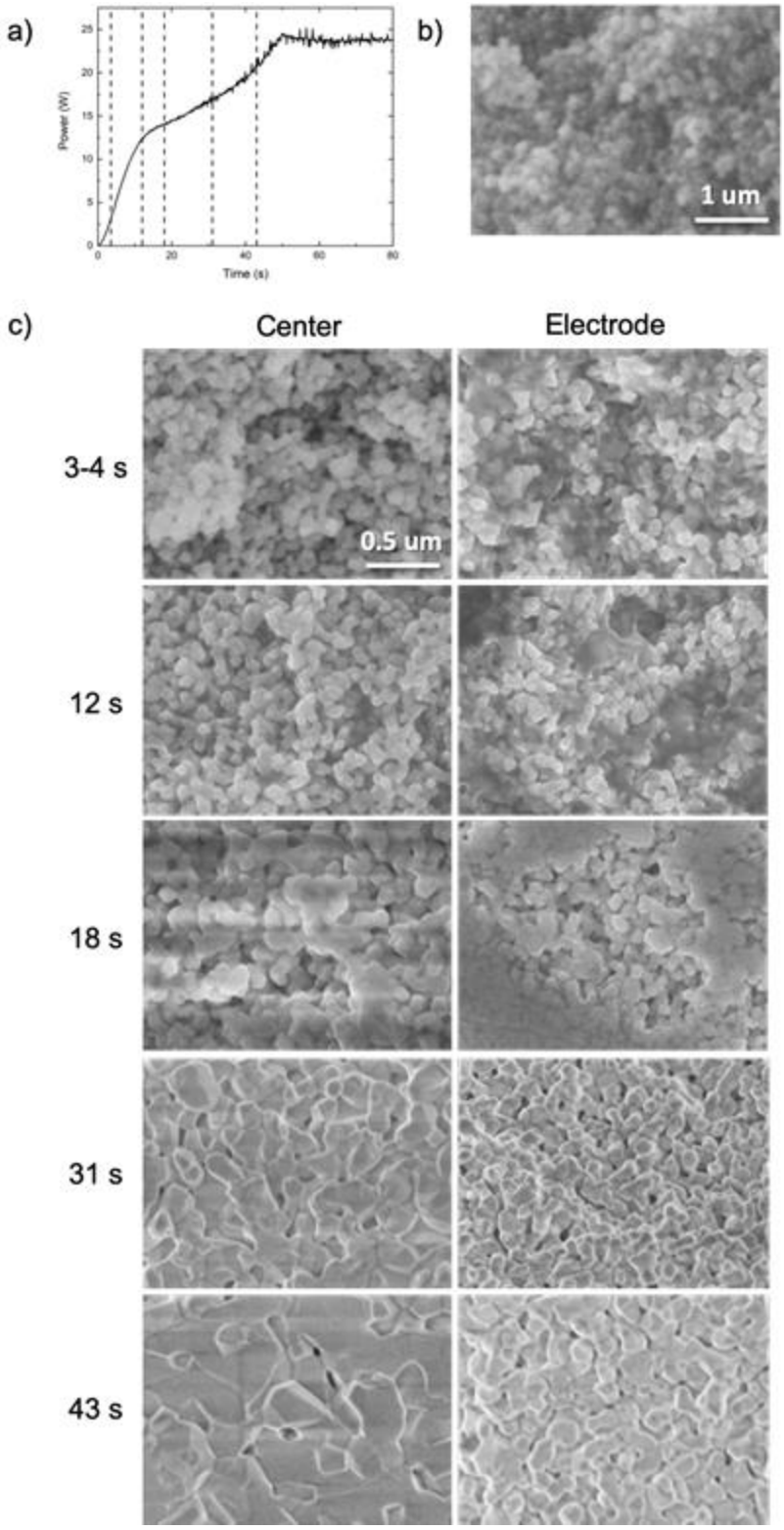

Figure S1 a) Points in time and their corresponding power for each sample in the time series, b) green body microstructure, and c) a series of images showing microstructure development as the flash process progresses.

CHAPTER 5

Investigations into the Origins of Enhanced Grain Boundary Conductivity in Flash Sintered Ceramics

Chapter 4 reported a consistent and subtle increase in both bulk and grain boundary conductivity in flash sintered samples as compared to conventionally sintered samples. When compared to a conventionally sintered, quenched sample, the difference in bulk conductivity appeared easily explained by the retained high temperature state, but the grain boundary conductivity increase remained substantially larger than the quench effect. The work contained in this chapter sought to further elucidate the fundamental causes behind this conductivity trend.

5.1 Background

Limited data is available in literature on changes in the microstructure and composition of grain boundaries upon flash sintering, and most of the relevant studies have used DC fields. Many of the findings therefore appear related to reduction/oxidation effects, such as accumulated stacking faults in ZnO which are linked to increased point defect concentrations (*146*) and anode-localized amorphous and Ce-rich grain boundaries in CeO_2 (*80*). In $K_{0.5}Na_{0.5}NbO_3$, gradients observed in grain boundary composition are related to localized melting (*58*). The one specific study using YSZ predominantly compares samples flash sintered in air and Ar (*167*). In comparison to conventionally sintered YSZ, the authors note increased concentrations of

dislocation arrays and observe Y segregation to the boundary in the flash sintered sample only; this latter finding contradicts a number of more robust measurements characterizing conventional stabilized zirconia, in which cation segregation is consistently observed (*2, 168, 169*).

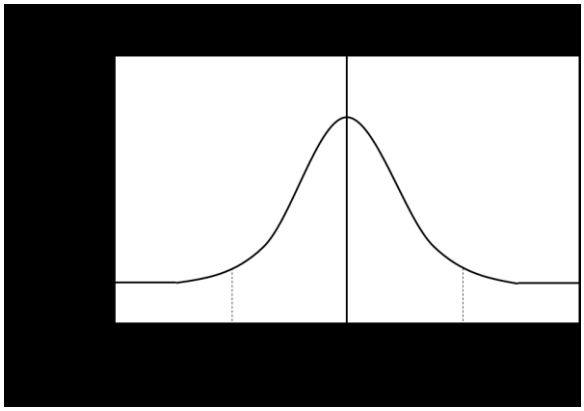

Figure 5.1 Schematic of expected Y segregation to the grain boundary. Distance and ration values are pulled from (2, 4).

Outside of flash sintering literature, the grain boundary conductivity in YSZ is fundamentally determined by the combined Y and oxygen vacancy segregation, which produce a positively charged grain boundary core surrounded by a negative space charge (*4*); the approximate magnitude of segregation and the thickness of the layer is schematically depicted in Figure 5.1. This electrical blocking layer manifests in a specific grain boundary conductivity 2-3 orders of magnitude lower than the bulk (*4, 165*). The space charge is modified by local grain boundary orientation (*170*), with electrical measurements across a polycrystal recording a sample average. Empirically, the measured conductivity is also sensitive to a number of processing factors including cooling rate (*171*), quench temperature (*161*), and grain size (*165*).

Based on this understanding, we suggest four possible explanations underlying the increase in grain boundary conductivity in flash sintered samples. First, flashed samples could contain a non-random grain boundary orientation distribution, manifest as either global texturing or local misorientation preferences. Second, it is possible that an impurity silica phase, commonly found at grain boundaries in YSZ (*4, 171*), was present and redistributed by rapid

densification or quenching (*165, 172*). Third, there may be a high temperature complexion – that is, a grain boundary "phase" (*173*) –for YSZ grain boundaries which is retained by the thermal quench and may manifest in structural ways such as facet formation, interfacial disordering, etc. Finally, there may be changes in the degree of dopant segregation that influence the space charge layer and therefore reduce the electrical blocking effect. This concept is similar to the idea of grain boundary complexions, but could also result from the quenched-in high temperature state, from interactions of the electric field with the space charge, or from local variations in microstructure. The following experiment and analysis expand on the findings in Chapter 4 in an effort to probe the likelihood of each of these prospects.

5.2 Methods

In this study, a small sample set was examined to focus on the fundamental differences between flash sintered and conventionally sintered samples. Control samples were prepared two ways: one was sintered conventionally at 1500°C for four hours, cooled at 20°C/h to 1000°C, and then furnace-cooled to room temperature ("conventional+slow-cool"); the other was sintered conventionally at 1500°C for four hours but quenched from this temperature by pulling the sample boat from the furnace at the end of the soak ("conventional+quench"). The control samples were compared to a sample flash sintered with a maximum current of 3A, a controlled current ramp rate of $6x10^{-6}$ A/ms, and a 30 s hold at the current maximum. The flash sintered sample was quenched from the furnace within a minute of the field being removed. Pellet preparation, the flash sintering setup, and procedure follow that detailed in Chapter 4. Each sample type was prepared at least twice.

The comparison and flash sintered samples were sputtered with Pt, characterized electrically by impedance spectroscopy, and fit to a two-R/CPE element equivalent circuit to

extract the bulk and grain boundary conductivity values. The grain boundary conductivity was normalized for microstructure using the brick layer model (*109*) and thus the reported values represent the specific grain boundary conductivity. After electrical characterization, these samples were cut in half, mounted, and polished. The microstructure of the sectioned samples was imaged using ion channel contrast imaging. θ-2θ XRD scans were performed on the intact duplicates of the flash sintered and conventional+slow-cooled samples. An additional sample flash sintered at $6x10^{-4}$ A/ms, with a 3A maximum and a 30 s hold was included for TEM analysis.

Duplicates of all three types of samples were annealed at 1500ºC for 8 hours (heated at 300ºC/h to 1000ºC then 100ºC/h to 1500ºC), cooled at 20ºC/h to 1000ºC, and allowed to furnace cool to room temperature. After cooling, a new layer of Pt was deposited and the electrical characterization was repeated.

5.3 Results

5.3.1 Effects of post-annealing on conductivity

An Arrhenius plot of the bulk and grain boundary conductivities is shown in Figure 5.2a and b. The quenched sample exhibits the highest bulk conductivity, followed by the flash sintered sample, and then the furnace cooled sample. Upon annealing, the bulk conductivity of the conventional+quenched sample decreased and that of the conventional+slow-cooled sample increased, aligning with the flash sintered sample at roughly the same value (shown in the inset).

Due to its high oxygen ion transport number, the bulk conductivity may be considered to be proportional to the number of mobile oxygen vacancies at a given temperature. As discussed in Chapter 4, many of the vacancies in YSZ at low temperatures are immobilized in defect clusters with Y'_{Zr} (*164, 174*). At high temperatures, however, effectively all oxygen vacancies are

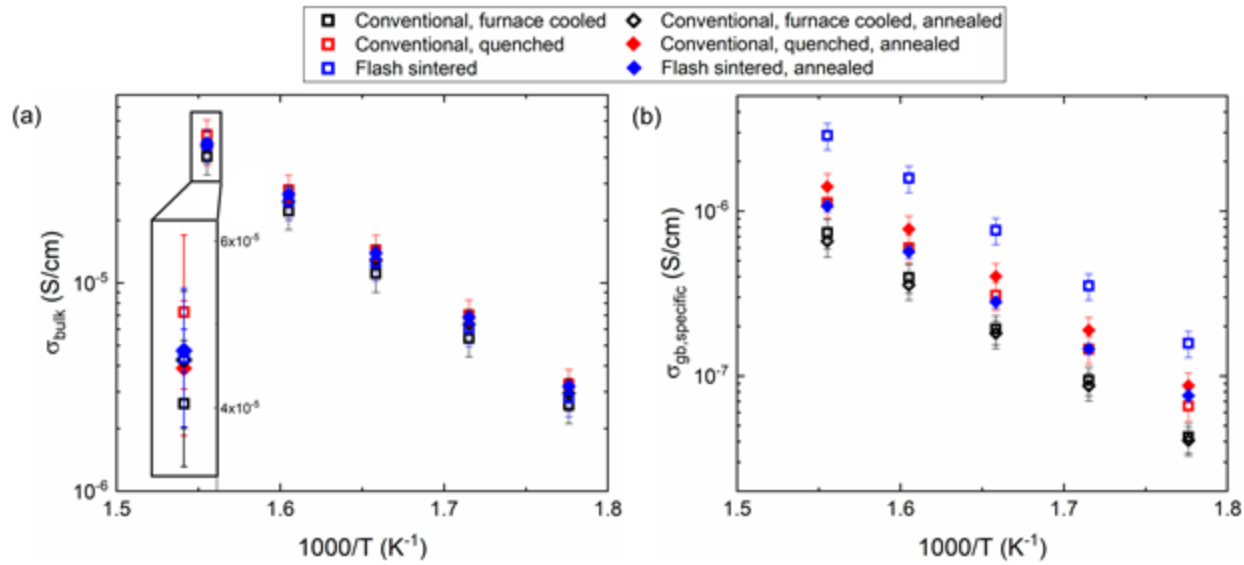

Figure 5.2 Arrhenius plots of (a) bulk and (b) specific grain boundary conductivities.

considered mobile. This phenomenon partially explains the temperature dependence reported by Park and Blumenthal (*116*) despite the theoretical pinning of the oxygen vacancy concentration by the dopant, as well as the change in activation energy "knee" commonly reported in the Arrhenius plots of YSZ conductivity. In quenched samples, increases in the bulk conductivity of conventionally sintered and quenched YSZ have been previously reported (*161*), resulting from an increased number of mobile oxygen vacancies as the equilibrium concentration of $V_O^{\cdot\cdot}$-$Y_{Zr}^{'}$ complexes are prevented from forming.

Our earlier results comparing conventional+quenched samples to flashed samples indicated that the built-in quench of flash sintered samples retained more mobile defects. The results after annealing each of these samples support this interpretation: regardless of thermal history, all samples are returned to the same bulk defect state when subject to the same thermal process. There are no fundamental residual changes in the defect state.

On the other hand, the grain boundaries behave quite differently from the bulk (see Figure 5.2b). Both the flash sintered and conventional, quenched samples exhibited higher grain

boundary conductivities than the conventional+slow-cooled sample; however, the grain boundary conductivity for the flash sintered sample is the most conductive by a substantial margin. Furthermore, the high temperature anneal produced dissimilar effects. While the furnace cooled sample retained the same grain boundary conductivity, neither the quenched nor flash sintered sample aligned with the final furnace-cooled value after annealing. The quenched sample remained effectively the same, and still more conductive than the furnace cooled sample, while the conductivity of the flash sintered sample did decrease, but only to the value of the quenched sample, not to the value of the furnace cooled sample.

These results suggest that there may be two contributions to enhanced grain boundary conductivity. The first is relatively stable after formation; that is, post-annealing has a limited ability to affect it. This effect is likely the common cause of the enhanced conductivity in the quenched sample and the retention of some enhanced conductivity in the flash sample, especially given that its conductivity sits around the same value as the quenched sample. Possible physical causes are discussed below. The second contribution then is much more alterable and is evidenced only in the flash sintered sample, which may mean it is based on oxygen vacancy or cation segregation to the grain boundary, factors which would return to equilibrium upon a high temperature anneal.

5.3.2 Additional analysis of flash sintered YSZ

Figure 5.3 shows the XRD spectra of the flash sintered sample and the conventional+slow-cooled sample. The spectra are remarkably similar, with a slight asymmetry in the flash sintered peaks due to residual strain from the Pt removal process. The flash sintered peaks are also slightly broader due to the smaller grain size. The peak splitting at higher angles is characteristic of the k-alpha doublet based on the degree of separation, although further

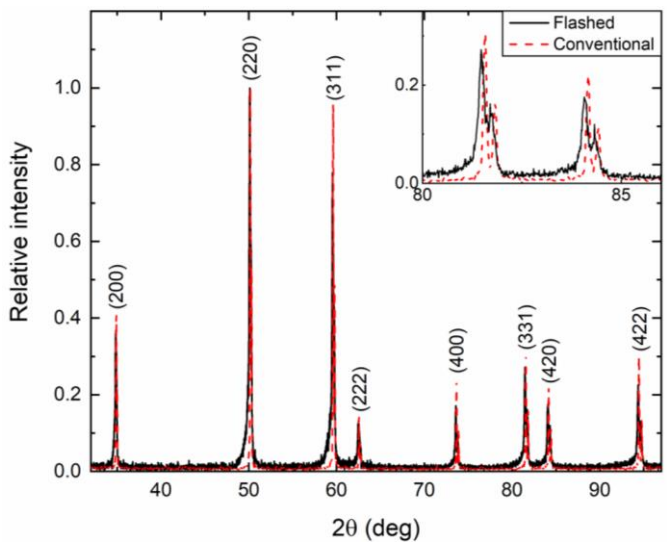

Figure 5.3 θ-2θ scan of a flash sintered sample and a conventionally sintered, furnace cooled sample. Inset shows the same data enhanced to show peak splitting. Both spectra are normalized by the (220) peak intensity.

refinement is required to fully confirm the absence of the tetragonal phase. Most notably, there are no reflections absent nor significant differences in intensity which would indicate large-scale texture development, although this lack does not preclude the possibility of local texture.

Figure 5.4 shows a TEM image of the general microstructure of the center of a flash sintered sample. The grain boundaries appear clean of large scale inclusions or secondary phases, although higher resolution analysis would be required to observe very thin wetting layers. Additional TEM analysis is currently underway.

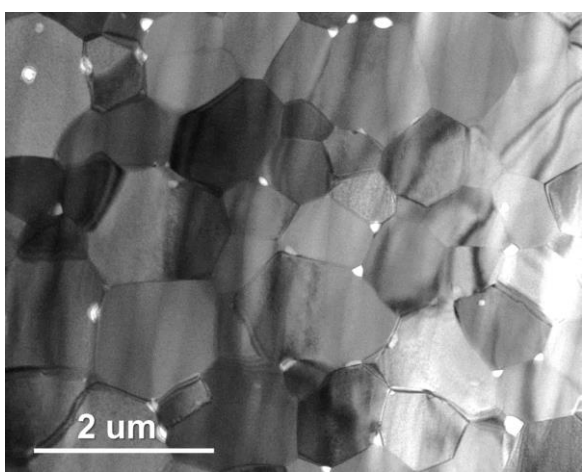

Figure 5.4 TEM image with the microstructure of a flash sintered sample (TEM courtesy of Steven Funni).

5.4 Possible sources of enhanced grain boundary conductivity

Although analysis of these samples is ongoing, this experimental set provides data for some preliminary discussion of the possible explanations for enhanced grain boundary conductivity in flash sintered YSZ.

The first possibility suggested was texturing, either globally or locally. This would increase the grain boundary conductivity if the preferred orientation increased oxygen vacancy mobility across the boundary (*2*). Although far from definitive, the spectra in Figure 5.3 do not show any indication of large-scale texture. Extensive EBSD would be required to identify statistically significant local texturing; it does appear from this preliminary data that any texturing effects would have to be subtle.The second possibility was that the conductivity was influenced by the presence or distribution of a secondary siliceous phases at the grain boundary. Impurities in YSZ powder commonly form a silica-based secondary phase at grain boundaries which, although not contiguous, does cause current constriction, reducing the grain boundary conductivity overall on a geometric basis (*4, 171*). Some studies indicate that this phase redistributes to surfaces and triple junctions upon annealing (*175, 176*). This type of redistribution has also been suggested to explain the increase in grain boundary conductivity observed upon rapid cooling (*165, 172*), although direct empirical evidence linking the quench effect to secondary phases is unreported.

The preliminary TEM imaging of the center of the flash sintered sample does not show any secondary phase, which may be due to the relatively high purity of the powder (< 0.002 wt% SiO_2), to re-distribution to regions outside of the sample center, to sampling limitations, or to the relatively low imaging magnification. In fact, Figure 5.4 shows a significant number of triple junction pores, but it is unclear whether these were pores in the as-processed sample or locations

which suffered grain pullout during sample preparation. If silica redistributed to these sites, it may have weakened the grain boundary, exacerbating pullout, and would no longer be evidenced in the sample. More imaging of flashed and conventionally prepared samples is required to identify the presence of a siliceous phase or lack thereof, but it is notable that this effect would be retained during the post-anneal and is therefore a viable candidate for the retained conductivity enhancement in the quenched and flash sintered sample.

The third possibility was the retention of a high temperature grain boundary complexion, manifest structurally or chemically, in the flash sintered and quenched samples which would correspond to a higher grain boundary conductivity. The temperature dependence of grain boundary complexions in YSZ has not been reported yet to our knowledge, but discontinuous changes in properties are considered indicative of a complexion transition (*173*). This effect would be removed by post-annealing, because all of the annealed samples saw the same high temperature and the same cooling profile, and like a phase, the grain boundary complexion should be responsive to changes in temperature. Therefore, at most the complexion could be responsible for the non-permanent component of the conductivity increase evidenced in Figure 5.2b. Figure 5.4 does not depict any notable or unusual structural characteristics, such as faceting or interfacial disorder, but definitively disproving this prospect is not possible without a comparison to the conventionally sintered sample and higher resolution imaging.

Finally, the difference in conductivity between the flash and conventional samples before annealing could be due to the difference in grain size. As grain size decreases, solute segregation to the grain boundary depletes the bulk, which becomes significant when the bulk concentration is significantly decreased. Alternately, when the size of the space charge, correlated to the depletion region, becomes large relative to the grain size, overlap between space charge layers

alters the electrostatics of the layers. Although this effect is often ignored in grains outside of the nanoscale, Verkerk et al. reported a decrease in specific grain boundary conductivity with increasing grain size in grains larger than 2-4 um in 8YSZ; they measured the effect up to grains as large as 12 um (*165*). Guo & Zhang reported the same effect in 3YSZ, although they observed it in grains smaller than 2 um as well, and proposed an increase in space charge with grain size to explain it (*177*).

A direct comparison of absolute conductivity values to these literature results is difficult because the measurement temperatures were different, but this microstructural influence on space charge and dopant segregation could be responsible for the non-permanent increase in grain boundary. Note that the high-temperature anneal would produce substantial grain growth, which would reduce the difference in grain size and therefore conductivity between the flash sintered and conventional samples. Additional TEM analysis, including EDS, in currently underway to identify directly whether modification to the dopant profile and therefore space charge has occurred in the flash sintered samples.

5.5 Conclusions

In order to better understand the origins of the specific grain boundary conductivity increase in flash sintered YSZ, flash sintered and two types of conventionally sintered samples were subject to a high temperature anneal. After annealing, the bulk conductivities returned to the same value, but the flash sintered and conventional+quenched samples retained a higher grain boundary conductivity. Additional analysis, including XRD and TEM, was performed, and the results were discussed in the context of four possible reasons underlying the conductivity trend: texture, silica redistribution, high temperature complexion retention, and modified dopant

segregation. This work is still ongoing, and at this time there is not enough evidence to strongly support one theory over the other.

CHAPTER 6

Effect of Processing Frequency during AC Flash Sintering

6.1 Introduction and background

Among the flash sintering literature, comparatively few studies have utilized AC instead of DC fields, and fewer still have examined the effects of the specific frequency chosen. Muccillo & Muccillo (*28*) and Steil et al. (*29*) were among the first to implement AC in flash sintering in 2013. Since then, AC flash sintering has been used to mitigate electrochemical reduction (*76, 80*) and mechanical instabilities (*41*). Yet, to our knowledge, the only study examining the effect of different frequencies on flash sintering was published by Carvalho et al. in 2018, in which 3YSZ was flash sintered at frequencies from 0.5 to 1 kHz (*36*). Carvalho et al. reported that higher frequencies produced higher density samples and less resistive final samples; they suggested that more Joule heating was produced at higher frequencies, aiding densification and increasing conductivity. While impedance and therefore AC Joule heating are frequency dependent, significant variation in heat dissipation over less than one decade seems surprising and perhaps unlikely.

This chapter postulates that the effect of frequency during flash sintering should depend, to a first approximation, on where the processing frequency falls relative to the characteristic impedance response of the starting green body. For a given temperature and frequency, different

dielectric polarization mechanisms are active. The manifestation of these mechanisms in various electrical parameters is depicted in Figure 6.1 for a polycrystal with one type of charge carrier and three dielectric contributions: one at the electrode/sample interface, one at the grain boundary, and one within the sample bulk. At the lowest frequencies, $f < f_{elec,store}$, all polarization mechanisms are able to respond because the field switches slowly relative to the polarization response times. As the frequency increases, two physically significant frequencies are reached: $f_{elec,store}$, which corresponds to the maximum frequency at which maximum charge storage is attainable at the electrode/sample interface; and $f_{elec,loss}$, which corresponds to the frequency at which the field most efficiently couples with the loss mechanism at the interface, generating

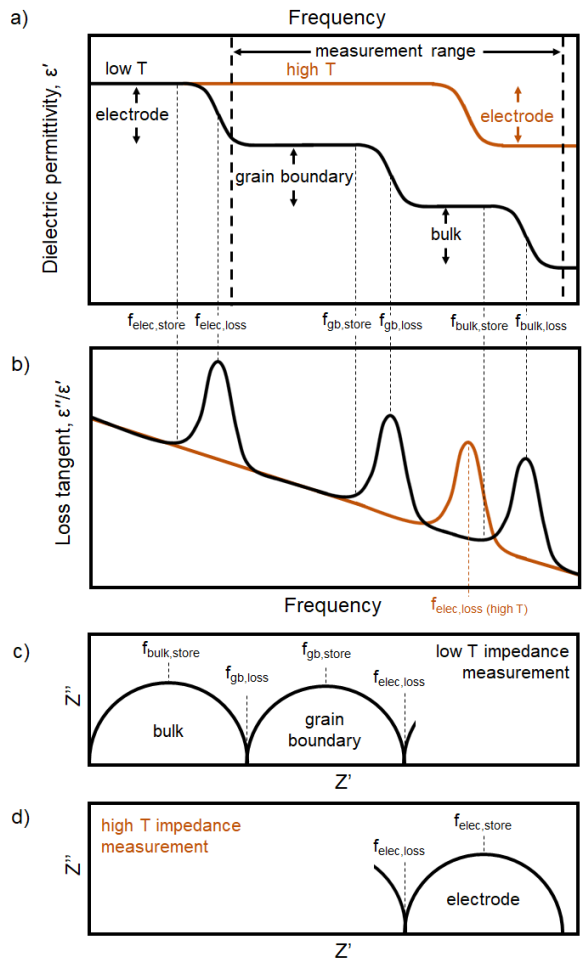

Figure 6.1 Schematic depicting the standard frequency dependence of a) dielectric permittivity and b) the loss tangent at two different temperatures. c) depicts the way these parameters manifest in an impedance spectrum recorded with a fixed frequency range at low temperature and d) at high temperatures.

maximum loss from that mechanism. The point $f_{elec,loss}$ manifests as a peak in the loss tangent (Figure 6.1b) and as a local minimum in a complex impedance plot (Figure 6.1c), while $f_{elec,store}$ indicates a local maxima on the complex impedance plot. As the frequency increases, the next slowest mechanism manifests its storage maximum, $f_{gb,store}$ in this example. At some intermediate frequency ($f_{elec,loss} < f < f_{gb,store}$), the electrode/sample interface mechanism stops contributing to the dielectric response of the sample, as the switching frequency has exceeded the ability of the mechanism to respond. This effect is important, but does not correspond to a clear single frequency in experimental plots. If the frequency continues to increase, each mechanism manifests its own maximum in storage and loss, first the grain boundary and then the bulk. Again, within the frequency range $f_{gb,loss} < f < f_{bulk,store}$ the grain boundary becomes unable to respond, and within $f_{bulk,loss} < f < \infty$ the bulk becomes unresponsive as well.

The simple depiction of dielectric response can be complicated by multiple polarization mechanisms with similar time constants or may be effected by the amplitude of the AC field and any superimposed DC field. Significant deviations from the idealized spectrum in Figure 6.1 can be produced by, e.g. non-linear electrode responses. In fact, as discussed later, the YSZ/Pt system does ultimately represent a more complex picture that that presented above.

Using the simplified framework in Figure 6.1 as a first approximation, we hypothesize that frequencies below, at, or above specific characteristic loss frequencies will result in different thermal and sintering profiles during flash. Theoretically, heat dissipation would be increased by choosing a frequency which corresponds to one of the loss peaks, e.g. $f_{elec,loss}$. Alternately, choosing a frequency above which one or more mechanisms is no longer active would reduce the heat generated but, by delocalizing the heat dissipation away from grain boundaries or interfaces, could lead to greater sample homogeneity.

This chapter reports the results of a set of experiments testing this hypothesis. First, the important frequencies and corresponding mechanisms of a YSZ green body at high temperatures were established. Next, a set of samples were flash sintered using the AC flash sintering equipment at NCSU, holding all flash sintering parameters constant except for the frequency in order to confirm that final properties are independent of frequencies below the lowest theoretically significant frequency value (e.g. $f_{loss,elec}$). These experiments used frequencies ranging from 0.1 to 9 kHz were used. In the second set of experiments, the AC flash sintering facility at Lucideon was used to test two higher frequencies (15 and 1500 kHz) which were below and above the lowest significant frequency previously established.

6.2 Green body characterization

In order to test the hypothesis that flash sintering at frequencies above and below specific characteristic frequencies would produce different sintering profiles, first the relevant frequency values needed to be established for YSZ in the green body state to determine which mechanistic transition or coupling values which would be accessible during flash sintering based on the range of frequencies available. Because the dielectric response is highly temperature dependent, the characteristic frequencies are temperature dependent too; this is shown in Figure 6.1a as a shift in the spectra to higher frequencies. Thus the same frequency window records different mechanisms depending on the sample temperature (Figure 6.1c and d). In the relatively low-temperature impedance measurements reported in this dissertation so far (290-370°C), the frequency range available to the impedance spectrometer (5 Hz-5 MHz) captured the bulk and grain boundary response, and the very beginnings of the electrode response. Values for $f_{elec,loss}$, $f_{gb,store}$, $f_{gb,loss}$, and $f_{bulk,store}$ can be extracted from this type of measurement at each temperature

measured between 290 to 370°C. Note that the $f_{i,store}$ is related to the resistance (R_i) and capacitance (C_i) according to Eq. 6.1:

$$f_{i,store} = \frac{1}{\tau_{char}} = \frac{1}{2\pi R_i C_i} \tag{6.1}$$

where τ_{char} is the time constant of the equivalent circuit element.

Using the impedance spectra previously reported in §4.3.4 from a conventionally sintered these frequency values from the previously reported spectra against inverse temperature (Figure 6.2). Assuming an Arrhenius response up to higher temperature, we extrapolated these values up to the furnace temperature of 1020°C. The predominantly bulk and grain boundary mechanisms which usually characterize the YSZ spectra respond at too high a frequency to manifest in an impedance measurement at flash sintering temperatures. One possible exception to this was the electrode loss impedance minimum ($f_{elec,loss}$), which bordered the measurable region. This analysis indicated that, while the electrode, grain boundary and bulk polarization mechanisms would all be active during any measurements or processing at high temperatures within our accessible range, either coupling with the bulk or grain boundary mechanisms ($f = f_{gb,loss}$) or short-circuiting their contribution (requiring $f > f_{gb,loss}$) would not be possible. Thus any

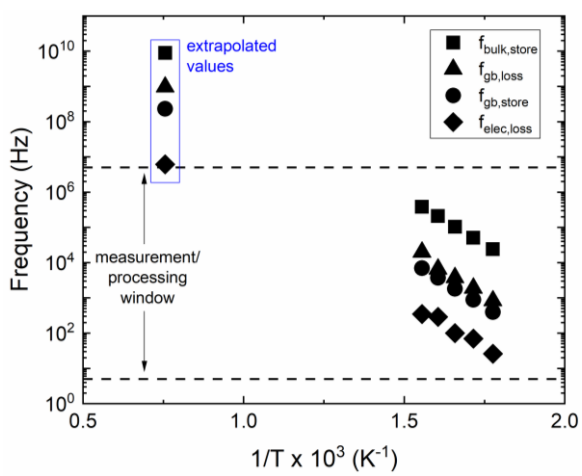

Figure 6.2 Characteristic frequencies extracted from the equivalent circuit fitting of the impedance spectra of a conventionally sintered YSZ sample.

frequency dependent behavior below the 100 Hz to 3 MHz range must depend on the impedance response of the electrode.

In order to elucidate the frequency dependent dielectric behavior of a porous green body and to establish the electrode behavior at high temperatures, impedance spectra were recorded over a broader range of temperatures using the sample holder in the AC flash sintering system at NCSU (system details can be found in §2.2). These measurements were performed on a green body, rather than a dense sample, in order to mimic the starting condition of flash sintering samples, and the green body sample was prepared the same way as the flash sintering samples in Chapter 4. The measurements, spanning ~360 to 918°C, are shown in Figure 6.4c-j, along with a comparison to the dense body spectra at 370°C (Figure 6.4a and b). The significant frequency values pulled from the spectra are plotted in Figure 6.3 and compared with the dense body values.

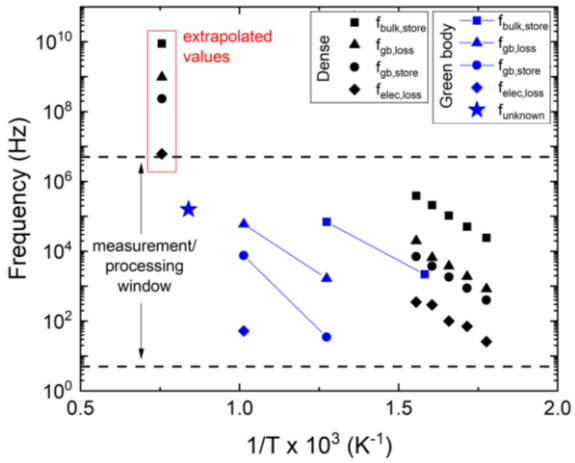

Figure 6.3 Characteristic frequencies extracted from the equivalent circuit fitting of the impedance spectra of a YSZ green body (blue) plotted with the characteristic frequencies of a dense sample (black). The blue lines are included only as a visual guide.

Table 6.1 Capacitance values extracted from equivalent circuit fitting of the high temperature impedance spectra.

T (C)	Bulk capacitance (F)	Grain boundary/particle surface capacitance (F)
[redacted]		

The impedance response of the green body is significantly different than the dense samples. Although the magnitude of the impedance, and therefore the characteristic frequency values, are substantially higher in the green sample than the dense sample, the relative contribution of each element can be assigned by the capacitance values, extracted from equivalent circuit fitting and shown in **Table 6.1**. These values indicate that the 359ºC spectrum captures the bulk impedance, the 512ºC spectrum captures the bulk and particle contact/surface contribution, and the 714ºC spectrum captures a portion of the bulk, all of the particle contact, and the beginnings of the electrode contribution. The shift in mechanisms captured with increasing temperature allows confident assignment of the highest temperature behavior (918ºC spectrum) to the electrode/sample interface, as the bulk and grain boundary contributions clearly move out of the measurable frequency range with increasing temperature. The significant frequency values plotted in Figure 6.3 further confirm that bulk or grain boundary coupling is inaccessible at high temperatures.

Next, it is notable that the highest temperature data introduces an apparent inductive element to the electrode/sample interface characteristics. The data were tested for lead inductance following the procedure described in §2.4, which verifies that the apparent inductive behavior in Figure 6.4i originates from the sample as opposed to being a measurement artifact. Note that the presence of the inductive element produces a discontinuity in ε' and ε'', which complicates the specific mechanistic interpretation of the contribution. The physical origins of this component and possible meanings for its characteristic frequency, $f_{unknown}$, are therefore discussed in detail later. Regardless of its precise mechanistic origins, the frequency $f_{unknown}$

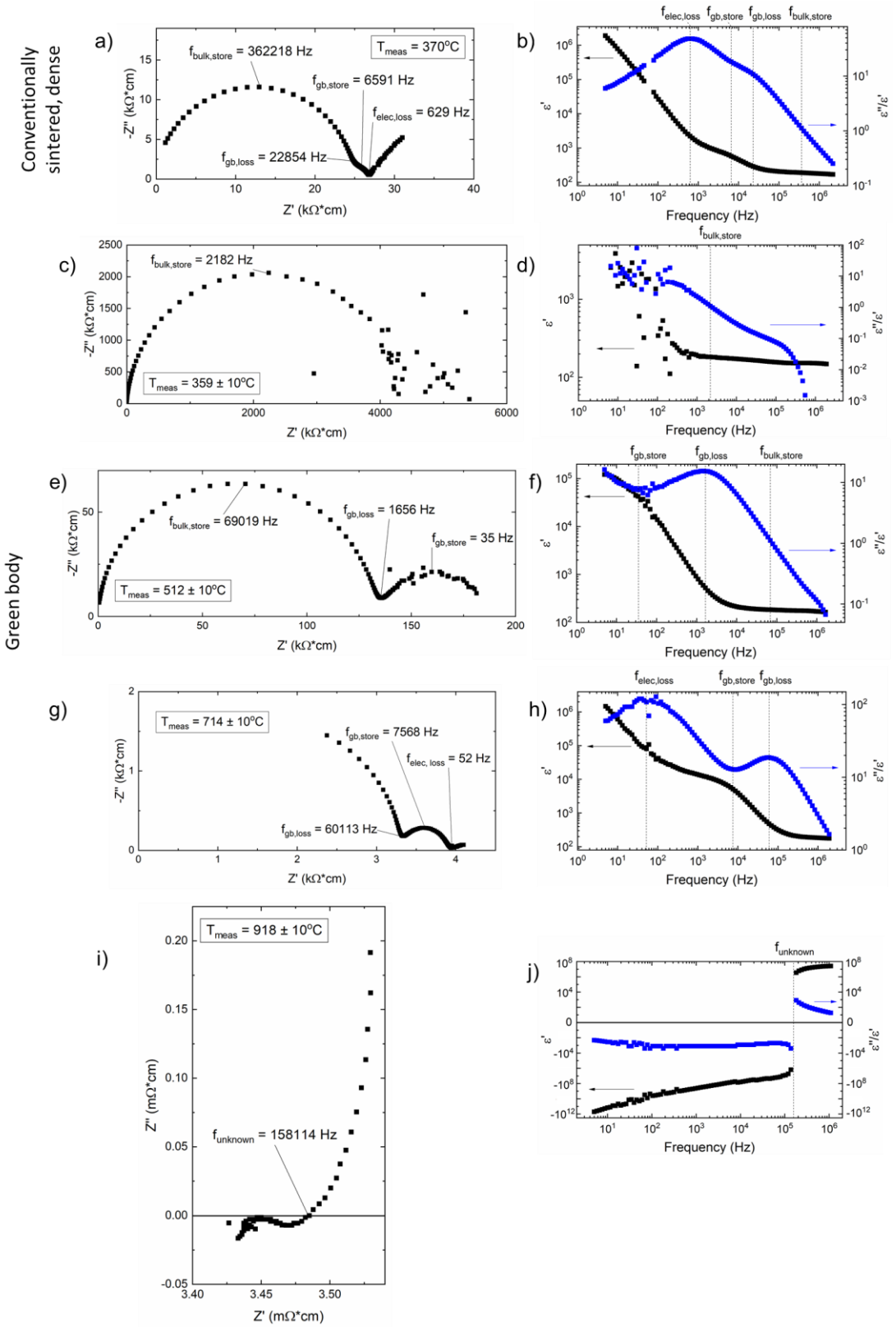

Figure 6.4 Impedance spectra of a green body measured at several temperatures. As the temperature increases, slower conduction/polarization mechanisms can be measured.

(~160 kHz) represents a transition in the impedance spectra between an inductive and capacitive element; this means that, at 1020°C, the mechanism representing the inductive element does not respond to frequencies greater than ~160 kHz. Therefore, based on our hypothesis, processing above and below this frequency may manifest some difference in the dielectric response and therefore sintering behavior of the sample.

6.3 Low frequency sintering (0.1 - 10 kHz)

6.3.1 Methods

Flash sintering experiments were performed in the lower frequency range (0.1-10 kHz) using the AC flash sintering setup described in §2.2. Pellets were prepared following the procedure used in the experiments in Chapter 4. The furnace temperature was 1050°C, corresponding to a starting sample temperature of ~1020°C, and a current ramp rate of 6x10^{-5} A/ms was used to initiate flash with a maximum current of 3 A (10.6 A/cm^{2}) and 30 s hold time. Frequencies of 100, 500, 1000, 5000, and 9000 Hz were used.

After flash sintering, residual Pt paste was removed from the sample surfaces in order to perform Archimedes density measurements. The surfaces were then polished and Pt electrodes were sputtered for ex situ impedance measurements. These measurements were performed from 290 to 370°C using an HP4192A impedance spectrometer; equivalent circuit fitting was performed using EIS Spectrum Analyser software (*108*) to fit the spectra to a two R||C element circuit. The brick layer model was used to normalize grain boundary conductivities (see §2.4). Next the samples were cross-sectioned, mounted, polished, and coated with AuPd for microstructure imaging. The microstructures were characterized using ion channeling contrast imaging on an FEI Quanta 3D FEG, a technique which does not require thermal annealing to

relieve grain boundaries. Grain size measurements were performed using the linear intercept method and Mendelson's correction factor of 1.56 was applied (*148*).

6.3.2 Low frequency results

The Archimedes densities of the samples processed from 0.1 to 9 kHz are shown in Figure 6.5 and the in-situ surface temperatures of the 0.1, 1, and 9 kHz samples are reported in Figure 6.6. Microstructure images from the center of the samples are shown in Figure 6.7a-c and grain sizes are plotted as a function of frequency in Figure 6.7d. The edge and electrode regions of the samples exhibited the same degree of grain size inhomogeneity as observed in the experiments in Chapter 4; these values are included in Figure 6.7d. Data processed with similar ramp rates are included to demonstrate that the variation with respect to frequency falls within experimental scatter. Neither density nor grain size appeared to trend in any significant way with

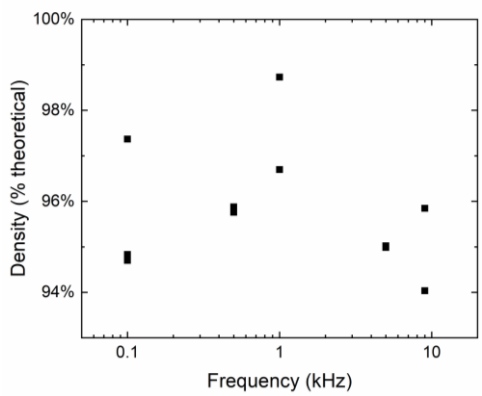

Figure 6.5 Archimedes density measurements for samples processed at 0.1-9 kHz. A maximum current of 3 A was used with a current ramp rate of $6x10^{-5}$ A/ms for all samples.

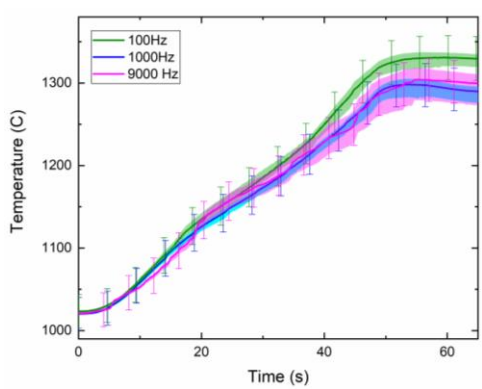

Figure 6.6 IR temperature profiles over time for samples processes at 100, 1000, and 9000 Hz.

frequency within this range; the degree of scatter in the density data likely results from the choice of a sub-optimal ramp rate.

While the invariance of microstructural properties with frequencies in this range does contradict the earlier results reported by Carvahlo et al. (*36*), these results agree with our characteristic frequencies hypothesis. Even the highest frequency, 9 kHz, was substantially lower than the ~160 kHz value of interest identified in §6.2. The results discussed in Chapter 4 indicate that the thermal profile of the sample should determine the microstructural properties. The IR surface temperature profiles behaved roughly same way in response to time and current regardless of frequency and produced roughly equivalent final products. This profile also disagrees with the frequency-temperature mechanism proposed in the Carvalho study, as the surface temperature appears independent of frequency in this range.

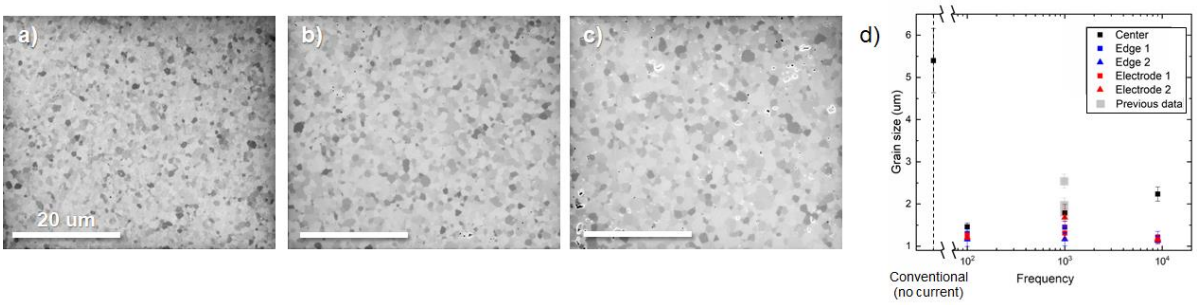

Figure 6.7 Microstructure images from the center of samples processed at (a) 100 Hz, (b) 1000Hz, and (c) 9000 Hz. (d) Grain size plotted as a function of frequency; grain size from a conventionally sintered sample is included for comparison, along with data from other samples with similar ramp rates (gray squares) to depict the general degree of variability.

6.4 High frequency sintering (1 kHz - 1.5 MHz)

6.4.1 Methods

In order to expand the range of frequencies tested, the second set of experiments was performed using the facility at Lucideon, Stoke-on-Trent. Due to the change in equipment, there were a few notable differences between the experimental setups for the low and high frequency experiments, although the pellets used were prepared the same way as in the NCSU experiments.

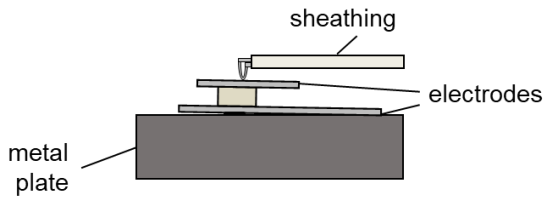

Figure 6.8 High frequency experimental setup.

First, a different sample holder was used, shown in Figure 6.8, which included a metallic bottom plate rather than a ceramic one; this introduced more asymmetric thermal boundaries. Second, two different power supplies and controls systems were utilized at this facility. The first was identical to those used in the NCSU experiments; experiments with that system used a current ramp rate of $6x10^{-6}$ A/ms, and the current was allowed to increase up to a power of 50 W, which corresponded to ~3.5 A. This system, like the one at NCSU, was limited to 10 kHz and was only used to generate an overlapping set of comparison samples at 1 kHz. The second electrical system, which included a higher frequency power supply, used power as its control parameter rather than current. A power ramp rate of $6x10^{-5}$ W/ms was chosen to approximate the current ramp rate of $6x10^{-6}$ A/ms. The power values and processing frequencies used in this set of experiments are shown in **Table 6.2**. Two samples were processed at each condition except for the 20W samples, due to time-limited access to the equipment. For clarity, all samples processed at this facility (including both the 1 kHz comparison samples and the 15/1500 kHz samples) are referred to as "Lucideon" samples in the following discussion, in comparison to "NCSU" samples processed between 0.1 and 9 kHz.

Table 6.2 Processing parameters used for high frequency flash sintering experiments.

Processing frequency (kHz):	1	15	1500
Max power (W)	-	20	20
	-	35	35
	50	50	50

An additional difference between the NCSU and Lucideon experiments was the pre-flash heating profile. In the Lucideon experiments, three samples were loaded simultaneously into the furnace at room temperature and the furnace was heated at a rate of 300°C/h up to 1020°C to match the starting temperature of the samples in the NCSU experiments. After 1020°C was reached, a baseline in-situ impedance spectrum was measured of one of the green bodies using a Solartron 1260; the spectrum from a typical green body in the Lucideon system is shown in Figure 6.9. These spectra indicated that the frequency of interest, $f_{unknown}$ in Figure 6.4, decreased slightly when switching systems, from ~160 kHz to ~20 kHz; however, the processing frequencies chosen – 15 kHz and 1.5 MHz – still bounded this value on either side, making it a valid test of our hypothesis.

The three samples were then flash sintered one after the other with a brief (< 10 min) delay between each during which the impedance spectrum of the newly flashed sample was measured in situ. After flash sintering and measuring all three samples, the furnace was turned off and the samples cooled down overnight in the furnace. After the samples were removed from the furnace, their densities, microstructures, and low temperature (290–370°C) impedance behaviors were characterized using the same procedure described in §6.4.

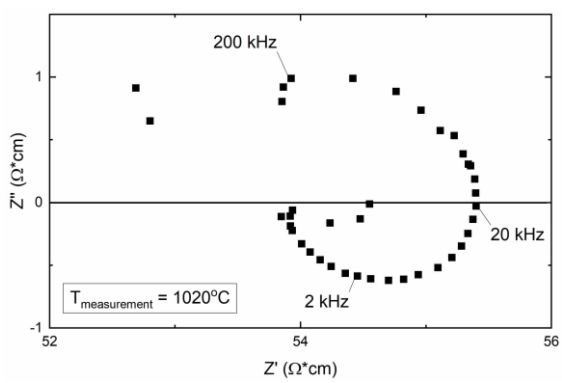

Figure 6.9 Impedance spectrum of a green body at 1020°C in the Lucideon system.

6.4.2 High frequency results

In Figure 6.10, the in-situ impedance spectrum of the green body is compared to the in-situ, post-flash spectra of samples flashed at 15 kHz and 1.5 MHz for various power levels. The characteristic "inductive" loop observed in the spectrum of the green bodies pre-flash disappears after flash sintering at 15 kHz with all but the lowest power; the spectrum instead is characterized by an R||C element. However, the samples flash sintered at 1.5 MHz retain their inductive nature at all power levels. This behavior was highly reproducible among samples processed at these frequencies. As discussed earlier, these results indicate that some mechanism is active below ~20 kHz which is effectively short-circuited by a processing frequency of 1.5 MHz. Note that the densities (included in Figure 6.10) remain independent of processing frequency.

The microstructures from the 50W samples (spectra in Figure 6.10a) are shown in Figure 6.11 for several regions of the sample. The microstructures are inhomogeneous, which complicates the comparison; however, within their inhomogeneity the samples all appear fairly similar. For instance, in each sample there is consistently one electrode with smaller grains than the other, and one edge with consistently larger grains than its counterpart. This distribution is likely due to the different thermal boundary conditions in the Lucideon sample holder; the small grained electrode may have been located next to the sample holder's metal plate (Figure 6.8), which would have cooled that region of the sample substantially, and the larger grained edge was likely located under the horizontal sheath from the top electrode, which could have preferentially concentrated current on that side due to reduced contact resistance. Finally, ex-situ values for bulk and grain boundary conductivity at 330°C are shown in Figure 6.12a and b as a function of processing frequency, compiled from both the NCSU and Lucideon samples. Note that these

spectra were collected in post-processing, so the original Pt/YSZ interface was removed, and new Pt was deposited. The data appear generally invariant with respect to frequency. The conductivity of the NCSU samples is fairly constant and consistent with the values reported in Chapter 4. The values for the Lucideon samples (σ_{gb} in particular) appear quite scattered; this difference may be due to the greater degree of microstructural homogeneity – the brick layer model assumes a homogeneous grain size – and the better control of the thermal profile in the

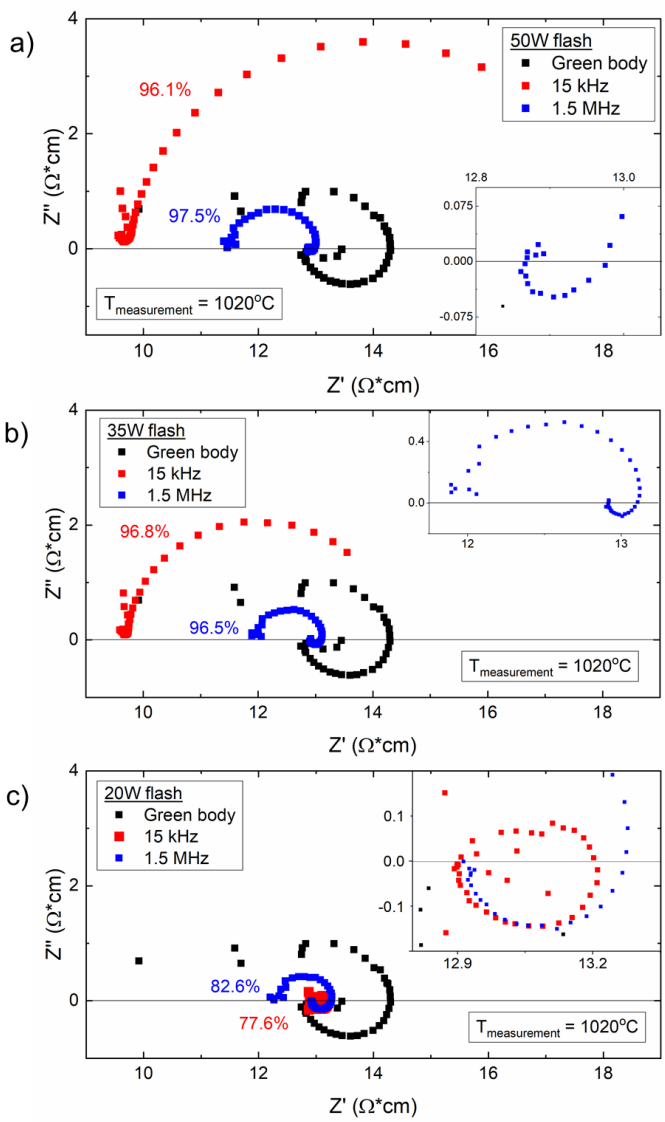

Figure 6.10 Post-flash impedance spectra collected immediately after processing (T = 1020°C) and compared to the green body spectra. Red samples were flashed with 15 kHz while the blue samples were flashed with 1.5 MHz. Final power values of (a) 50 W, (b) 35 W, and (c) 20 W were used. Spectra are labelled with their final densities. Some spectra were shifted along Z' to allow for easier plotting and comparison and insets were included to magnify the details of certain spectra.

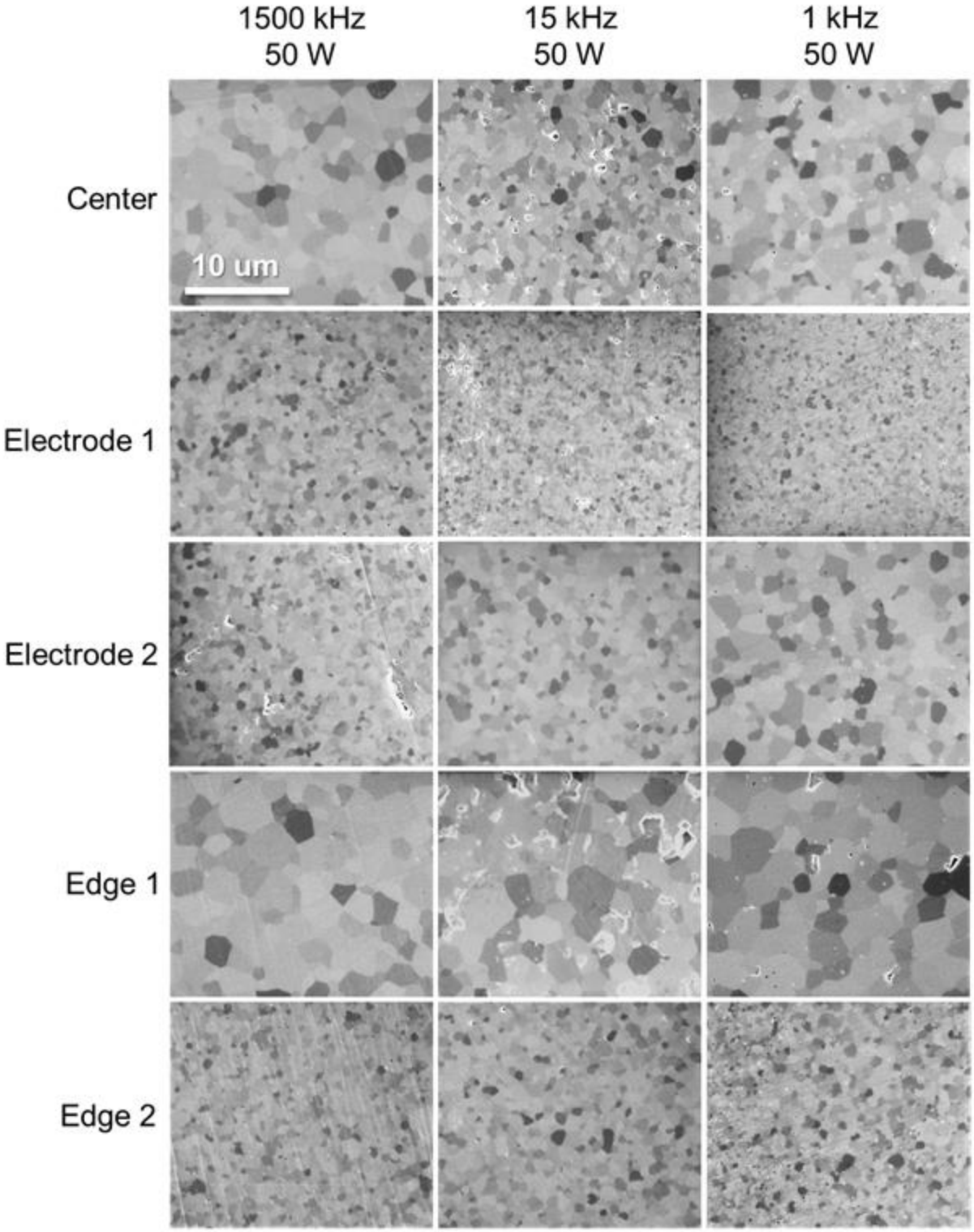

Figure 6.11 Spatial distribution of microstructures for samples processed at 50W and 1, 15, and 1500 kHz.

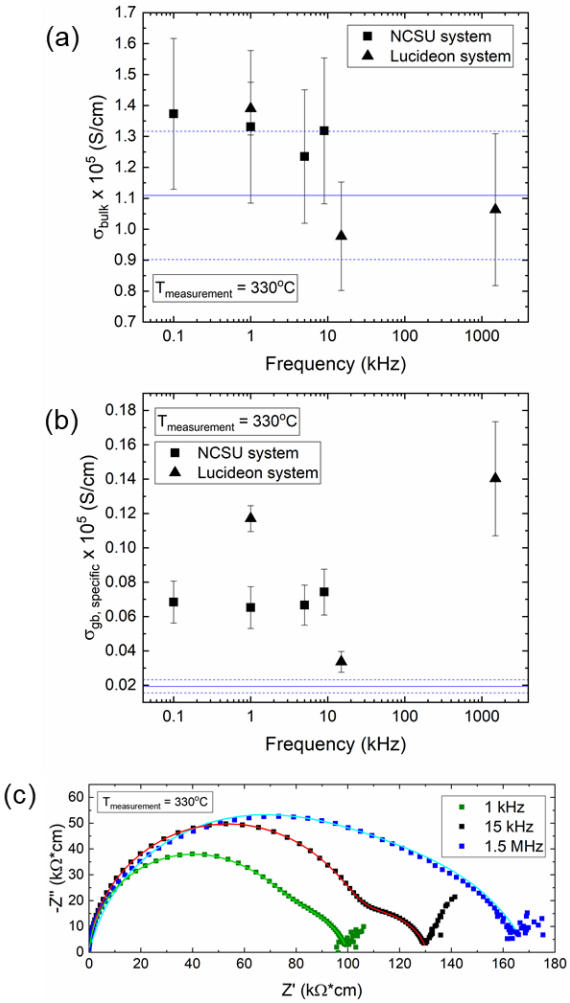

Figure 6.12 (a) Bulk and (b) grain boundary conductivities shown as a function of frequency. (c) shows the Nyquist plot for the 1, 15, and 1500 kHz Lucideon samples at 330ºC with their respective equivalent circuit fits. The Lucideon samples were all processed with 50W.

NCSU samples. The Lucideon samples also experienced variable amounts of time in the furnace because the samples were run in sets of three.

The most notable features in the ex-situ electrical data include the persistent increase in grain boundary conductivity as compared to the conventionally sintered sample and the elevated bulk conductivity among the NCSU samples relative to the Lucideon samples. Both of these findings are consistent with those in Chapter 4 and likely grounded in the same causes; the bulk conductivity is sensitive to thermal profile, and the source of the grain boundary conductivity increase is still under investigation. The measurement most likely to exhibit different behavior –

that of a sample processed at 1.5 MHz – did appear to have the highest grain boundary conductivity. However, that may have been due to issues with fit quality; the spectra from that sample were difficult to fit, as exemplified in Figure 6.12c. The data are shown compared to the 15 kHz sample, in which the features were much better defined and produced a much more satisfactory fit.

6.5 Discussion: Interpreting changes in interfacial behavior

By far the most interesting result from the frequency experiments was the change in the in-situ impedance behavior after flash when processing at and below 15 kHz, and retention of the same qualitative spectrum as the green body after processing at 1.5 MHz. As established in §6.2, these high temperature impedance features describe the electrical character of the electrode/sample interface; therefore, these before and after spectra indicate some change in the interfacial response in only the lower frequency-processed samples.

Physically, an inductor typically represents energy storage via the generation of a magnetic field. However, when inductive behavior is reported in a non-magnetic material, and particularly in electrolytes, it is often explained using interfacial reactions. From a mathematical perspective, Klotz has explained inductive loops in this type of material as a superposition of time varying responses (*178*). When some aspect of the circuit changes in response to the measurement – e.g., a conductivity increase in response to a voltage pulse – the change introduces an impedance maxima in the time domain, which translates to a current lag or positive phase shift, the mathematical form of an inductor. In this study therefore, the inductive loop implies that the electrical characteristics of the Pt/YSZ interface change in response to the impedance measurement itself.

To make sense of possible interfacial changes in YSZ, consider the time varying response of one electrode/YSZ interface to an electric field. Under a positive driving voltage, the following reaction occurs at the triple phase boundary:

$$O_o^x \overset{k_{forward}}{} V_o^{\cdot\cdot} + O_{ads} + 2e^- \tag{6.2}$$

The reverse occurs under a negative driving voltage:

$$V_o^{\cdot\cdot} + O_{ads} + 2e^- \overset{k_{reverse}}{} O_o^x \tag{6.3}$$

Often, the rate of Reaction 6.3 is less than the rate of Reaction 6.2 because $[O_{ads}]$ is not replenished as quickly as oxygen vacancies arrive, i.e. $J_{O_{ads}} < J_{V_o^{\cdot\cdot}}$ (see Chapter 3 for a discussion of the empirical factors which can limit the flux of O_{ads}). When this occurs, the local stoichiometry of the interface changes, becoming slightly reduced and producing a decrease in resistance.

Now consider the driving voltage during an impedance measurement, Figure 6.13a. When the electrode/sample interface is subject to a negative driving voltage, oxygen vacancies are driven to the interface. For very small voltages, the amount of O_{ads} at the surface is adequate to facilitate Reaction 6.3, but once this reservoir is depleted the reaction begins to lag, and oxygen vacancies accumulate at the interface; this point is shown in Figure 6.13b as t_1 in excess oxygen vacancy concentration profile. The resulting change in local stoichiometry produces a local drop in resistance which varies with time and voltage (right axis of Figure 6.13b). Therefore, the current maximum of the sample response will occur not at the voltage maximum, but when the absolute ratio of the voltage to the resistance is maximized, t_2 in Figure 6.13a. This lag in current response characterizes the classic inductor (in which the ideal current phase shift would be 90°). This situation also fits the time-varying conditions Klotz describes as producing

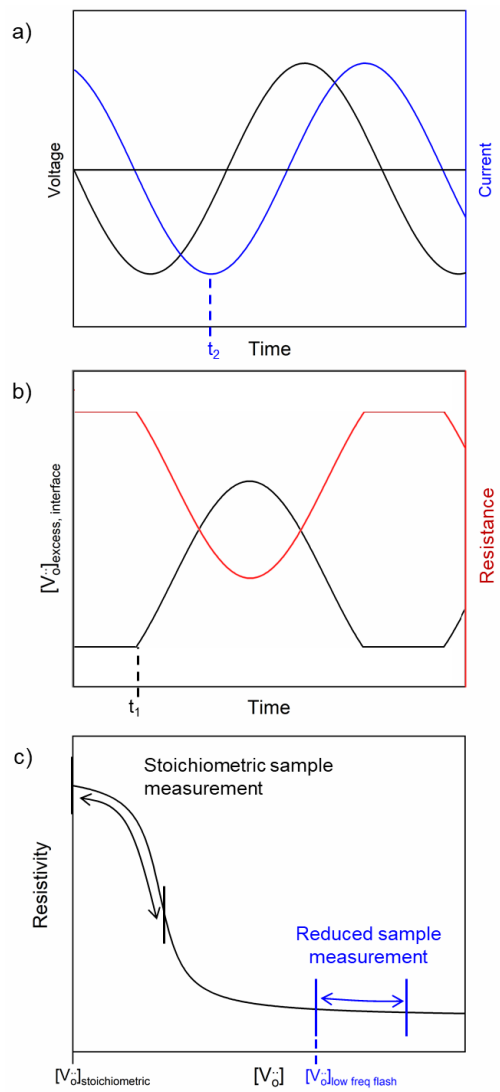

Figure 6.13 Time varying response during AC excitation of (a) voltage and current and (b) $[V_O^{\cdot\cdot}]_{excess}$ and resistance. (c) shows a schematic of the sensitivity of resistivity to oxygen vacancy concentration for a YSZ-type material.

inductive impedance loops (*178*), and explains why the green body spectrum of YSZ behaved inductively.

Given that the sensitivity of the interfacial resistance to local deviations in stoichiometry produces an inductive effect in impedance spectra, the absence of the inductive loop indicates that the interfacial resistance is relatively invariant in response to the driving voltage. This type of capacitive response was found in the in-situ, post-flash spectra of samples flashed at frequencies below 1.5 MHz (Figure 6.10). We suggest that the difference between the low and

high frequency flashed samples is found in the accumulation of oxygen vacancies which is possible under high currents and low frequencies. During an impedance measurement, when the starting condition of a sample is stoichiometric, small perturbations in oxygen vacancy concentration produce large changes in the resistance, as depicted in Figure 6.13c. However, when the interface of the sample is already reduced, perturbations in stoichiometry have relatively little effect on the resistance.

Our results indicate that high frequencies (≥ 1.5 MHz) limit the amount of reduction that occurs at the interface. In addition, there appears to be a power dependence; the 15 kHz sample flashed at the lowest power value (20 W) maintained its inductive character. These trends all agree with the picture of oxygen vacancy accumulation: high frequencies do not allow as much time per cycle for the vacancies to accumulate; and lower powers correspond to lower currents which means the ratio of adsorbed oxygen to oxygen vacancies is larger, limiting the creation of excess vacancies.

Note that while reduction is often assumed to be completely eliminated by switching from DC to AC flash sintering, our lab consistently observes light discoloration indicative of localized reduction upon removing the Pt paste after AC flash sintering; an example of this coloration is shown in Figure 6.14. While the use of AC does prevent large-scale reduction, it does not appear to prevent local reduction at the electrode at low frequencies. Unfortunately,

Figure 6.14 Coloration in 1 kHz flash sintered YSZ.

pictures were not taken of the sub-Pt YSZ surface of the Lucideon samples; however, anecdotally the coloration seemed less severe in the higher frequency samples.

In order to test this theory, impedance spectra were collected at 1020°C of a conventionally sintered 8YSZ pellet with fired Pt paste electrodes. Under all sampling voltages, ranging from 0.01 to 1 V, the inductive loop was present (Figure 6.15a). When a DC bias was applied, the magnitude of the inductive contribution decreased significantly (Figure 6.15b). This decrease could be due to a steady-state decrease in YSZ resistance under DC bias; the inductive loop corresponds to a parallel L||R circuit element, and therefore the magnitude of the loop scales with both the resistive and inductive element. It could also indicate, though, that the resistance was varying less during the measurement, reducing the inductive contribution. More extensive experiments involving different electrode configurations would likely be required to verify this hypothesis.

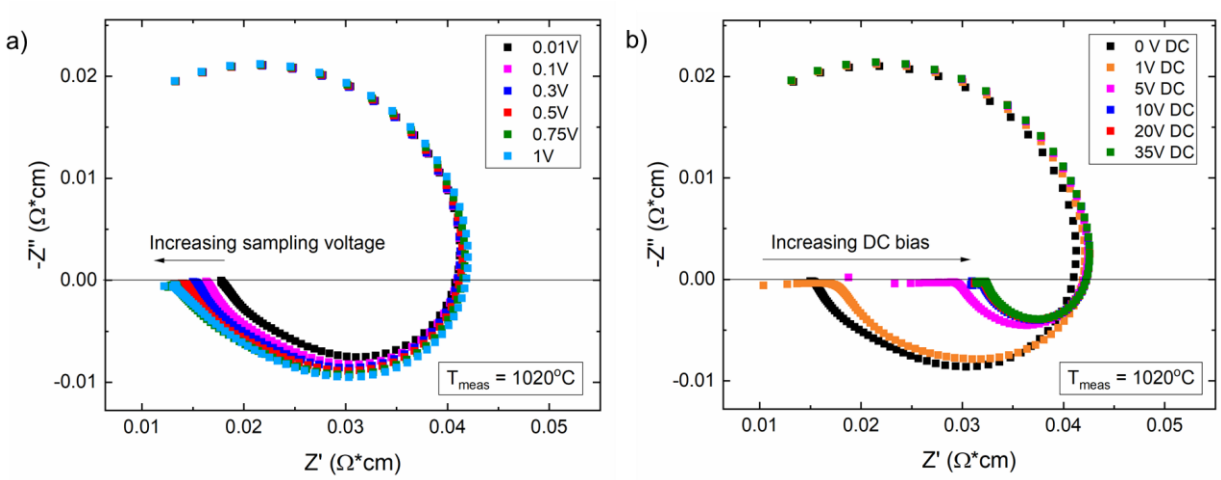

Figure 6.15 Impedance spectra of conventionally sintered 8YSZ at 1020°C (a) with various sampling voltages and (b) under increasing DC bias and 0.3 V sampling voltage.

Finally, it is valuable to contextualize these observations in literature. The time-dependent electrode response characterized here is reported in YSZ literature in a couple of different forms. In high temperature I-V measurements, it manifests as “apparent” hysteresis – that is, not a steady-state hysteresis, but a transient one. This hysteresis is linked to voltage,

sweep rate, and sample history (*117, 179*). Similarly, the same conditions result in inductive loops in impedance measurements (*180, 181*). Generally speaking, this effect is correlated with the overpotential state, which can result from many combinations of electrode microstructure, gas exposure, voltage magnitude (AC or DC) and excitation rate.

6.6 Conclusions

This study used green body impedance spectra to identify frequency ranges which may influence the flash sintering process. Based on these results, two experimental setups were used to examine the effect of frequency on flash sintering across a five-decade frequency range, surpassing the electrode/sample interfacial impedance mechanism at the highest frequency. At the lower frequencies, the similarity in thermal profile appeared to produce samples with similar microstructural and electrical characteristics. In-situ impedance spectra indicated that using a processing frequency below the electrode/interface characteristic frequency fundamentally affected the electrical characteristics of the interface in a manner consistent with an increase in the number of catalytic sites on the surface of YSZ. Processing frequencies greater than the characteristic frequency prevented this change from occurring. Changes in microstructure which might have corresponded to the different interfacial behavior were overshadowed by inhomogeneities introduced by uneven thermal boundaries and current localization. More study is needed to clarify the potential effects on final properties of flash sintering in the MHz range.

CHAPTER 7

Conclusions and Future Work

The studies assembled in this dissertation aimed to decouple the thermal and athermal effects of the electric field during flash sintering, and thereby to elucidate the densification mechanisms of the technique. In literature, early studies did not account for secondary effects like sample temperature, which led to the generation of persistent misleading assumptions, e.g. that Joule heating alone was inadequate to densify ceramics. The most common approach taken to separate the effect of temperature from the direct effects of the electric field has been to add a blocking layer which prevents current flow. This type of athermal study provided an invaluable piece of the puzzle, but because it does not include the same thermal profile as field-assisted sintering techniques, its impact on the sintering process could be, at best, inferred. In this dissertation, we have attempted to maintain all the aspects of flash sintering but, by choosing our parameters carefully and appropriately considering temperature effects, have provided evidence to characterize flash sintering as a predominantly thermal process, understandable using previously established science like stoichiometric reduction and fast-firing. The following chapter summarizes the findings of each of the studies presented, as well as highlighting remaining unanswered questions and areas which seem ripe for additional exploration.

7.1 Electrochemically-induced inhomogeneities in DC flash sintering

In Chapter 3, a study was presented in which the electrochemical boundary conditions of a YSZ pellet were varied during DC flash sintering. This variation was accomplished by using

two different conductive pastes and electrodes, progressively increasing the length of the triple phase boundary facilitating the oxidation/reduction reaction at the anode/cathode of YSZ. The amount of current and lengths of time applied to the samples were also varied.

Substantial stoichiometric reduction was clearly evident from coloration changes and progression into the samples. The amount of reduction scaled with the balance between the degree of ion-blocking enforced by the electrode configuration and sample form factor, and the amount of current involved in the cathodic reaction. The stoichiometry gradient which developed in response to reducing conditions manifested as a density gradient due to the low background temperature, where densification was limited primarily to the anode and the cathode remained virtually green. This densification inhomogeneity was linked to the chemical reduction gradient by the disparate electrical properties of the stoichiometric and reduced ceramic. Reduced YSZ is substantially more conductive, and thus generated substantially less Joule heating, leading to a thermal profile in which the anode was notably hotter than the cathode. The relationship between the degree of reduction and experimental factors like electrode configuration and sample form factor had severe implications for the larger scale implementation of flash sintering, limiting the sample quality attainable for non-ideal form factors.

DC flash sintering is by far the most common form applied in literature; however, this work showed that there were unavoidable detriments associated with the choice of a DC field, particularly in ceramics that are or can, under field, become mixed conductors and in form factors which are not dogbones. Other literature has reported similar inhomogeneities, as discussed in Chapter 1, although when this study was conducted, this concept had not achieved the broad support it has now among the community. As the field of flash sintering progresses, DC remains useful primarily as a way to intentionally induce polarization or reduction and study

the subsequent effects; its value when investigating the fundamentals of flash or trying to achieve certain microstructures and properties is highly limited as the effects from DC become a hindrance which one must attempt to avoid.

7.2 A thermal perspective on flash sintering

7.2.1 Dominance of the thermal profile in determining properties of flash sintered ceramics

Chapter 4 focused on the effect of different temperature-time profiles during flash sintering while holding the maximum current constant. A few different sample sets were generated. In the first, the current was increased at a controlled rate to the current maximum then held constant for 30s, and in the second, the same set of controlled current ramp rates were used, but the hold time was extended. The final density appeared to be fixed by the initial shrinkage rate; that is, that the density of a quickly ramped sample did not improve upon additional hold time. The increase in density with decreasing current ramp rate levelled off at values above ~$6x10^{-6}$ A/ms. Below this current ramp rate value, appreciable grain growth was also limited. This dependence of final density on densification rate was related back to the maintenance of a homogeneous pore network and the effects of gas trapping in the lattice, which are undermined by excessively rapid sintering profiles. The magnitude of grain growth observed in the slower ramp rate samples was consistent with the amount expected in similar, conventionally induced thermal profiles and in comparison to the conventionally sintered sample in that study. In addition, grain growth within the sample followed the internal thermal profile predicted by ANSYS, with less grain growth in the cooler edge and electrode regions. Overall, it was concluded that the thermal profile dominates the final microstructure of a flash sintered sample.

The electrical characteristics of these samples were compared to two conventionally prepared ceramics: one which was heated and held at temperature conventionally, followed by a

slow cool in the furnace; and one which was heated and held at temperature conventionally, but rapidly quenched from the sintering temperature. The increase in bulk conductivity evidenced in the flash sintered samples was matched by the quenched sample, indicating that this enhancement was likely due to the quench aspect of flash sintering. However, the grain boundary conductivity of the flash sintered samples was consistently much higher than the grain boundary conductivity of either the quenched or furnace cooled conventional samples.

Chapter 5 presented additional experiment and analysis following Chapter 4 in a preliminary effort to understand the origins of this grain boundary conductivity enhancement in flash sintered samples as compared to conventional. Flash sintered samples were annealed along with both quenched and slow-cooled conventionally sintered samples, and two contributions to the elevated grain boundary conductivity were identified: one which was retained post-anneal, and present in both the flash sintered sample and the conventional and quenched sample; and one which disappeared from the flash sintered sample upon annealing. Several possible reasons for this difference were discussed, including changes in the grain boundary structure, dopant segregation, or texturing. The study discussed some preliminary XRD and TEM data trying to refine the list of potential underlying physical causes, but the work thus far is inadequate to determine the exact cause of the differences in conductivity at the grain boundary.

7.2.2 Robust microstructure control via flash sintering

The microstructure results in Chapter 4 indicate great potential for flash sintering as a technique to accommodate sensitive microstructural control. Electric fields/currents are far more tunable than the temperature of a large furnace and it appears that, for a given material, an electrical profile could be developed which would limit grain growth while acquiring high densities. Furthermore, the potential to exploit this aspect of flash sintering is not limited to the

type of microstructures these studies have focused on up to this point – that is, dense samples and small grains – but could be applied to other types of microstructures, such as openly porous catalytic ceramics.

For the development of flash sintering specifically as a tool for microstructure control (setting aside materials which may benefit from other aspects of flash sintering, e.g., reduction to enhance catalyst performance), the ideal material would

1. be traditionally difficult to sinter (either due to phase decomposition limitations or low surface energies)
2. have a well-established phase diagram
3. be of scientific or industrial interest

This combination represents an optimum in technical challenge, relevance, and interpretability of the results. Materials which satisfy the above criteria include $BaTiO_3$ (BTO), in which small grained structures are highly desirable for piezo- and ferroelectric applications; it has traditionally been difficult to obtain highly dense BTO while preventing grain growth, as liquid phase formation is often required to obtain high densities. BTO also possesses a fairly low temperature eutectic (1320°C) (*182*) and a complex but well-established binary phase diagram, which controlled flash sintering might be well-suited to handle. Other high permittivity dielectrics including titanates such as $SrTiO_3$ and TiO_2 possess similar characteristics, but are arguably less technologically relevant than BTO due to the prevalence of BTO in the capacitor industry. Other ferroelectrics such as $PbZr_xTi_{1-x}O_3$ would similarly benefit from the microstructure control, but safety measures involved in processing Pb-containing materials complicate the experimental setup without offering additional incentive.

A more unusual ceramic to consider for a microstructure study could be silicon carbide, which would be particularly interesting due to the tunability of its diffusion mechanisms with doping (*183*); furthermore, its sintering temperature in the absence of external pressure and sintering aids lies above 2000°C, making furnace temperature reduction a significant processing benefit. Unfortunately, the need for an inert atmosphere means the equipment in this study is inadequate for this material, or indeed any of the non-oxide family of ceramics.

Materials that can be readily excluded from this specific list include relatively high conductivity ceramics such as ZnO; the magnitude of their conductivity enables a wide parameter set which easily produces quality samples, and generally the flash sintering of these materials have been studied substantially already. More complex materials may possess more interesting structures than the ceramics discussed above, but their complexity can make results such as grain boundary characteristics or phase changes difficult to interpret on a fundamental level.

While a handful of other ceramics may satisfy the criteria discussed above, the technological relevance and ready availability of BTO led our lab to perform some preliminary experiments on that material, using furnace temperatures and currents much lower than YSZ (700-800°C, 0.3-1 A). During these experiments, two competing obstacles became immediately apparent. The first is the low eutectic temperature; due to its high resistivity samples subject to relatively high currents or higher background temperatures quickly surpassed this point, as evidenced by liquid which formed and disrupted contact between the pellet and electrode. The second is the greater tendency of BTO to localize as compared to YSZ; low resistance paths in a highly resistive BTO matrix are proportionally more prone to current concentration. This preference towards localization was observed in these preliminary experiments as well, as

exemplified by the preliminary data shown in Figure 7.1. Optimizing parameters for the flash sintering of $BaTiO_3$ would provide a true test of the technique's ability to control microstructures.

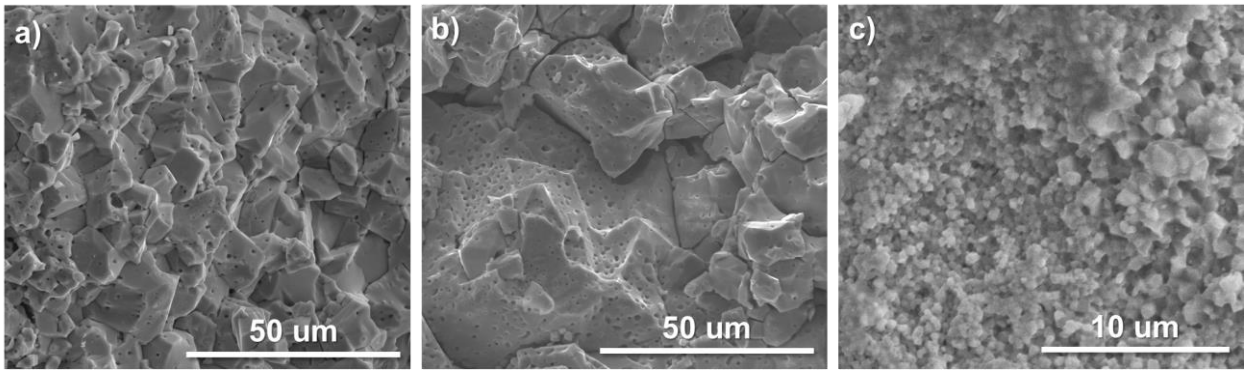

Figure 7.1 Fracture surfaces of preliminary flash sintered $BaTiO_3$, sampled from the pellet (a) center, (b) first edge, and (c) second edge. Sample was processed in an 800ºC furnace with max current of 0.6 A.

7.2.3 Questions concerning the electric field, space charge, and grain growth

There remain unanswered questions from the work in Chapters 4 and 5, and they revolve around the origins of the unusual grain boundary conductivity in flash sintered samples. Although we have offered several possible interpretations, it remains unclear whether this feature can be explained by the thermal profile, as most other characteristics of flash sintering can. Additional analysis of the grain boundaries of flash sintered YSZ is needed to identify the physical origin of the conductivity trend, specifically including grain boundary composition analysis and more robust texture analysis.

A robust grain growth study under high frequency AC fields would provide an additional information concerning the possibility of the interplay of the field with the grain boundary space charge, as the magnitude of the space charge controls solute segregation and therefore grain mobility. As discussed in Chapter 1, athermal studies (that is, studies which apply an electric field but prevent current flow) provide experimental evidence that grain growth may be enhanced by the presence of an electric field absent Joule heating effects, but this effect appears

tied to chemical polarization. Alternate studies have been performed which allow for current flow but do not consider the effects of Joule heating, and so incorrectly compare samples which are in fact processed at different temperatures in addition to the use or exclusion of an electric field. Furthermore, these studies almost invariably use DC or low frequency (60 Hz) fields, which also allow for electrochemical reduction. To our knowledge, a study has not been performed which equates thermal profiles and mitigates chemical reduction to examine direct effects of the field with the space charge.

This study could be performed using the IR and ANSYS temperature characterization procedure in Chapter 4 in combination with a high frequency power supply. Ideally an investigation would start with samples already conventionally sintered to full density and containing the same starting grain size, then subject them to the same currents for different periods of time while monitoring by IR. The same thermal profiles would then be mimicked in a furnace or rapid thermal annealer (depending on the ramp rate required) and the subsequent grain growth compared. This sample set would robustly establish or disprove a direct interaction of an external electric field with space charge.

7.3 Effects of frequency on flash sintering

Chapter 6 presented a set of smaller studies which examined the effects of processing frequency on flash sintering. In particular, the chapter hypothesized that frequencies which coupled with or surpassed specific mechanistic frequencies in YSZ might increase or homogenize heat dissipation respectively. First, data was presented characterizing the impedance of a green body sample within both the measurement and processing frequency ranges available at high temperatures. The data indicated that at the flash sintering starting temperature of 1020°C, only the electrode contribution was measurable by the impedance spectrometer, and that

processing frequencies of at least 20 kHz would need to be used if this impedance contribution were to be surpassed. The bulk and grain boundary impedance contributions were too high to measure or couple with at this temperature.

Next, a set of samples were flash sintered using frequencies ranging from 100 to 9000 Hz. The samples showed no significant density, microstructural or electrical variation with frequency. The IR measurements from these samples indicated that the thermal profile was roughly the same at each frequency and as such, production of almost identical samples was not surprising. This result agreed with the characteristic frequency interpretation because the processing frequencies were substantially lower than any characteristic frequencies at this temperature.

The second set of frequency experiments used a different sample holder, power supply, and controller to expand the frequency range up to 1.5 MHz. The samples compared were processed at 15 kHz and 1.5 MHz – below and above the expected mechanistic transition point. Impedance data was collected in situ before and after flash sintering the samples, and the spectra changed dramatically when processed at 15 kHz, while samples process at 1.5 MHz exhibited qualitatively the same behavior as the green body. It was postulated that the transition represented a stabilization of the interfacial stoichiometry – that high current, low frequency flash sintering allowed significant surface reduction, pushing the sample into a stoichiometric region where the interfacial resistance was relatively invariant under the impedance measurement voltage. High frequency flash sintering prevented this transition from occurring by limiting the accumulation of excess oxygen vacancies per cycle under high currents.

While a reasonable explanation was offered for the in-situ impedance results, additional work is needed to definitively establish the changes at the interface, perhaps utilizing sensitive

surface techniques like x-ray photoelectron spectroscopy on the as-processed surfaces of flash sintered YSZ. In addition, the effect of eliminating or including interfacial reduction on the microstructure and electrical properties of flash sintered samples should be established by repeating the study in a more thermally homogeneous sample holder. If the reduction-based hypothesis is correct, changes in the final electrical properties would be particularly of interest and perhaps more likely than microstructural changes, although processes like grain growth are also sensitive to oxygen chemical potential.

Finally, if the processing frequency could be extended into the GHz range, experiments could be used to examine the effects of short-circuiting grain boundary responses, as well as comparing the results to microwave sintering, in which net current flow is removed but electrical heat is still generated from dielectric loss. If the original theory underlying Chapter 6 holds true, activating fewer dielectric mechanisms would produce less heating, but utilizing only bulk conduction might allow for greater homogeneity or different grain boundary properties.

REFERENCES

1. M. Cologna, B. Rashkova, R. Raj, Flash Sintering of Nanograin Zirconia in < 5 s at 850 degrees C. *Journal of the American Ceramic Society* **93**, 3556-3559 (2010).

2. N. Shibata, F. Oba, T. Yamamoto, Y. Ikuhara §, Structure, energy and solute segregation behaviour of [110] symmetric tilt grain boundaries in yttria-stabilized cubic zirconia. *Philosophical Magazine* **84**, 2381-2415 (2004).

3. R. M. German, *Sintering Theory and Practice*. (John Wiley & Sons, Inc., New York, NY, 1996).

4. X. Guo, R. Waser, Electrical properties of the grain boundaries of oxygen ion conductors: Acceptor-doped zirconia and ceria. *Progress in Materials Science* **51**, 151-210 (2006).

5. D. M. Dawson, in *High Performance Materials in Aerospace*, H. M. Flower, Ed. (Chapman & Hall, London, United Kingdom, 1995), chap. 6, pp. 182-201.

6. Z. Özkurt, E. Kazazoğlu, Zirconia dental implants: a literature review. *Journal of oral implantology* **37**, 367-376 (2011).

7. *Solid Electrolytes and Their Applications*. (Plenum Press, New York, 1980).

8. R. Darolia, Thermal barrier coatings technology: critical review, progress update, remaining challenges and prospects. *Int. Mater. Rev.* **58**, 315-348 (2013).

9. D. R. Clarke, M. Oechsner, N. P. Padture, Thermal-barrier coatings for more efficient gas-turbine engines. *MRS Bulletin* **37**, 891-898 (2012).

10. Z. A. Munir, U. Anselmi-Tamburini, M. Ohyanagi, The effect of electric field and pressure on the synthesis and consolidation of materials: A review of the spark plasma sintering method. *J. Mater. Sci.* **41**, 763-777 (2006).

11. D. M. Hulbert *et al.*, The absence of plasma in "spark plasma sintering". *Journal of Applied Physics* **104**, 7 (2008).

12. D. Yang, R. Raj, H. Conrad, Enhanced Sintering Rate of Zirconia (3Y-TZP) Through the Effect of a Weak dc Electric Field on Grain Growth. *Journal of the American Ceramic Society* **93**, 2935-2937 (2010).

13. S. Ghosh, A. H. Chokshi, P. Lee, R. Raj, A Huge Effect of Weak dc Electrical Fields on Grain Growth in Zirconia. *Journal of the American Ceramic Society* **92**, 1856-1859 (2009).

14. D. Yang, H. Conrad, Influence of an electric field on the superplastic deformation of 3Y-TZP. *Scripta Materialia* **36**, 1431-1435 (1997).

15. H. Conrad, Electroplasticity in metals and ceramics. *Materials Science and Engineering: A* **287**, 276-287 (2000).

16. H. Conrad, D. Yang, Dependence of the sintering rate and related grain size of yttria-stabilized polycrystalline zirconia (3Y-TZP) on the strength of an applied DC electric field. *Materials Science and Engineering: A* **528**, 8523-8529 (2011).

17. I. W. Chen, S. W. Kim, J. Li, S. J. L. Kang, F. Huang, Ionomigration of Neutral Phases in Ionic Conductors. *Advanced Energy Materials* **2**, 1383-1389 (2012).

18. S. W. Kim, S. J. L. Kang, I. W. Chen, Electro-Sintering of Yttria-Stabilized Cubic Zirconia. *Journal of the American Ceramic Society* **96**, 1398-1406 (2013).

19. D. Yang, H. Conrad, Plastic deformation of fine-grained Al2O3 in the presence of an electric field. *Scripta Materialia* **41**, 397-401 (1999).

20. H. Conrad, Space charge and the dependence of the flow stress of ceramics on an applied electric field. *Scripta Materialia* **44**, 311-316 (2001).

21. P. L. Kapitza, *Collected Papers of PL Kapitza*. (Pergamon Press, NY Google Scholar, 1965).

22. S. W. Kim, S. J. L. Kang, I. W. Chen, Ionomigration of Pores and Gas Bubbles in Yttria-Stabilized Cubic Zirconia. *Journal of the American Ceramic Society* **96**, 1090-1098 (2013).

23. J. A. Downs, V. M. Sglavo, Electric Field Assisted Sintering of Cubic Zirconia at 390°C. *Journal of the American Ceramic Society* **96**, 1342-1344 (2013).

24. J. S. C. Francis, R. Raj, Influence of the Field and the Current Limit on Flash Sintering at Isothermal Furnace Temperatures. *Journal of the American Ceramic Society* **96**, 2754-2758 (2013).

25. J. M. Lebrun, R. Raj, A First Report of Photoemission in Experiments Related to Flash Sintering. *Journal of the American Ceramic Society* **97**, 2427-2430 (2014).

26. C. E. J. Dancer, Flash sintering of ceramic materials. *Materials Research Express* **3**, 102001 (2016).

27. M. Yu, S. Grasso, R. McKinnon, T. Saunders, M. J. Reece, Review of flash sintering: materials, mechanisms and modelling. *Advances in Applied Ceramics*, 1-37 (2016).

28. R. Muccillo, E. N. S. Muccillo, An experimental setup for shrinkage evaluation during electric field-assisted flash sintering: Application to yttria-stabilized zirconia. *Journal of the European Ceramic Society* **33**, 515-520 (2013).

29. M. C. Steil, D. Marinha, Y. Aman, J. R. C. Gomes, M. Kleitz, From conventional ac flash-sintering of YSZ to hyper-flash and double flash. *Journal of the European Ceramic Society* **33**, 2093-2101 (2013).

30. Y. Dong, I. W. Chen, Onset Criterion for Flash Sintering. *Journal of the American Ceramic Society* **98**, 3624-3627 (2015).

31. W. Qin, H. Majidi, J. Yun, K. Benthem, Electrode Effects on Microstructure Formation During FLASH Sintering of Yttrium-Stabilized Zirconia. *Journal of the American Ceramic Society* **99**, 2253-2259 (2016).

32. H. Charalambous *et al.*, Inhomogeneous reduction and its relation to grain growth of titania during flash sintering. *Scripta Materialia* **155**, 37-40 (2018).

33. Y. Zhang, J.-I. Jung, J. Luo, Thermal runaway, flash sintering and asymmetrical microstructural development of ZnO and ZnO–Bi2O3 under direct currents. *Acta Materialia* **94**, 87-100 (2015).

34. R. Muccillo, M. Kleitz, E. N. S. Muccillo, Flash grain welding in yttria stabilized zirconia. *Journal of the European Ceramic Society* **31**, 1517-1521 (2011).

35. M. Cologna, A. L. G. Prette, R. Raj, Flash-Sintering of Cubic Yttria-Stabilized Zirconia at 750°C for Possible Use in SOFC Manufacturing. *Journal of the American Ceramic Society* **94**, 316-319 (2011).

36. S. G. M. Carvalho, E. N. S. Muccillo, R. Muccillo, AC Electric Field Assisted Pressureless Sintering Zirconia: 3 mol% Yttria Solid Electrolyte. *physica status solidi (a)*, (2018).

37. W. Qin, J. Yun, A. M. Thron, K. van Benthem, Temperature gradient and microstructure evolution in AC flash sintering of 3 mol% yttria-stabilized zirconia. *Materials and Manufacturing Processes* **32**, 549-556 (2017).

38. S. Carvalho, E. Muccillo, R. Muccillo, Electrical Behavior and Microstructural Features of Electric Field-Assisted and Conventionally Sintered 3 mol% Yttria-Stabilized Zirconia. *Ceramics* **1**, 2 (2018).

39. X. Vendrell, D. Yadav, R. Raj, A. R. West, Influence of flash sintering on the ionic conductivity of 8 mol% yttria stabilized zirconia. *Journal of the European Ceramic Society*, (2018).

40. R. Muccillo, E. N. S. Muccillo, Electric field assisted sintering of electroceramics and in situ analysis by impedance spectroscopy. *Journal of Electroceramics* **38**, 24-42 (2017).

41. K. H. Christian, H. Charalambous, S. K. Jha, T. Tsakalakos, Current-ramp assisted sintering of 3YSZ: Electrochemical and microstructural comparison to flash and thermal sintering. *Journal of the European Ceramic Society* **40**, 436-443 (2020).

42. K. Terauds *et al.*, Electroluminescence and the measurement of temperature during Stage III of flash sintering experiments. *Journal of the European Ceramic Society* **35**, 3195-3199 (2015).

43. J. A. Downs, University of Trento, (2013).

44. M. Biesuz, P. Luchi, A. Quaranta, A. Martucci, V. M. Sglavo, Photoemission during flash sintering: An interpretation based on thermal radiation. *Journal of the European Ceramic Society* **37**, 3125-3130 (2017).

45. R. E. W. Casselton, Blackening in yttria stabilized zirconia due to cathodic processes at solid platinum electrodes. *Journal of Applied Electrochemistry* **4**, 25-48 (1974).

46. R. Raj, Joule heating during flash-sintering. *Journal of the European Ceramic Society* **32**, 2293-2301 (2012).

47. J. Frenkel, On Pre-Breakdown Phenomena in Insulators and Electronic Semi-Conductors. *Physical Review* **54**, 647-648 (1938).

48. M. Cologna, J. S. C. Francis, R. Raj, Field assisted and flash sintering of alumina and its relationship to conductivity and MgO-doping. *Journal of the European Ceramic Society* **31**, 2827-2837 (2011).

49. K. S. Naik, V. M. Sglavo, R. Raj, Flash sintering as a nucleation phenomenon and a model thereof. *Journal of the European Ceramic Society* **34**, 4063-4067 (2014).

50. H. Gao *et al.*, Native point defect formation in flash sintered ZnO studied by depth-resolved cathodoluminescence spectroscopy. *Journal of Applied Physics* **120**, 105302 (2016).

51. B. Yoon *et al.*, Measurement of O and Ti atom displacements in TiO2 during flash sintering experiments. *Journal of the American Ceramic Society* **101**, 1811-1817 (2018).

52. J. M. Lebrun *et al.*, Emergence and extinction of a new phase during on–off experiments related to flash sintering of 3 YSZ. *Journal of the American Ceramic Society* **98**, 1493-1497 (2015).

53. N. Shomrat, S. Baltianski, E. Dor, Y. Tsur, The influence of doping on flash sintering conditions in SrTi1−xFexO3−δ. *Journal of the European Ceramic Society* **37**, 179-188 (2017).

54. M. Jongmanns, R. Raj, D. E. Wolf, Generation of Frenkel defects above the Debye temperature by proliferation of phonons near the Brillouin zone edge. *New Journal of Physics* **20**, 093013 (2018).

55. T. P. Mishra *et al.*, On the role of Debye temperature in the onset of flash in three oxides. *Scripta Materialia* **170**, 81-84 (2019).

56. R. Chaim, Liquid Film Capillary Mechanism for Densification of Ceramic Powders during Flash Sintering. *Materials* **9**, 280 (2016).

57. R. Chaim, Particle Surface Softening as Universal Behaviour during Flash Sintering of Oxide Nano-Powders. *Materials* **10**, 179 (2017).

58. G. Corapcioglu *et al.*, Microstructure and microchemistry of flash sintered $K_{0.5}Na_{0.5}NbO_3$. *Journal of the Ceramic Society of Japan* **124**, 321-328 (2016).

59. R. Serrazina *et al.*, Mechanism of densification in low-temperature FLASH sintered lead free potassium sodium niobate (KNN) piezoelectrics. *Journal of Materials Chemistry C* **7**, 14334-14341 (2019).

60. M. Biesuz, V. M. Sglavo, Current-induced abnormal and oriented grain growth in corundum upon flash sintering. *Scripta Materialia* **150**, 82-86 (2018).

61. W. Ji *et al.*, Ultra-fast firing: Effect of heating rate on sintering of 3YSZ, with and without an electric field. *Journal of the European Ceramic Society* **37**, 2547-2551 (2017).

62. J. G. P. da Silva, H. A. Al-Qureshi, F. Keil, R. Janssen, A dynamic bifurcation criterion for thermal runaway during the flash sintering of ceramics. *Journal of the European Ceramic Society* **36**, 1261-1267 (2016).

63. R. I. Todd, E. Zapata-Solvas, R. S. Bonilla, T. Sneddon, P. R. Wilshaw, Electrical characteristics of flash sintering: thermal runaway of Joule heating. *Journal of the European Ceramic Society* **35**, 1865-1877 (2015).

64. I. J. Hewitt, A. A. Lacey, R. I. Todd, A Mathematical Model for Flash Sintering. *Mathematical Modelling of Natural Phenomena* **10**, 77-89 (2015).

65. Y. Zhang, J. Luo, Promoting the flash sintering of ZnO in reduced atmospheres to achieve nearly full densities at furnace temperatures of <120°C. *Scripta Materialia* **106**, 26-29 (2015).

66. M. P. Harmer, E. W. Roberts, R. J. Brook, Rapid sintering of pure and doped -Al_2O_3. *Transactions and Journal of the British Ceramic Society* **78**, 22-25 (1979).

67. D. E. García, J. Seidel, R. Janssen, N. Claussen, Fast firing of alumina. *Journal of the European Ceramic Society* **15**, 935-938 (1995).

68. C. Feng, H. Qiu, J. Guo, D. Yan, W. Schulze, Fast firing of nanoscale ZrO sub 2+ 2. 8 mol% Y sub 2 O sub 3 ceramic powder synthesized by sol-gel process. *J. Mater. Synth. Process.(USA)* **3**, 25-29 (1995).

69. D. E. García, D. Hotza, R. Janssen, Building a sintering front through fast firing. *International Journal of Applied Ceramic Technology* **8**, 1486-1493 (2011).

70. R. M. Young, R. McPherson, Temperature-Gradient-Driven Diffusion in Rapid-Rate Sintering. *Journal of the American Ceramic Society* **72**, 1080-1081 (1989).

71. M. Biesuz, V. M. Sglavo, Microstructural temperature gradient-driven diffusion: Possible densification mechanism for flash sintering of zirconia? *Ceramics International* **45**, 1227-1236 (2019).

72. M. Y. Chu, M. N. Rahaman, L. C. Jonghe, R. J. Brook, Effect of Heating Rate on Sintering and Coarsening. *Journal of the American Ceramic Society* **74**, 1217-1225 (1991).

73. P. Roura, J. Costa, J. Farjas, Is sintering enhanced under non-isothermal conditions? *Materials Science and Engineering: A* **337**, 248-253 (2002).

74. J. S. C. Francis, M. Cologna, R. Raj, Particle size effects in flash sintering. *Journal of the European Ceramic Society* **32**, 3129-3136 (2012).

75. Y. Zhang, J. Nie, J. M. Chan, J. Luo, Probing the densification mechanisms during flash sintering of ZnO. *Acta Materialia* **125**, 465-475 (2017).

76. H. Charalambous, S. K. Jha, J. Okasinski, T. Tsakalakos, Spectral analysis and temperature measurement during flash sintering under AC electric field. *Materialia* **6**, 100273 (2019).

77. M. Yoshida, S. Falco, R. I. Todd, Measurement and modelling of electrical resistivity by four-terminal method during flash sintering of 3YSZ. *Journal of the Ceramic Society of Japan* **126**, 579-590 (2018).

78. C. A. Grimley, A. L. Prette, E. C. Dickey, Effect of boundary conditions on reduction during early stage flash sintering of YSZ. *Acta Materialia* **174**, 271-278 (2019).

79. M. Biesuz *et al.*, Investigation of Electrochemical, Optical and Thermal Effects during Flash Sintering of 8YSZ. *Materials* **11**, 1214 (2018).

80. S. K. Jha *et al.*, In-situ observation of oxygen mobility and abnormal lattice expansion in ceria during flash sintering. *Ceramics International* **44**, 15362-15369 (2018).

81. N. Masó, A. R. West, Electronic Conductivity in Yttria-Stabilized Zirconia under a Small dc Bias. *Chemistry of Materials* **27**, 1552-1558 (2015).

82. G. Liu, D. Liu, J. Liu, Y. Gao, Y. Wang, Asymmetric temperature distribution during steady stage of flash sintering dense zirconia. *Journal of the European Ceramic Society* **38**, 2893-2896 (2018).

83. O. Rozenbaum, D. D. S. Meneses, P. Echegut, Texture and porosity effects on the thermal radiative behavior of alumina ceramics. *International Journal of Thermophysics* **30**, 580-590 (2009).

84. Y. Du, A. J. Stevenson, D. Vernat, M. Diaz, D. Marinha, Estimating Joule heating and ionic conductivity during flash sintering of 8YSZ. *Journal of the European Ceramic Society* **36**, 749-759 (2016).

85. H. Tanaka, S. Sawai, K. Morimoto, K. Hisano, Measurement of Spectral Emissivity and Thermal Conductivity of Zirconia by Thermal Radiation Calorimetry. *Journal of Thermal Analysis and Calorimetry* **64**, 867-872 (2001).

86. H. Charalambous *et al.*, In situ measurement of temperature and reduction of rutile titania using energy dispersive x-ray diffraction. *Journal of the European Ceramic Society* **38**, 5503-5511 (2018).

87. J. G. P. d. Silva, J. M. Lebrun, H. A. Al-Qureshi, R. Janssen, R. Raj, Temperature Distributions During Flash Sintering of 8% Yttria-Stabilized Zirconia. *Journal of the American Ceramic Society* **98**, 3525-3528 (2015).

88. H. Charalambous *et al.*, Investigation of temperature approximation methods during flash sintering of ZnO. *Ceramics International* **44**, 6162-6169 (2018).

89. J. Park, I. W. Chen, In Situ Thermometry Measuring Temperature Flashes Exceeding 1,700°C in 8 mol% Y2O3-Stablized Zirconia Under Constant-Voltage Heating. *Journal of the American Ceramic Society* **96**, 697-700 (2013).

90. J. S. C. Francis, R. Raj, Flash-Sinterforging of Nanograin Zirconia: Field Assisted Sintering and Superplasticity. *Journal of the American Ceramic Society* **95**, 138-146 (2012).

91. H. Yoshida, P. Biswas, R. Johnson, M. K. Mohan, Flash-sintering of magnesium aluminate spinel (MgAl2O4) ceramics. *Journal of the American Ceramic Society* **100**, 554-562 (2017).

92. H. Yoshida, Y. Sakka, T. Yamamoto, J.-M. Lebrun, R. Raj, Densification behaviour and microstructural development in undoped yttria prepared by flash-sintering. *Journal of the European Ceramic Society* **34**, 991-1000 (2014).

93. S. Grasso *et al.*, Modeling of the temperature distribution of flash sintered zirconia. *Journal of the Ceramic Society of Japan* **119**, 144-146 (2011).

94. J. M. Lebrun, S. K. Jha, S. J. McCormack, W. M. Kriven, R. Raj, Broadening of diffraction peak widths and temperature nonuniformity during flash experiments. *Journal of the American Ceramic Society* **99**, 3429-3434 (2016).

95. S. K. Jha, J. M. Lebrun, K. C. Seymour, W. M. Kriven, R. Raj, Electric field induced texture in titania during experiments related to flash sintering. *Journal of the European Ceramic Society* **36**, 257-261 (2016).

96. L. A. Perez-Maqueda *et al.*, Insight into the BiFeO3 flash sintering process by in-situ energy dispersive X-ray diffraction (ED-XRD). *Ceramics International* **45**, 2828-2834 (2019).

97. W. Rheinheimer, J. P. Parras, J. H. Preusker, R. A. De Souza, M. J. Hoffmann, Grain growth in strontium titanate in electric fields: The impact of space-charge on the grain-boundary mobility. *Journal of the American Ceramic Society* **102**, 3779-3790 (2019).

98. W. Rheinheimer, M. Fülling, M. J. Hoffmann, Grain growth in weak electric fields in strontium titanate: Grain growth acceleration by defect redistribution. *Journal of the European Ceramic Society* **36**, 2773-2780 (2016).

99. Y. Dong, I. W. Chen, Electrical and hydrogen reduction enhances kinetics in doped zirconia and ceria: II. Mapping electrode polarization and vacancy condensation in YSZ. *Journal of the American Ceramic Society* **101**, 1058-1073 (2018).

100. S. W. Kim, S. G. Kim, J. I. Jung, S. J. L. Kang, I. W. Chen, Enhanced Grain Boundary Mobility in Yttria-Stabilized Cubic Zirconia under an Electric Current. *Journal of the American Ceramic Society* **94**, 4231-4238 (2011).

101. H. Conrad, J. Wang, Equivalence of AC and DC electric field on retarding grain growth in yttria-stabilized zirconia. *Scripta Materialia* **72**, 33-34 (2014).

102. W. Straka, S. Amoah, J. Schwartz, Densification of thoria through flash sintering. *MRS Communications* **7**, 677-682 (2017).

103. GamryInstruments, Basics of Electrochemical Impedance Spectroscopy (application note). 2019.

104. A. K. Jonscher, *Dielectric Relaxation in Solids*. (Chelsea Dielectrics Press Ltd., London, UK, 1983).

105. J. T. Irvine, D. C. Sinclair, A. R. West, Electroceramics: characterization by impedance spectroscopy. *Advanced Materials* **2**, 132-138 (1990).

106. C. Hsu, F. Mansfeld, Concerning the conversion of the constant phase element parameter Y0 into a capacitance. *Corrosion* **57**, 747-748 (2001).

107. E. P. Butler, N. Bonanos, The characterization of ZrO2 engineering ceramics by A.C. impedance spectroscopy. *Materials Science and Engineering* **71**, 49-56 (1985).

108. A. Bondarenko, G. Ragoisha, Progress in chemometrics research. *Nova Science Publishers, New York*, 89-102 (2005).

109. T. v. Dijk, A. J. Burggraaf, Grain boundary effects on ionic conductivity in ceramic GdxZr1–xO2–(x/2) solid solutions. *physica status solidi (a)* **63**, 229-240 (1981).

110. X. Guo, J. Maier, Grain boundary blocking effect in zirconia: a Schottky barrier analysis. *Journal of the Electrochemical Society* **148**, E121-E126 (2001).

111. M. Biesuz, V. M. Sglavo, Flash sintering of ceramics. *Journal of the European Ceramic Society* **39**, 115-143 (2019).

112. J. Wang, H. Conrad, Contribution of the space charge to the grain boundary energy in yttria-stabilized zirconia. *J. Mater. Sci.* **49**, 6074-6080 (2014).

113. H. Conrad, D. Yang, Influence of an applied dc electric field on the plastic deformation kinetics of oxide ceramics. *Philosophical Magazine* **90**, 1141-1157 (2010).

114. R. Kirchheim, On the mixed ionic and electronic conductivity in polarized yttria stabilized zirconia. *Solid State Ionics* **320**, 239-258 (2018).

115. B. Steele, Interfacial reactions associated with ceramic ion transport membranes. *Solid State Ionics* **75**, 157-165 (1995).

116. J. H. Park, R. N. Blumenthal, Electronic Transport in 8 Mole Percent Y 2 O 3-ZrO2. *Journal of the Electrochemical Society* **136**, 2867-2876 (1989).

117. S. B. Adler, Factors Governing Oxygen Reduction in Solid Oxide Fuel Cell Cathodes. *Chemical Reviews* **104**, 4791-4844 (2004).

118. A. K. Opitz, A. Schintlmeister, H. Hutter, J. Fleig, Visualization of oxygen reduction sites at Pt electrodes on YSZ by means of 18O tracer incorporation: The width of the electrochemically active zone. *Physical Chemistry Chemical Physics* **12**, 12734-12745 (2010).

119. V. S. Bagotsky, *Fundamentals of Electrochemistry*. The Electrochemical Society Series (John Wiley & Sons, Inc., Hoboken, New Jersey, ed. 2nd, 2006).

120. A. Luntz, M. Williams, D. Bethune, The sticking of O2 on a Pt (111) surface. *The Journal of chemical physics* **89**, 4381-4395 (1988).

121. C. T. Campbell, G. Ertl, H. Kuipers, J. Segner, A molecular beam study of the adsorption and desorption of oxygen from a Pt(111) surface. *Surface Science* **107**, 220-236 (1981).

122. P. S. Manning, J. D. Sirman, R. A. De Souza, J. A. Kilner, The kinetics of oxygen transport in 9.5 mol % single crystal yttria stabilised zirconia. *Solid State Ionics* **100**, 1-10 (1997).

123. A. Elsner, A. Wagner, T. Aste, H. Hermann, D. Stoyan, Specific surface area and volume fraction of the cherry-pit model with packed pits. *The Journal of Physical Chemistry B* **113**, 7780-7784 (2009).

124. A. Mitterdorfer, L. J. Gauckler, Reaction kinetics of the Pt, O2(g)|c-ZrO2 system: precursor-mediated adsorption. *Solid State Ionics* **120**, 211-225 (1999).

125. A. Mitterdorfer, L. Gauckler, Identification of the reaction mechanism of the Pt, O2 (g)| yttria-stabilized zirconia system: Part I: General framework, modelling, and structural investigation. *Solid State Ionics* **117**, 187-202 (1999).

126. R. Waser, T. Baiatu, K. H. Härdtl, dc Electrical Degradation of Perovskite-Type Titanates: I, Ceramics. *Journal of the American Ceramic Society* **73**, 1645-1653 (1990).

127. T. Baiatu, R. Waser, K. H. Härdtl, dc Electrical Degradation of Perovskite-Type Titanates: III, A Model of the Mechanism. *Journal of the American Ceramic Society* **73**, 1663-1673 (1990).

128. R. Waser, T. Baiatu, K. H. Härdtl, dc Electrical Degradation of Perovskite-Type Titanates: II, Single Crystals. *Journal of the American Ceramic Society* **73**, 1654-1662 (1990).

129. Y. Dong, I. W. Chen, Oxygen potential transition in mixed conducting oxide electrolyte. *Acta Materialia* **156**, 399-410 (2018).

130. C. Bonola, P. Camagni, P. Chiodelli, G. Samoggia, Study of defects introduced by electroreduction in YSZ. *Radiation Effects and Defects in Solids* **119-121**, 457-462 (1991).

131. V. M. Orera, R. I. Merino, Y. Chen, R. Cases, P. J. Alonso, Electron and hole trapped defects produced by thermoreduction or irradiation in Stabilized Zirconia. *Radiation Effects and Defects in Solids* **119-121**, 907-912 (1991).

132. R. Ben-Michael, D. Tannhauser, J. Genossar, ESR centers in reduced stabilized zirconia. *Physical Review B* **43**, 7395 (1991).

133. W. Ma, F. W. Herbert, S. D. Senanayake, B. Yildiz, Non-equilibrium oxidation states of zirconium during early stages of metal oxidation. *Applied Physics Letters* **106**, 101603 (2015).

134. F. Moghadam, T. Yamashita, D. Stevenson, Characterization of the current-blackening phenomena in scandia stabilized zirconia using transmission electron microscopy. *J. Mater. Sci.* **18**, 2255-2259 (1983).

135. M. Levy, J. Fouletier, M. Kleitz, Model for the electrical conductivity of reduced stabilized zirconia. *Journal of the Electrochemical Society* **135**, 1584-1589 (1988).

136. D. Siegel, F. El Gabaly, K. McCarty, N. Bartelt, In situ characterization of the formation of a mixed conducting phase on the surface of yttria-stabilized zirconia near Pt electrodes. *Physical Review B* **92**, 125421 (2015).

137. J. Janek, C. Korte, Electrochemical blackening of yttria-stabilized zirconia – morphological instability of the moving reaction front. *Solid State Ionics* **116**, 181-195 (1999).

138. H. Schmalzried, *Chemical kinetics of solids*. (John Wiley & Sons, 2008).

139. J.-C. M'Peko, J. S. C. Francis, R. Raj, Field-assisted sintering of undoped BaTiO3: Microstructure evolution and dielectric permittivity. *Journal of the European Ceramic Society* **34**, 3655-3660 (2014).

140. Y. Yamashita, T. Kurachi, T. Tokunaga, H. Yoshida, T. Yamamoto, Technique to control specimen electric current during a flash state with alternating current electric fields. *Journal of the Ceramic Society of Japan* **127**, 849-851 (2019).

141. C. Schmerbauch, J. Gonzalez-Julian, R. Röder, C. Ronning, O. Guillon, Flash sintering of nanocrystalline zinc oxide and its influence on microstructure and defect formation. *Journal of the American Ceramic Society* **97**, 1728-1735 (2014).

142. J. M. Lebrun *et al.*, In-situ Measurements of Lattice Expansion Related to Defect Generation During Flash Sintering. *Journal of the American Ceramic Society*, (2017).

143. C. Cao, R. Mücke, O. Guillon, Effect of AC field on uniaxial viscosity and sintering stress of ceria. *Acta Materialia* **182**, 77-86 (2020).

144. H. Charalambous, S. K. Jha , K. H. Christian, R. T. Lay, T. Tsakalakos, Flash Sintering using Controlled Current Ramp. *Journal of the European Ceramic Society* **38**, 3689 - 3693 (2018).

145. P. Kumar MK, D. Yadav, J. M. Lebrun, R. Raj, Flash sintering with current rate: A different approach. *Journal of the American Ceramic Society* **102**, 823-835 (2019).

146. X. L. Phuah *et al.*, Comparison of the grain growth behavior and defect structures of flash sintered ZnO with and without controlled current ramp. *Scripta Materialia* **162**, 251-255 (2019).

147. I. R. Lavagnini, J. V. Campos, J. A. Ferreira, E. M. d. J. A. Pallone, Microstructural evolution of 3YSZ flash-sintered with current ramp control. *J. Am. Ceram. Soc.* **Accepted, unpublished**, (2020).

148. M. I. Mendelson, Average grain size in polycrystalline ceramics. *Journal of the American Ceramic society* **52**, 443-446 (1969).

149. G. Petzow, H. E. Exner, in *Sintering key papers*. (Springer, 1990), pp. 639-655.

150. M. F. Yan, Microstructural control in the processing of electronic ceramics. *Materials Science and Engineering* **48**, 53-72 (1981).

151. M. F. Yan, R. Cannon Jr, H. Bowen, U. Chowdhry, Effect of grain size distribution on sintered density. *Materials science and engineering* **60**, 275-281 (1983).

152. R. Coble, Sintering alumina: effect of atmospheres. *Journal of the American Ceramic Society* **45**, 123-127 (1962).

153. R. Vines, J. Semmelman, P. Lee, F. Fonvielle Jr, Mechanisms involved in securing dense, vitrified ceramics from preshaped partly crystalline bodies. *Journal of the American Ceramic Society* **41**, 304-309 (1958).

154. R. M. German, K. Churn, Sintering atmosphere effects on the ductility of W-Ni-Fe heavy metals. *Metallurgical Transactions A* **15**, 747-754 (1984).

155. H. Palmour, M. Huckabee, in *'Sintering- New Developments'. Proc. Fourth Int. Round Table Conf. on Sintering held at Dubrovnik, Yugoslavia, Sept. 5-10, 1977. Edited by M. M. Ristic. Elsevier Sci. Publishing Co., Amsterdam, 1979.* (1977), pp. 46.

156. H. Palmour, in *Science of sintering*. (Springer, 1989), pp. 337-356.

157. M. L. Huckabee, T. M. Hare, H. I. Palmour, in *Processing of Crystalline Ceramics,* H. I. Palmour, R. F. Davis, T. M. Hare, Eds. (Plenum Press, New York, 1978), pp. 205-215.

158. M. L. Huckabee, H. Palmour, Rate Controlled sintering of fine-grained Al 2 O 3. *Am Ceram Soc Bull* **51**, 574-576 (1972).

159. C. Cao, R. Mücke, O. Guillon, Effect of AC field on uniaxial viscosity and sintering stress of ceria. *Acta Materialia*, (2019).

160. R. Chaim, G. Chevallier, A. Weibel, C. Estournès, Grain growth during spark plasma and flash sintering of ceramic nanoparticles: a review. *J. Mater. Sci.* **53**, 3087-3105 (2018).

161. A. El Barhmi, E. Schouler, A. Hammou, M. Kleitz, Influence of quenching on the electrical properties of yttria-stabilized zirconia. *Solid State Ionics* **28**, 493-496 (1988).

162. S. Badwal, F. Ciacchi, R. Hannink, Relationship between phase stability and conductivity of yttria tetragonal zirconia. *Solid State Ionics* **40**, 882-885 (1990).

163. M. Weller *et al.*, Oxygen mobility in yttria-doped zirconia studied by internal friction, electrical conductivity and tracer diffusion experiments. *Solid State Ionics* **175**, 409-413 (2004).

164. J. A. Kilner, B. Steele, in *Nonstoichiometric Oxides,* O. T. Sorenson, Ed. (Academic Press, Inc., London, UK, 1987), chap. 5, pp. 233-269.

165. M. J. Verkerk, B. J. Middelhuis, A. J. Burggraaf, Effect of grain boundaries on the conductivity of high-purity ZrO_2-Y_2O_3 ceramics. *Solid State Ionics* **6**, 159-170 (1982).

166. J. Zhang, F. Meng, R. I. Todd, Z. Fu, The nature of grain boundaries in alumina fabricated by fast sintering. *Scripta Materialia* **62**, 658-661 (2010).

167. H. Wang *et al.*, Key microstructural characteristics in flash sintered 3YSZ critical for enhanced sintering process. *Ceramics International* **45**, 1251-1257 (2019).

168. Z. Mao, S. B. Sinnott, E. C. Dickey, Ab initio calculations of pristine and doped Zirconia Σ5 (310)/[001] tilt grain boundaries. *Journal of the American Ceramic Society* **85**, 1594-1600 (2002).

169. T. Oyama, M. Yoshiya, H. Matsubara, K. Matsunaga, Numerical analysis of solute segregation at Σ 5 (310)/[001] symmetric tilt grain boundaries in Y 2 O 3-doped ZrO 2. *Physical Review B* **71**, 224105 (2005).

170. K. Vikrant, R. E. García, Charged grain boundary transitions in ionic ceramics for energy applications. *npj Computational Materials* **5**, 24 (2019).

171. S. Badwal, Grain boundary resistivity in zirconia-based materials: effect of sintering temperatures and impurities. *Solid State Ionics* **76**, 67-80 (1995).

172. S. Badwal, Yttria tetragonal zirconia polycrystalline electrolytes for solid state electrochemical cells. *Applied Physics A* **50**, 449-462 (1990).

173. P. R. Cantwell *et al.*, Grain boundary complexions. *Acta Materialia* **62**, 1 - 48 (2014).

174. J. Goff, W. Hayes, S. Hull, M. Hutchings, K. N. Clausen, Defect structure of yttria-stabilized zirconia and its influence on the ionic conductivity at elevated temperatures. *Physical Review B* **59**, 14202 (1999).

175. A. E. Hughes, S. P. S. Badwal, Impurity and yttrium segregation in yttria-tetragonal zirconia. *Solid State Ionics* **46**, 265-274 (1991).

176. S. Badwal, Zirconia-based solid electrolytes: microstructure, stability and ionic conductivity. *Solid State Ionics* **52**, 23-32 (1992).

177. X. Guo, Z. Zhang, Grain size dependent grain boundary defect structure: case of doped zirconia. *Acta materialia* **51**, 2539-2547 (2003).

178. D. Klotz, Negative capacitance or inductive loop?–A general assessment of a common low frequency impedance feature. *Electrochemistry Communications* **98**, 58-62 (2019).

179. T. Jacobsen, B. Zachau-Christiansen, L. Bay, M. J. Jørgensen, Hysteresis in the solid oxide fuel cell cathode reaction. *Electrochimica Acta* **46**, 1019-1024 (2001).

180. E. Schouler, M. Kleitz, Electrocatalysis and inductive effects at the gas, Pt/stabilized zirconia interface. *Journal of The Electrochemical Society* **134**, 1045-1050 (1987).

181. E. Siebert, A. Hammouche, M. Kleitz, Impedance spectroscopy analysis of La1−xSritxMnO3-yttria-stabilized zirconia electrode kinetics. *Electrochimica Acta* **40**, 1741-1753 (1995).

182. S. Lee, C. A. Randall, Z. K. Liu, Modified Phase Diagram for the Barium Oxide–Titanium Dioxide System for the Ferroelectric Barium Titanate. *J. Am. Ceram. Soc.* **90**, 2589-2594 (2007).

183. G. Magnani, G. Sico, A. Brentari, P. Fabbri, Solid-state pressureless sintering of silicon carbide below 2000° C. *Journal of the European Ceramic Society* **34**, 4095-4098 (2014).

APPENDIX

Reprint Permissions

Throughout the preceding text, material from previous publications was reproduced with permission from the publishing companies. This includes the full content of Chapter 3, and Figures 1.1, 1.2, and 1.4. The permissions obtained from John Wiley and Sons are reproduced below and cover the duplicated figures. Elsevier does not require authors to acquire permissions to reproduce their own articles in dissertations; this accommodates the use of published content in Chapter 3.

JOHN WILEY AND SONS LICENSE
TERMS AND CONDITIONS

Jan 31, 2020

This Agreement between Mrs. Carolyn Grimley ("You") and John Wiley and Sons ("John Wiley and Sons") consists of your license details and the terms and conditions provided by John Wiley and Sons and Copyright Clearance Center.

License Number	4751370426892
License date	Jan 17, 2020
Licensed Content Publisher	John Wiley and Sons
Licensed Content Publication	Wiley Books
Licensed Content Title	Sintering Theory and Practice
Licensed Content Author	Randall M. German
Licensed Content Date	Jan 1, 1996
Licensed Content Pages	1
Type of use	Dissertation/Thesis
Requestor type	University/Academic
Format	Electronic
Portion	Figure/table
Number of figures/tables	2

Original Wiley figure/table number(s)	Figure 3.10 Figure 3.20
Will you be translating?	No
Title of your thesis / dissertation	Decoupling Chemical, Thermal, and Electrical Effects in Flash Sintering
Expected completion date	Feb 2020
Expected size (number of pages)	100
Requestor Location	Mrs. Carolyn Grimley 222 Bald Eagle Lane CARY, NC 27518 United States Attn: Mrs. Carolyn Grimley
Publisher Tax ID	EU826007151
Total	0.00 USD

Terms and Conditions

TERMS AND CONDITIONS

This copyrighted material is owned by or exclusively licensed to John Wiley & Sons, Inc. or one of its group companies (each a"Wiley Company") or handled on behalf of a society with which a Wiley Company has exclusive publishing rights in relation to a particular work (collectively "WILEY"). By clicking "accept" in connection with completing this licensing transaction, you agree that the following terms and conditions apply to this transaction (along with the billing and payment terms and conditions established by the Copyright Clearance Center Inc., ("CCC's Billing and Payment terms and conditions"), at the time that you opened your RightsLink account (these are available at any time at http://myaccount.copyright.com).

Terms and Conditions

- The materials you have requested permission to reproduce or reuse (the "Wiley Materials") are protected by copyright.

JOHN WILEY AND SONS LICENSE
TERMS AND CONDITIONS

Jan 31, 2020

This Agreement between Mrs. Carolyn Grimley ("You") and John Wiley and Sons ("John Wiley and Sons") consists of your license details and the terms and conditions provided by John Wiley and Sons and Copyright Clearance Center.

License Number	4751371100212
License date	Jan 17, 2020
Licensed Content Publisher	John Wiley and Sons
Licensed Content Publication	Journal of the American Ceramic Society
Licensed Content Title	Flash Sintering of Nanograin Zirconia in <5 s at 850°C
Licensed Content Author	Rishi Raj, Boriana Rashkova, Marco Cologna
Licensed Content Date	Sep 28, 2010
Licensed Content Volume	93
Licensed Content Issue	11
Licensed Content Pages	4
Type of use	Dissertation/Thesis
Requestor type	University/Academic
Format	Electronic

Portion	Figure/table
Number of figures/tables	1
Original Wiley figure/table number(s)	Figure 1
Will you be translating?	No
Title of your thesis / dissertation	Decoupling Chemical, Thermal, and Electrical Effects in Flash Sintering
Expected completion date	Feb 2020
Expected size (number of pages)	100
Requestor Location	Mrs. Carolyn Grimley 222 Bald Eagle Lane CARY, NC 27518 United States Attn: Mrs. Carolyn Grimley
Publisher Tax ID	EU826007151
Total	0.00 USD

Terms and Conditions

TERMS AND CONDITIONS

This copyrighted material is owned by or exclusively licensed to John Wiley & Sons, Inc. or one of its group companies (each a"Wiley Company") or handled on behalf of a society with which a Wiley Company has exclusive publishing rights in relation to a particular work (collectively "WILEY"). By clicking "accept" in connection with completing this licensing transaction, you agree that the following terms and conditions apply to this transaction (along with the billing and payment terms and conditions established by the Copyright Clearance Center Inc., ("CCC's Billing and Payment terms and conditions"), at the time that you opened your RightsLink account (these are available at any time at http://myaccount.copyright.com).